Feasibility Analysis and Optimization of a Propulsive Empennage Aircraft

Aerodynamic and Flight Mechanics Evaluation of the DUUC V0.1 Concept

AE5551 - Master Thesis

Tom van de Water

Delft University of Technology

TU Delft

Feasibility Analysis and Optimization of a Propulsive Empennage Aircraft

Aerodynamic and Flight Mechanics Evaluation of the DUUC V0.1 Concept

by

Tom van de Water

in partial fulfillment of the requirements for the degree of

Master of Science
in Aerospace Engineering

at the Delft University of Technology,
to be defended publicly on Thursday July 17, 2025 at 13:30.

Student number:	4664868	
Thesis committee:	Prof. dr. ir. L.L.M. Veldhuis	TU Delft, Daily Supervisor
	Dr. C. Varriale	TU Delft, Chair
	Ir. P.C. Roling	TU Delft, Examiner

Cover: Artist impression DUUC V0.1 model [1]

A digital copy of this thesis is available at http://repository.tudelft.nl/.

TU Delft

Preface

The analysis of the DUUC rounds up my study period in Delft, where I have been able to develop myself as a Flight Performance engineer that became even more inspired by the wonders of aviation. This thesis marks the end of my student time and the beginning of my time as an engineer.

When the topic of the DUUC came on my path, I was immediately interested in the newness and unconventional nature of this project. A few students have worked on this project before and there are aircraft with aft-mounted engines so my first thoughts were, this should be possible. This has allowed my to stay critical throughout the whole development of the prediction models and evaluation of the results.

The challenge of this project was found in the fact that some students had worked on this project before without very clear concise answers. The vast amount of parameters, aerodynamic and flight dynamic disciplines that had to be researched made this a real challenge. The balance between details and aircraft level integration had to be maintained while keeping a birds eye view towards the end goal. I have really enjoyed the puzzle of all the data regarding the DUUC and I am happy with the results produced that will lead to a more conclusive answer on the question, to DUUC or not to DUUC? As that mostly captures the project goal.

First of all, I would like to thank my supervisor Leo Veldhuis, who has given me the opportunity to work on this challenging and inspiring topic, and for his continuous support and feedback throughout my thesis project. I am very grateful for the help and insight that I have received on the aerodynamics of the DUUC. In addition to that I would like to thank Maurice Hoogreef and Carmine Varriale for the knowledge and support on the flight mechanics evaluation, your enthusiasm has pushed this project to the next level. Furthermore, I would like to thank the thesis committee for the time and effort they took to evaluate this thesis.

I would like to thank all my friends for the support they gave during this project. They were a welcome form of distraction, but also a source of inspiration for creative solutions. A special thanks goes to Rik Lambrichs for all the endless brainstorm sessions and support whilst working in the basement of the High Speed Lab.

At last, I would like to express my deepest gratitude to my family for all the support during my entire studies.

Tom van de Water
Delft, July 2025

Abstract

The pursuit of sustainable and efficient air transport has led to increased interest in unconventional aircraft configurations, the Delft University Unconventional Configuration (DUUC) has shown potential. This concept combines the propulsion unit with the empennage and utilizes the synergy of these components. The so-called Propulsive Empennage (PE) consists of Ducted Fan Systems (DFS) which are two ducted propellers attached to the fuselage by a pylon with control vanes at the rear end of the duct. The feasibility of the DUUC has been investigated in previous studies, but a conclusive answer has not been formed where the potential is shown but an unfavorable design was the result. This thesis aims for optimize the existing methodology for analyzing the DUUC performance, benchmarking it against a conventional turboprop configuration, specifically the ATR72-600 and form a definitive answer on the feasibility of an aircraft employing a Propulsive Empennage.

The Integrated Aircraft Feasibility Model (IAFM) is set up to determine the feasibility of the DUUC concept. The IAFM is divided into two disciplines: aerodynamics and flight mechanics. An extensive literature review forms the basis of the improvements made to earlier analysis methods. The literature review comprises a state-of-the-art part for the DUUC aircraft including all relevant contributions from previous research. In addition, all important concepts of ducted fans are discussed as well as tail volume coefficients and requirements for static longitudinal and directional stability.

The aerodynamic section of the IAFM has been improved with the addition of an inflow correction for the duct that accounts for the flow change due to elevator deflection. The effect is small, but is included in the model for completeness. The nacelle performance model has been updated with the addition of a lift coefficient prediction based on an inclined body of revolution, where in previous studies the lift of the nacelle was ignored. The inflow angles for the support and control vanes are modified from the propeller slip calculation to a velocity vector approach based on the radial distribution of axial velocity calculated by a Blade Element Momentum model.

An empirical prediction for the thrust generated by the duct has been implemented in order to allow fast design iterations of the PE compared to the Ducted Fan Design Code that has been used before. The validation of this model shows good agreement with the experimental data. Additionally, the control vane load model has been adjusted to account for the difference in inflow angle based on the propeller swirl direction. This has shown a 25% reduction in control vane load that should be considered for control vanes in X-configuration.

For the flight mechanics model, the mass estimation of the pylon, support and duct have been modified. To allow for a better prediction based on structural requirements, the duct's mass prediction has been changed from a nacelle prediction to a horizontal tail prediction. As this resembles its function better. The pylon and support mass were previously sized on the basis of a percentage of the mass it had to carry. This method is improved by calculating the required weight based on the bending moment created by the aerodynamic load or the weight of the propulsion group.

The pendulum stability implications with respect to the addition of the PE have not been specifically treated yet, whilst it has a significant influence on the vertical center of gravity. Adding the empennage decreases the vertical moment arm and hence decreases the stabilizing contribution of the fuselage to the longitudinal stability.

Up to now, the control vane configuration of the PE has been an x-configuration which has been shown to be ineffective. An improved configuration has been proposed, but has not yet been analyzed. The control vanes would then be placed on the edge of the duct and would influence the lift contribution with a change in camber. This control vane model, called the duct edge, has been analyzed by means of Athena Vortex Lattice and demonstrated to be three times more efficient and approached the control regime of the reference aircraft.

A sensitivity study shows the effect of empennage position across the fuselage with respect to the center of gravity and requirements for empennage sizing. The pylon and duct sensitivity are demonstrated with respect to force contributions and mass estimations. But also with respect to stability and required restoring moments.

Two DUUC configurations have been set up and benchmarked with the reference aircraft. Configuration 1 has the PE on the conventional empennage position, while configuration 2 is placed in front of the wing and acts as a canard. The results of the IAFM show that both configurations do not outperform the reference aircraft due to an increase in weight, center of gravity excursion and additional trim drag. This forms a more definitive answer to the feasibility of the DUUC.

This work contributes to the broader effort to develop sustainable aviation technologies by providing a structured methodology to analyze an unconventional aircraft configuration employing a Propulsive Empennage. The DUUC serves as both a technical challenge and an opportunity to rethink traditional aircraft design in the pursuit of greener aviation.

Contents

List of Figures

List of Tables

Nomenclature

Acronyms

Acronym	Explanation
ac	Aerodynamic Center
AR	Aspect Ratio
ATR	Avions de Transport Régional
AVL	Athena Vortex Lattice
BEM	Blade Element Momentum
CBA	Cooperative Business Aircraft
CFD	Computational Fluid Dynamics
cg, CG	center of gravity
CFRP	Carbon Fibre-Reinforced Polymer
DFDC	Ducted Fan Design Code
DFS	Ducted Fan System
DUUC	Delft University Unconventional Configuration
FAR	Federal Aviation Regulations
FBD	Free Body Diagram
FEM	Finite Element Method
FG	Fuselage Group
GSR	Gap to Span Ratio
IAFM	Integrated Aircraft Feasibility Model
IRON	Innovative turbopROp configuratioN
KBE	Knowledge Based Engineering
KPI	Key Performance Indicator
LEMAC	Leading Edge Mean Aerodynamic Chord
MAC	Mean Aerodynamic Chord
MD	McDonnell Douglas
MTOM	Maximum Take-Off Mass
MZF	Mass Zero Fuell
OEM	Operational Empty Mass
OEI	One Engine Inoperative
OR	Open Rotor
pax	Passengers
PE	Propulsive Empennage
PHALANX	Performance, Handling Qualities and Load Analysis Toolbox
PW	Pratt and Whitney
Re	Reynolds number
RPS	Revolutions Per Second
SM	Static Margin
SR	Shrouded Rotor
SRV	Swirl Recovery Vane
VC	Vickers
WG	Wing Group

Greek symbols

Symbol	Explanation	Unit
α	Angle of attack	$[deg]$
β	Side slip angle	$[deg]$
β	Pitch angle of the propeller blade	$[deg]$
δ_e	Horizontal control vane deflection angle	$[deg]$
δ_r	Vertial control vane deflection angle	$[deg]$
ϵ	Downwash angle	$[deg]$
η	Efficiency factor	[-] or [%]
λ	Fuselage slenderness ratio	[-]
Λ	Taper ratio	$[-]$
ϕ	Propeller twist angle	$[deg]$
ϕ	Cant angle	$[deg]$
ϕ	Sweep angle	$[deg]$
ρ	Air density	$[kg/m^3]$
ρ_{alu}	Density Aluminum	$[kg/m^3]$
σ_{duct}	Expansion ratio duct	$[-]$
σ_{allow}	Allowable stress	$[N/m^2]$
τ	Thickness ratio wing profile	[-]
ζ	Correction factor	[-]

Latin symbols

Symbol	Explanation	Unit
a	Axial induction factor	[-]
b	Span	$[m]$
c	Chord	$[m]$
d	Diameter	$[m]$
D	Drag	$[N]$
e	Oswald efficiency factor	[-]
ff	Form factor	[-]
F	Force	$[N]$
f_M	Mach correction factor	[-]
g	Gravitational constant	$[m/s^2]$
i	Installation angle	$[deg]$
J	Advance ratio	[-]
l	Length	$[m]$
L	Lift	$[N]$
m	Mass	$[kg]$
M	Mach number	[-]
n	Number of blades	[-]
Q	Body volume of the nacelle	$[m^3]$
R	Radius	$[m]$
S	Surface area	$[m^2]$
t	Thickness	$[m]$
T	Thrust	$[N]$
V	Velocity	$[m/s]$
W	Weight	$[N]$
x	x-direction	$[m]$
y	y-direction	$[m]$
z	z-direction	$[m]$
$\bar{c}$	Mean Aerodynamic Chord	$[m]$
C_D	Drag Coefficient	[-]
C_{D_i}	Lift Induced Drag Coefficient	[-]
C_f	Friction Coefficient	[-]
C_L	Lift Coefficient	[-]
C_M	Pitching Moment Coefficient	[-]
C_N	Normal Force Coefficient	[-]
C_P	Power Coefficient	[-]
C_Q	Torque Coefficient	[-]
C_T	Thrust Coefficient	[-]
C_Y	Side Force Coefficient	[-]

Superscript and Subscripts

Super/subscript	Explanation
0	Initial state
α	With respect to angle of attack
β	With respect to side slip angle
ac	Aerodynamic center
allow	Allowable
alu	Aluminum
ax	Axial velocity
c/4	Quarter Chord Point
cg	Center of Gravity
cv	Control vane
d,D	Drag
dive	Dive
e	With respect to elevator deflection
eng	Engine
fus	Fuselage
ht	Horizontal tail
i	Indicates several components
in	Inflow
l,L	Lift
m,M	Pitching moment
max	Maximum
misc	Miscellaneous
n	Neutral point
N	Normal force
p,P	Power
PE	Propulsive Empennage
proj	Projected
prop	Propeller
Q	Torque
r	With respect to rudder deflection
ref	Reference
t,T	Thrust
tan	Tangential velocity
ult	Ultimate
vt	Vertical tail
w	Wing
wet	Wetted
∞	Freestream conditions

1

Introduction

The innovation in unconventional aircraft concepts is driven by critical concerns about the environmental impact of aviation and the global push towards sustainable transport solutions. With conventional aircraft concepts approaching their performance and efficiency limits, fundamentally different configurations show potential [2]. Among such emerging concepts is the Delft University Unconventional Configuration (DUUC), which integrates propulsion and control surfaces through a ducted-fan system. An artist impression of the DUUC is shown in Figure 1.1. This novel Propulsive Empennage (PE) approach replaces the traditional empennage with a configuration that utilizes the synergy between the propulsion and aerodynamic stability systems [1].

Figure 1.1: Artist impression of the DUUC [3]

In the 1980s, tail mounted propeller aircraft were already investigated [4] and the Clean Sky 2 initiative has also investigated this in the IRON project [5], illustrated in Figure 1.2 where innovative turboprop configurations are analyzed. History shows several examples of aircraft employing aft fuselage-mounted engines. Think about the VC10 [6], MD87 [7] and Embraer CBA-123 Vector [8], illustrated in Figure 1.3. Benefits of these configurations are the potential to reduced cabin noise due to the aft position, a clean wing concept because of the absence of the pylons and enhanced longitudinal stability. With aft mounted engines, application of additional thrust causes a nose down pitching moment compared to a nose up

pitching moment for a wing-mounted engine configuration. Disadvantages of the aft placement of the engines is the increased tail load because of the weight of the propulsive system at the tail.

Figure 1.2: Innovative aircraft configuration in the Clean Sky 2 project [9]

Figure 1.3: CBA-123 Vector in flight during the 1990 Farnborough air show [10].

The DUUC configuration, shows potential to be a viable alternative to wing mounted propeller configuration due to the interaction between the duct and propeller according to Vos [11]. This study showed an unfavorable fuel burn, but the drag estimates were conservative and the beneficial duct thrust effects were not taken into consideration. That could offset the drag making the aircraft concept a viable alternative. Furthermore, the integration of ducted propellers within the empennage, ducted propellers can achieve improved static thrust performance [12], enhanced control authority [13], and potentially lower noise emissions due to the shielding effects of the structure of the duct [14]. Another advantage of the compact integration of propulsion and control elements can be a reduction in operational empty weight according to Stavreva [15], thus improving aerodynamic efficiency. The ring-wing characteristics of the duct ring wing contribute to longitudinal stability.

However, despite these promising features, previous studies have shown significant challenges associated with the DUUC architecture. Key issues include the increased weight on the tail with its implications for aircraft balance due to aft-shifted center of gravity, and uncertainties in the aerodynamic interaction between the fan, duct, and airframe components. Furthermore, earlier studies initially deemed the DUUC unattractive in terms of overall performance, highlighting the need for an improved design according to van den Dungen and Stavreva [16, 15].

To address the gaps in previous studies, the current research seeks to revisit the feasibility of the DUUC concept by improving and extending earlier research on the DUUC. The purpose of this project is to evaluate the efficiency of the duct, validate the applicability of traditional tail volume coefficients for a Propulsive Empennage configuration, and establish design criteria for such an innovative empennage. Through a combination of theoretical modeling of the aerodynamic behavior and flight mechanics analysis, the research aims to quantify the performance trade-offs and identify configurations that might outperform conventional turboprop aircraft.

Ultimately, this work contributes to the broader objective of developing more sustainable aircraft concepts by systematically evaluating the potential and limitations of an aircraft employing a Propulsive Empennage. As such, the DUUC represents not only a technical challenge but also a vital step toward re-imagining future aircraft for a cleaner and more efficient aviation sector.

1.1. Research Objective

The objective of the research is to investigate the feasibility of the Delft University Unconventional Configuration aircraft by means of an aerodynamic and flight mechanical analysis. The main objective of this thesis can be summarized as follows.

> Determine the feasibility of an aircraft with Propulsive Empennage compared to a conventional turboprop aircraft. When it turns out to be not feasible, see what improvements/changes need to be undertaken to get a feasible aircraft. The feasibility is evaluated with respect to aerodynamic efficiency, performance and stability.

A set of research goals have been set up in order to breakdown the main objective.

- Determine whether the 'tail volume' concept can be used in the initial design procedure of an aircraft with propulsive empennage.
- Establish the design criteria for DUUC that can be related to the duct, pylon, and overall performance.
- Compare the performance of a novel DUUC concept with a traditional turboprop design.
- Evaluate the efficiency of the duct design and identify areas of improvement.
- Identify potential configuration changes of the DUUC V0.1 and determine its feasibility.

1.2. Research Questions

The research is guided by two main research questions:

> What is the feasibility of the DUUC aircraft concept with respect to aerodynamic efficiency, performance and stability characteristics compared to a conventional turboprop aircraft?
>
> How can the Propulsive Empennage be optimized to enhance aerodynamic efficiency, performance and stability compared to design iteration V0.1?

The main research questions can be answered by a set of sub-questions:

1. How can the conceptual sizing method of the tail volume coefficient be applied for the propulsive empennage of the DUUC?
2. What is the propulsive efficiency of an aircraft employing a Propulsive Empennage?
3. How does the performance of the DUUC configuration compare to a conventional turboprop configuration aircraft?
4. What improvements can be made to the Propulsive Empennage to enhance propulsive efficiency?
5. What are alternative positions of the Propulsive Empennage, and how does this affect the performance?
6. What are the implications with respect to the static stability of the aircraft when the Propulsive Empennage is used compared to a conventional turboprop?

1.3. Research Hypothesis

During the start of the project, the following hypotheses were defined based on the earlier studies and available literature.

The DUUC will have a higher OEM due to the addition of the duct and support.

The Propulsive Empennage will have a higher tail effectiveness due to the powered control.

The tail volume coefficient of the DUUC will be smaller because of the effectiveness of the Propulsive Empennage.

The DUUC will have a higher propulsive efficiency as a result of the additional thrust generated by the ducted propulsors.

The center of gravity excursion of the DUUC will be larger compared to a conventional turboprop aircraft.

Placing the Propulsive Empennage in front of the wing will enhance the aerodynamic performance of the DUUC.

1.4. Scope

To clearly define the research of the DUUC and to be able to answer the research question within the timeframe of the thesis, a scope has been established. Since the DUUC is still in a conceptual design phase, several assumptions have to be made and their implications have to be defined.

The following things are within the scope of the thesis:

- Improvement and extension of current aerodynamic and flight mechanics model for evaluating the DUUC.
- Evaluation of the Propulsive Empennage efficiency and aerodynamic forces by means AVL, XFoil and a BEM model.
- The feasibility of the DUUC concept will only be evaluated during cruise.
- The DUUC will be benchmarked against the ATR72-600 aircraft.
- The static longitudinal and static directional stability are evaluated.
- Determine the flight performance implications of the DUUC.
- Alternative positions of the Propulsive Empennage on the fuselage are evaluated.
- Sensitivity study on key design parameters inside the Propulsive Empennage.
- Design changes (like control vane configuration) are only evaluated in a conceptual method.

Because of the conceptual state of the aircraft design, which requires quick and (potentially) large design changes, the analysis does not suit itself to detailed full aircraft CFD or FEM analysis. Additionally, some other things are excluded from the feasibility analysis:

- Detailed design and weight estimation of the propulsion group inside the Propulsive Empennage.
- Noise analysis of the aircraft concept.
- Lateral stability effects.
- Effects with respect to aileron (roll) deflection.
- All flight conditions beyond cruise.

Hence, this thesis is limited to the aerodynamic and flight mechanics evaluation of the DUUC V0.1 concept, focusing on the integration and optimization of the Propulsive Empennage onto a regional turboprop aircraft framework. The work aims to provide a definitive assessment of the technical feasibility and performance trade-offs of the unconventional aircraft configuration in the limited resources and timeframe of this master thesis project.

1.5. Thesis Outline

The thesis is built up according to the flow scheme illustrated in Figure 1.4. The thesis starts with a part where background information is given. The DUUC definition described in chapter 2, includes an extensive review of the existing research into the DUUC and important definitions of the Propulsive Empennage. Next, a literature study is done in chapter 3 that treats all relevant topics with regard to ducted propellers and the flight mechanics behavior of the aircraft. In the next part of the analysis, the Integrated Aircraft Feasibility Model is setup in the methodology. A differentiation is made between the aerodynamic and flight mechanics part of the IAFM, found in chapter 4 and chapter 5, respectively. Both models are validated in their last sections. The third part of this document contains results in chapter 6. First, the DUUC empennage is compared with the conventional empennage of the ATR after which two configurations of the DUUC are compared with the baseline aircraft. Next, a study of the sensitivity of important parameters in section 6.3. The analysis is concluded in section 7.1 followed by recommendations in section 7.2.

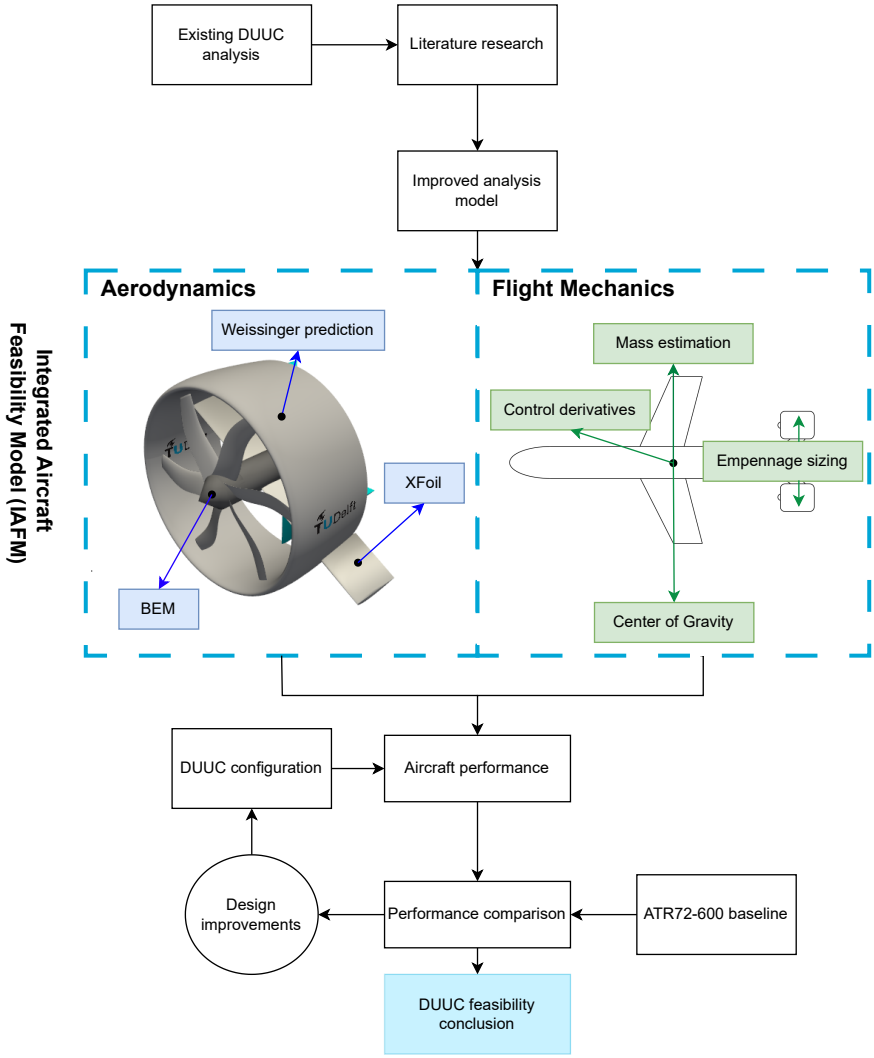

Figure 1.4: Flow chart of the thesis outline.

Part I
Background

2

DUUC Definition and Prior Work

The Delft University Unconventional Concept (DUUC) is an innovative aircraft design with a so-called Propulsive Empennage [1]. This empennage is sized for stability and control whilst also being the propulsive system on the aircraft [16]. The original shape of the wing-body was inspired by the Boeing 737-700 [11] and the mission profile is derived from the ATR72-600 [17]. The PE consists of two Ducted Fan System (DFS) which each are constructed from ducted propellors with control vanes at the rear end of the ducts. The propulsors are attached to the fuselage by two pylons. An artist impression by van Arnhem [1] of the DUUC is given in Figure 2.1.

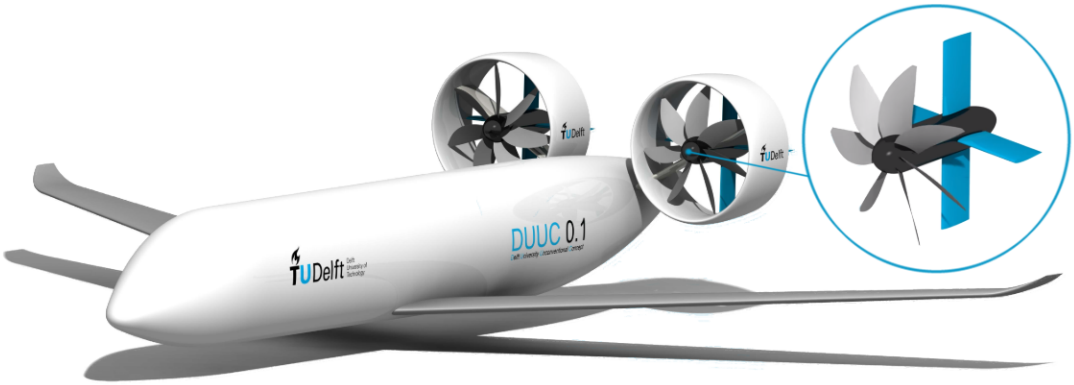

Figure 2.1: Artist impression of the DUUC V0.1 [1].

The DUUC has a harmonic mission profile of 1530 km with a payload of 7500 kg, as noted by Vos et al. [11]. The operating Mach number is between 0.4 and 0.6 as determined by the reference data of the ATR [18].

The innovative PE is built on the principle of synergizing the propulsive systems with directional and longitudinal control. Using a ducted propeller, the efficiency is increased at low speeds due to the limitations of tip vortices and decreased streamtube compression according to Pereira [19]. It also allows for the ability to vector the thrust with the control vanes at the rear end of the duct. An additional benefit of the DUUC would be the clean wing principle as the flow on the wing is not influenced by the wing-mounted engines and the reduced perception of noise inside the cabin as the engines are placed after the cabin as discussed by Stavreva [15].

The Propulsive Empennage of the DUUC V0.1 includes two ducted fans. Each ducted fan contains a duct, propellor, center body (core, including the engine), control vanes in horizontal and vertical

direction and a pylon, or support strut, attaching the propulsor to the fuselage.

The terminology of duct, ring wing, annular wing and shroud, illustrated in Figure 2.2a, are used interchangeably throughout this report. Similarly, for tail-off and tailless when discussing the stability and control of the aircraft, for which an illustration is shown in Figure 2.2b. The terms rotor and propeller, visualized in Figure 2.2c, are considered equal in all sections.

(a) Illustration duct, ring wing, annular wing and shroud.

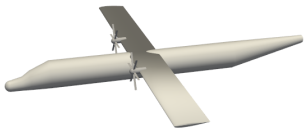

(b) Illustration tail-off and tailless.

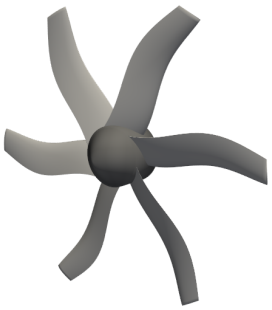

(c) Illustration rotor and propeller.

2.1. Previous Research

The DUUC V0.1 has been topic of various studies, addressing aerodynamic performance, structural sizing and mass estimations. Stability and control requirements must be satisfied and handling qualities should be sufficient. Their findings are presented in this section.

The unconventional configuration with Propulsive Empennage was implemented in the initiator design code by van den Dungen [16]. This has been used to compare the DUUC with the ATR72-600. The horizontal and vertical tail surface was found to be undersized due to the tail volume coefficient, which did not scale during the design iterations. The positioning of the wing for longitudinal static stability and trim was found to be a challenge for the DUUC due to the high tail load. The performance of the DUUC shows an increase in OEM of +17.4%, +12.9% fuel mass and +11.2% MTOM, considering the harmonic mission profile. A reduction in parasite drag is visible, but that is diminished by an increase in trim drag adding up to 14% additional drag during flight, compared to the ATR72-600 [16].

The aerodynamic performance of a ducted propeller system has been investigated by Harinarain [13]. No general relationship has been found between thrust (setting) and lifting force as this depends on the shape of the duct. The control vanes have been found to be less effective compared to conventional rudders and elevators. After the onset of stall of the duct, the control vanes will not lose effectiveness. It became apparent that at low inflow velocities the total thrust to power ratio was increased after which it decreases [13].

Hameeteman [20] created a parametric model in ParaPy (Knowledge Based Engineering software [21]) that has been used to create input files for extensive CFD analysis. The extracted data set has been used by Hameeteman for flight mechanics simulations to assess its handling qualities. The thrust has a significant effect on all components inside the duct and shows an increase in lift with increasing thrust. The vertical control vane, duct, and center body show a decrease in drag regardless of the elevator deflection. The placement of the ducted propulsors aft and above of the center of gravity line contribute to a stabilizing effect. However, this placement shifts the center of gravity aft and directly destabilizes the aircraft. Requiring more trimming efforts and hence more trim drag [20].

When a fuselage-mounted ducted propeller configuration is designed with the same top-level aircraft requirements as conventional aircraft, it demonstrates a feasible design with respect to performance and stability. For a harmonic mission of 1530 km, it shows an increase in fuel burn of 12% and a larger excursion of the center of gravity due to the aft position of the propulsion group [11].

The thrust-elevator interaction research has shown the non-trivial flight mechanics behavior that occurs due to the effectors interaction. This clearly distinguishes the DUUC from a conventional engine-tail

aircraft. It also showed an increase in control effectiveness (of the control vanes) in a throttle-up situation [17].

Stavreva [15] set up a way to structurally size the Propulsive Empennage in order to estimate the weight of the empennage in more detail. Take-off, cruise, and dive are used as critical design conditions in the sizing process. The design of the duct, made of aluminum, had a mass less than half of what was predicted by empirical relations. When the material is changed to CFRP, a mass reduction of 70% is achieved. A Kevlar inner liner has been added for blade containment in case of a blade loss. The pylon mass was originally underestimated by empirical methods; a reduction in weight can again be made by changing the material to CFRP.

Varying duct sizes have been studied and it was observed that the drag is larger for smaller ducts at low angles of attack, which can be explained by the control vanes inside the duct. At larger angles of attack, the drag of the larger ducts becomes more dominant compared to the control vanes. For a stable design, it is proposed that the wing position is at 47.5% of the fuselage length. Placing the Propulsive Empennage forward by 20% of the fuselage length leads to a smaller excursion of the center of gravity [22].

2.2. Important Definitions

Some definitions in this report are used differently in other papers or are important to understand the principles. They are defined in this section to clarify the explanation and to ensure a clear baseline for comparison. The most important definition is the definition of the Propulsive Empennage, Ducted Fan System and component specification inside the Propulsive Empennage, given in subsection 2.2.1 and subsection 2.2.2, respectively.

2.2.1. Propulsive Empennage and Ducted Fan System

When speaking about the Propulsive Empennage, it includes two Ducted Fan Systems which include the components mentioned in subsection 2.2.2. It is important to understand that this system aims to provide propulsion and stability to the aircraft. The PE is illustrated in Figure 2.3a and one DFS is shown in Figure 2.3b.

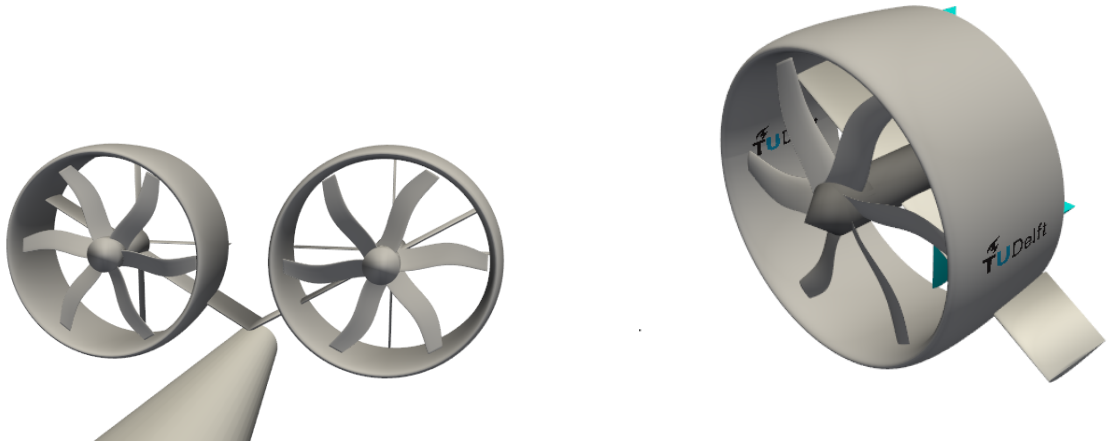

(a) Conceptual illustration of the Propulsive Empennage (PE).

(b) Conceptual illustration of a Ducted Fan System (DFS).

Figure 2.3: Simplified drawings of the Propulsive Empennage definition

2.2.2. Propulsive Empennage Components

The duct is a circular wing illustrated by the blue area in Figure 2.4a, the duct is axisymmetric. The pylon is the component that connects the duct to the fuselage, illustrated by Figure 2.4b. The structural component inside the duct, which mounts the propulsor and acts as a structural body for the duct is named support strut and is visualized in Figure 2.4c. The nacelle enclosing the propulsor is shown in Figure 2.4d. The propeller includes the spinner hub and is depicted in Figure 2.4e. Lastly, the control vanes located at the rear end of the duct, seen in Figure 2.4f, include the elevators and rudders.

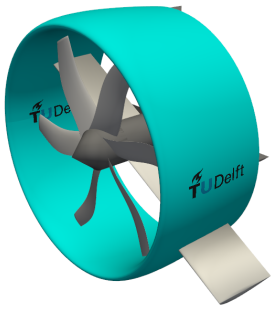

(a) Duct.

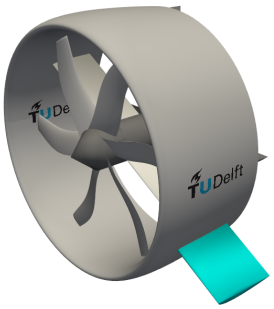

(b) Pylon.

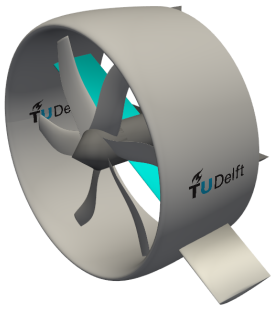

(c) Support strut.

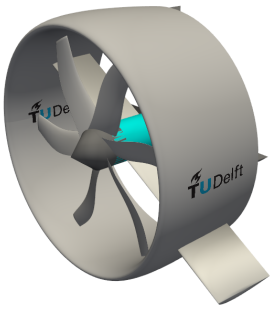

(d) Nacelle.

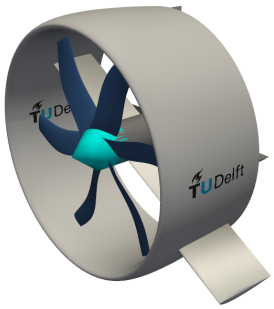

(e) Propeller.

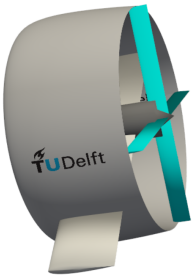

(f) Control vanes.

Figure 2.4: Conceptual component illustration of the components in the DFS.

The different cross-sectional areas are required to determine the inflow velocity at different components. The cross-sectional area including their station numbers are shown in Figure 2.5 which is only used to define the station numbers per component. Depending on the airfoil shape of the duct, the diameters at each cross section change.

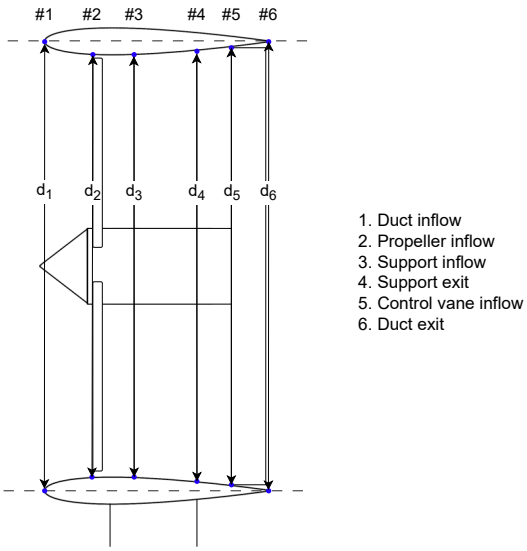

Figure 2.5: Station numbers inside the duct including diameter number definition drawn in a conceptual DFS design.

2.2.3. Aspect Ratio

The Aspect Ratio (AR) of a duct has been defined in various ways throughout different researches on this topic in the past. Ribner [23] used Equation 2.1 to define the aspect ratio, where R [m] represents the radius of the duct and c [m] the chord of the duct. Fletcher [24] has improved this definition using the inner diameter of the duct. In this research, the duct diameter is taken between the two center lines of the duct airfoils and the aspect ratio is defined as Equation 2.2. The chord is taken parallel to the center line of the annular airfoil. Figure 2.6 illustrates the definition that will be used throughout this research.

$$AR = \frac{8 \cdot R}{\pi \cdot c_{duct}} \tag{2.1}$$

$$AR = \frac{d}{c} \approx \frac{d_{duct}}{c_{duct}} \tag{2.2}$$

2.2.4. Cant Angle

The cant angle of the PE is defined as ϕ in Figure 2.7. This angle determines the position of the DFS relative to the fuselage.

2.2.5. Advance Ratio

The non-dimensional parameter, advance ratio J, is used to relate the airspeed to the movement of the propeller, Equation 2.3. Where the Revolutions Per Second is defined by RPS, d_{prop} [m] the propeller diameter and V_∞ [m/s] the free-stream airspeed. The advance ratio is also used to define the efficiency of a propeller in Equation 3.3 [25].

$$J = \frac{V_\infty}{RPS \cdot d_{prop}} = \frac{V_\infty}{RPS \cdot d_2} \tag{2.3}$$

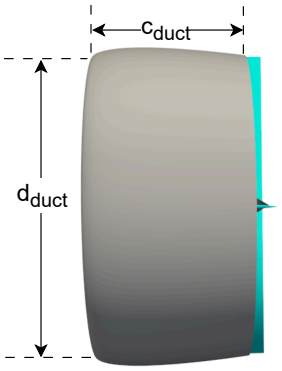

Figure 2.6: Aspect Ratio definition for the DFS.

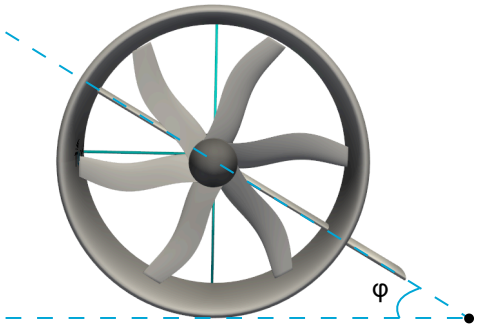

Figure 2.7: Definition of the cant angle.

2.3. DUUC V0.1

The current DUUC version (V0.1) has a duct which is an annular wing with NACA0012 profile. The pylon and support a have similar airfoil profile, whilst the control vanes are created from NACA0016. The propeller modeled in the DUUC V0.1 is the F568-1 propeller installed in the turboprop engine Pratt and Whitney 127 that is used in the ATR72-600. The geometric characteristics of DUUC V0.1 are given in Table 2.1 that have been used by Varriale [17] for a longitudinal control study. The Ducted Fan System is installed with a cant angle of 30 degrees with respect to the fuselage as described by Varriale [17].

Table 2.1: DUUC V0.1 geometry as used by Varriale [17].

Description	Symbol	Value	Unit
Wing span	b	34.3	m
Mean aerodynamic chord	c	3.96	m
Fuselage length	l_{fus}	34.5	m
Wing area	S	103.5	m^2
Empennage duct radius	R_{duct}	2.27	m
Empennage duct chord length	c_{duct}	2.27	m
Empennage cant angle	ϕ	30.0	deg
Aircraft mass	m	38.1 $\times 10^3$	kg

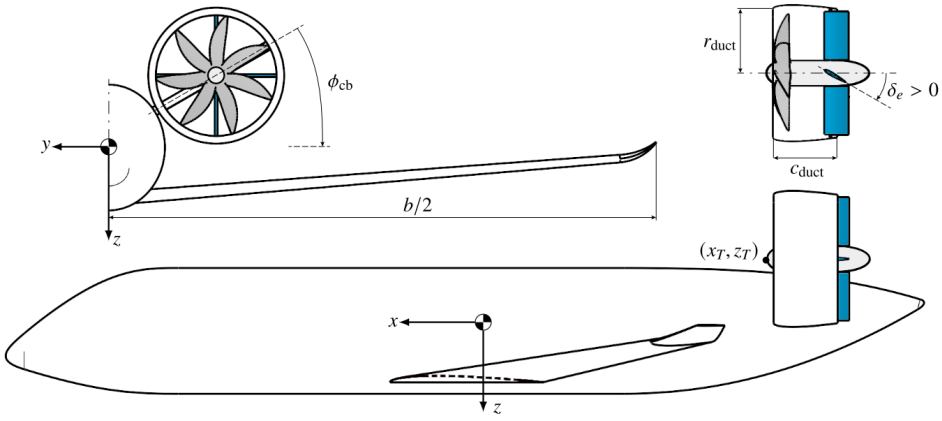

Figure 2.8: DUUC geometry with body reference system defined by Varriale [17].

2.4. Reference Systems

Throughout this thesis, different reference systems are used for the definition of forces, components and motion derivatives. This section aims to explain and illustrate the different reference systems used.

The stability and control derivatives including the aircraft resultant forces are defined in the body reference system as illustrated in Figure 2.8. For determining the center of gravity, the object reference system with zero point is used at the bottom of the fuselage and the nose of the cockpit. This system is illustrated in Figure 2.9. The aerodynamic forces are defined in the flow axis system that is depicted in Figure 2.10

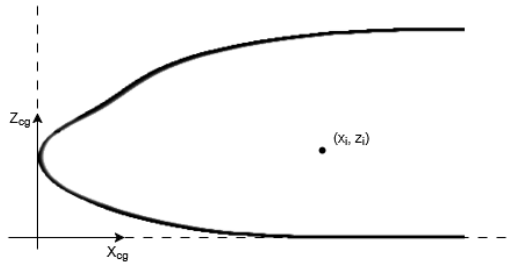

Figure 2.9: Object reference system used to determine the center of gravity of the aircraft.

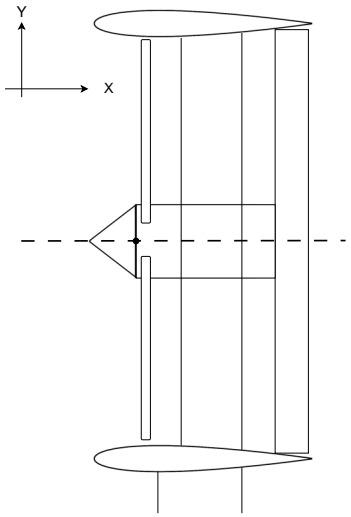

Figure 2.10: Flow reference system used to determine the aerodynamic forces of the Propulsive Empennage and aircraft.

3

Literature Review

In this chapter, a literature review is done on all components of the ducted propulsor in terms of their performance and relevant aspects. First the potential benefits of the DUUC aircraft are treated. The propeller is treated after in section 3.2 followed by the duct in section 3.3. The pylon is the last element investigated in section 3.4. In section 3.5, the sizing methods for a conventional empennage and their implications for the DUUC are described. The requirements and relevant relations regarding stability and balance are also discussed in the section about empennage sizing.

3.1. Potential benefits of the DUUC

Besides the benefits of using a ducted propeller there are some additional benefits of the DUUC V0.1 design on aircraft level are mentioned in this section.

Noise shielding

Placing a duct around the propeller has the benefit of shielding the radiated noise. With a proper acoustic liner, a noise reduction can be achieved, especially during take-off and landing according to Dittmar [14]. This has a beneficial effect on passenger comfort in the cabin, but also on the environment in and around airports. One must be critical in weighting this potential benefit as Oleson and Patrick [26] have shown that the addition made the ducted propeller louder because of the strong rotor stator interaction.

The placement of the propellers at the back of the fuselage also improves the passenger comfort in terms of noise in the front part of the cabin. The noise benefits of the DUUC V0.1 have not yet been explicitly investigated.

Advantage of a clean wing

When engines are mounted on the wing, interference effects occur in the flow around the mounting location. The interference drag increases between the pylon, nacelle and wing which leads to an increase in aircraft drag [27]. The wing-mounted engine also has an effect on the sectional angle of attack of the wing. With a rear-mounted engine, and thus having a clean wing, improves the performance of the wing [28].

Flight path steepness

The control vanes directly behind the propulsion source allow for the vectoring of the thrust. Using this ability, the exit flow of the engines can be directed such that an airbrake is created. This allows for a steeper flight path, which improves flight performance. This is a conceptual thought for the DUUC and has not yet been researched.

3.2. Propeller

The performance of the propeller depends on multiple factors and will be defined. The effect of the gap between the rotor tip and the duct is explained. The control vanes and pylon inside the duct can act as a swirl recovery system.

3.2.1. Aerodynamic Performance

The aerodynamic performance of the propeller can be measured with multiple parameters common in literature. The power and thrust coefficients C_P and C_T, Equation 3.1 and Equation 3.2 respectively, are used to determine the propulsive efficiency η_p, Equation 3.3. The torque coefficient C_Q is also a valuable parameter, Equation 3.4. The total thrust is the combined thrust of the propeller and the duct. The air density of the free flow is represented by ρ, while the revolutions per second are given by n.

$$C_P = \frac{P}{\rho \cdot n^3 \cdot D_{prop}^5} \tag{3.1}$$

$$C_T = \frac{T_{total}}{\rho \cdot n^2 \cdot D_{prop}^4} \tag{3.2}$$

$$\eta_p = \frac{C_T}{C_P} \cdot J \tag{3.3}$$

$$C_Q = \frac{Q}{\rho \cdot n^2 \cdot D_{prop}^5} \tag{3.4}$$

The isolated performance of the DUUC V0.1 propeller, F568-1 has been simulated by Filippone [29]. The propeller flight envelope is illustrated in Figure 3.2 where the optimum operating line is represented in blue. The lines of constant propulsive efficiency and collective pitch are also given in the figure.

When the performance of an open rotor is compared to that of a propeller inside a duct, some clear differences can be observed. The normal force gradient of the ducted propeller is much steeper with increasing airspeed compared to an open rotor, according to Pereira [19]. The ducted propeller also delivers more thrust in the same power range compared to the open rotor, this is depicted in Figure 3.1. This statement is also based on the research of Martin and Tung [30]. The dashed line is the line that combines the thrust of the propeller and duct. For both the open rotor and the ducted fan cases, the power consumption decreases with increasing airspeed, the power consumption of the ducted fan always stays lower than in the open rotor case, as experimentally studied by Pereira and Cai [19, 31].

Pereira [19] has experimentally shown that the effects of a change in angle of attack and airspeed on propeller forces and moments are magnified by adding a duct around the propeller. This has also been confirmed by Abrego [32].

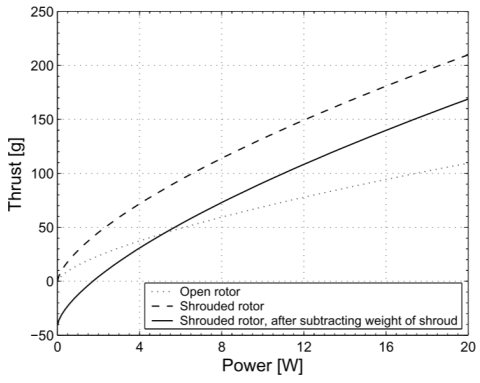

Figure 3.1: Thrust comparison for an open and shrouded rotor with a 6.3-inch propeller [19].

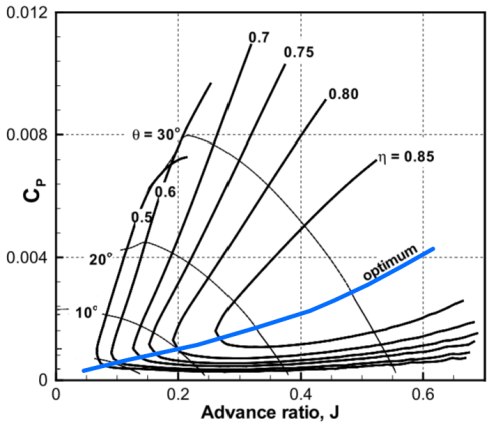

Figure 3.2: Power coefficient versus advance ratio of the F568-1 propeller with six blades, at various collective pitch values [29].

Tip Loss

The movement of the propeller blade is correlated with the energy losses concentrated at the tip of the blade. This loss has a consequence of an increase in power consumption. Because the propeller blade has a finite length, a vortex is induced due to the high pressure below the blade that wants to flow to the low pressure area on top of the blade. This vortex reduces the effective circulation, causing an

energy loss that requires additional power from the engine. The tip loss comprises about 25% of the total energy loss and includes the movement of the tip vortex and the interaction between the wake and the vortex [33].

In propeller design, a tip-loss correction can be applied that has been developed by Prandtl. This correction is necessary when comparing an open rotor case with a ducted propeller. The loss in circulation depends on the effective incoming flow, the 2D airfoil polars, and the radial position. The Prandtl tip loss correction at a particular radial position is given in Equation 3.5. The parameter d is represented by Equation 3.6. Here, the number of blades is given by B, and a is the axial induction factor [25]. A loss in circulation also occurs near the rotor hub as the vortex shed by the hub influences the blade sections in close proximity. This loss can also be modeled by mirroring Equation 3.5.

$$f_{loss}\left(\frac{r}{R}\right) = \frac{2}{\pi} \cdot arccos\left(e^{\frac{-\pi \cdot \left(\frac{1-r}{R}\right)}{d}}\right) \tag{3.5}$$

$$d = \frac{2\pi}{B} \cdot \frac{1-a}{\sqrt{\lambda^2 + (1-a)^2}} \tag{3.6}$$

When considering ducted propulsion, the annular wing acts as an end plate at the tip of the blade. This effect, called end plate effect, can be compared to winglets on aircraft wings but is not one-to-one comparable. The end plate effect only applies when the clearance between the tip and the annular wing is small enough. This effect lowers the tip losses as the lift-induced drag component is reduced.

The effect of increasing the clearance between the duct and the tip of the blade has been numerically analyzed by Yongle [34], An [35] and many more researchers. This has also been validated experimentally by Fletcher [24] and Black et al. [12]. It was found that, at low advance ratios, there is a linear relationship between an Gap to Span Ratio (GSR) and a decreasing thrust and torque coefficient (Figure 3.3a and Figure 3.3b). The GSR is measured as a percentage of the blade radius. At higher advance ratios, the GSR ratio decreases first, after which it increases (Figure 3.3c); this can be explained by reversed pressure at the leading edge. With an expansion of the gap, the vortex structure changes from a shed vortex to one big separation vortex. The blade loading and vortex structure affect each other at the trailing edge. The propulsive efficiency as illustrated in Figure 3.3 is defined as Equation 3.3 and represents the total efficiency of the ducted propulsor.

An important relation between the tip gap and duct thrust was found. The thrust of the duct increases with a smaller tip gap. This performance increase can be correlated to the breakdown of the tip vortex into an increased axial velocity in the duct [36, 24, 12].

Black et al. [12] experimentally showed an average increase in thrust at a fixed flow speed, M = 0.4, and propeller advance ratio. It showed a slight decrease at M = 0.5, which can be attributed to the interaction between the boundary layer of the duct and the tips of the propeller blade. Increasing the gap consistently shows a lower performance at low Mach numbers.

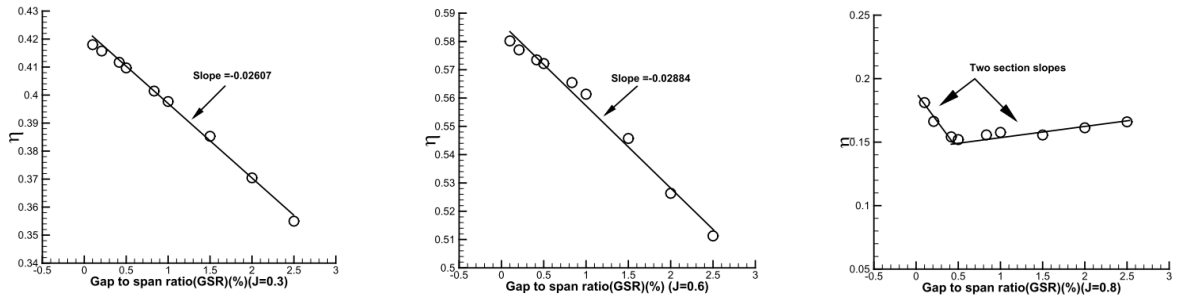

(a) GSR (%) for an advance ratio of 0.3.

(b) GSR (%) for an advance ratio of 0.6.

(c) GSR (%) for an advance ratio of 0.8.

Figure 3.3: Numerical relationship between efficiency and tip clearance for a ducted propeller (d = 240 mm) [34].

3.2.2. Swirl Recovery

Depending on the propeller design and operating conditions, swirl losses in the propeller slipstream can be up to 10% [37]. When the disk loading increases, swirl losses increase and the efficiency of the propeller decreases. Subsequently, a potential mitigation for this is the use of Swirl Recovery Vanes (SRV). As the inner part of the pylon and the control vanes are in the propeller slipstream, they could serve the purpose of a stator for swirl recovery.

Wind tunnel experiments have shown efficiency increases around two percent with static SRVs [38]. Numerical solutions demonstrate the potential for an efficiency increase of up to five percent using the same configuration [39]. The distance of the recovery vanes to the propeller determines the efficiency gains as the vanes block the flow behind the propeller. This will limit the flow capacity and increase the incidence angle of the blade sections. This increases the blade load, which enhances the swirl losses in the slipstream [40].

The effect of SRVs has mostly been studied for open rotor systems [41]. Li et al. [42] has studied the aerodynamic performance and interaction of the swirl recovery vanes inside a ducted propeller. His research showed that an increase in propulsive efficiency of up to 5.08% can be achieved. The SRVs have a coupled flow interference with the duct and the blade that results in reduced thrust and power consumed by the blade. This loss is compensated with the thrust generated by the swirl recovery vanes. The velocity contour comparison, provided in Figure 3.4, shows a lower velocity near the leading edge of the duct without SRVs.

(a) Duct velocity contour without SRV

(b) Duct velocity contour with SRV

Figure 3.4: Velocity contour comparison at hover with and without a SRV for a ducted propeller. With a propeller speed of 8000 rpm and inflow velocity equal to 0 m/s [42].

An additional benefit of the swirl recovery vanes is the torque generation in opposite direction of the counter-torque created by the propeller. The research of Li [42] has also shown a counter-torque reduction of up to 63.1% for a particular case, which could be beneficial for the structural sizing of the pylon.

3.3. Duct

The duct, which can be seen as a circular wing, has two main functions in the context of the PE. One is the generation of a lifting force and secondly the flow contraption around the propeller. Another function of the duct, is that it is able to generate some static thrust at low inflow velocities. This section describes the aerodynamic performance of the duct, the streamtube compression when a propeller is placed inside the duct and the critical design parameters related to the duct.

3.3.1. Aerodynamic Performance

The aerodynamic performance of the duct is split up in a lift and drag component and the moment induced by the duct.

Lift

The lift curve slope of annular wings has been studied numerous times in the past where experimental data is compared with different theoretical models for high and low aspect ratio wings and for different planforms. Ribner [23] has established the first basis for theoretical modeling for annular wings, although

the advantages of non-planar wings were known much earlier from the work of Prandtl [43]. Ribner has found that a circular wing has double the lift compared to a planar flat wing that spans the diameter. The lifting line theory was applied on the annular wing to find get to this conclusion. Fletcher [24] has experimentally studied annular wings of different aspect ratios (d_{duct}/c_{duct}) and has come to the conclusion that the lift curve slope of an annular wing is double that of a planar wing. This shows good agreement between Fletcher and Ribner.

Maqsood [44] has studied the theoretical prediction models for C_{L_α} with the experimental data for annular wings of different aspect ratios. This study, of which the results are shown in Figure 3.6, has concluded that the Weissinger prediction model for elliptical planforms match the experimental results the most. It must be noted that these methods are only based on linear lift-curve assumptions and hence ignore nonlinearities. In the Weissigner prediction model, the lift curve slope of the annular wing is calculated using Equation 3.7. Where $\zeta_{annular}$ is determined using Equation 3.8 and C_{l_α} is the lift curve slope of the 2D airfoil section that is used inside the annular wing.

$$C_{l_{\alpha,annular}} = \frac{\pi}{2} \cdot \zeta_{annular} \cdot C_{l_{\alpha,2D}} \tag{3.7}$$

$$\zeta_{annular} = \frac{1}{1 + \frac{\pi/2}{AR} + \frac{tan^{-1}\left(1.2 \cdot \frac{1}{AR}\right)}{AR}} \tag{3.8}$$

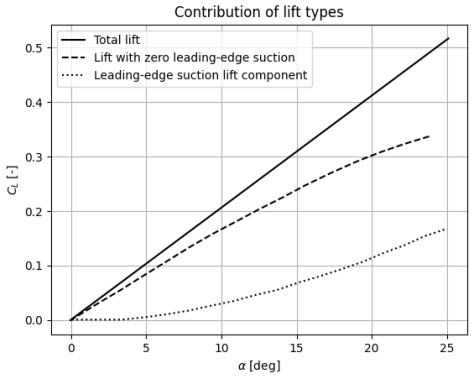

Figure 3.5: Contribution of potential and vortex lift effects [44].

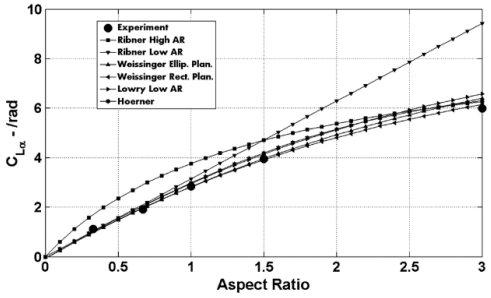

Figure 3.6: Comparison of lift-curve slope with different theoretical models for various aspect ratios [44].

When applying the leading edge suction analogy to the lift prediction of annular wings, the overall lift can be parametrized into a pressure-induced and vortex-induced contribution. This concept of Polhamus [45] is based on the fact that the total lift is a sum of the potential flow lift and the lift associated with leading/side-edge vortices. Lamar [46] has extended the concept so that the side-edge vortices also contribute to the vortex lift. The potential lift can be estimated using Equation 3.9, where K_p has been obtained using empirical techniques according to [44]. The vortex lift equivalent to the leading edge suction force can be written as Equation 3.10, where K_v is a constant. The different contributions to the lift coefficient are shown in Figure 3.5.

$$C_{l,p} = K_p \cdot sin(\alpha)cos^2(\alpha) \tag{3.9}$$

$$C_{l,v} = K_v \cdot cos(\alpha)sin^2(\alpha) \tag{3.10}$$

When the values for K_p are set to twice the values that are usual for elliptical and rectangular wings, the results in Figure 3.7a are obtained. This formulation suggests that the vortex lift is about a third for the annular wing compared to the planar configuration. The pressure-induced lift is thus about twice as high compared to the planar situation. This is also in agreement with the research of Ribner [23].

Maqsood [44] has determined a numerical formulation for the lift of an annular wing that closely matches the experimental data. Equation 3.11 is used, which is a combination of Equation 3.9 and Equation 3.10, where the value of K_v remains constant at $\pi/3$ and K_p is determined by Equation 3.12. The aspect ratio used in this equation is 1.62 and $K_{p_{max}} = 6.25$. This formulation matches the experimental data accurately in the pre-stall regime. The comparison between theory and experimental data is shown in Figure 3.7b.

$$C_L = K_p \cdot sin(\alpha) \cdot cos^2(\alpha) + K_v \cdot cos(\alpha) \cdot sin^2(\alpha) \tag{3.11}$$

$$K_p = K_{p_{max}} \cdot sin\left(\frac{AR}{2}\right) \tag{3.12}$$

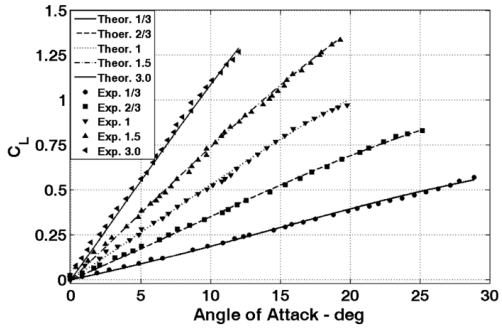

(a) Lift comparison between the Polhamus [45] suction analogy and experimental data obtained from Fletcher [24] by Maqsood [44].

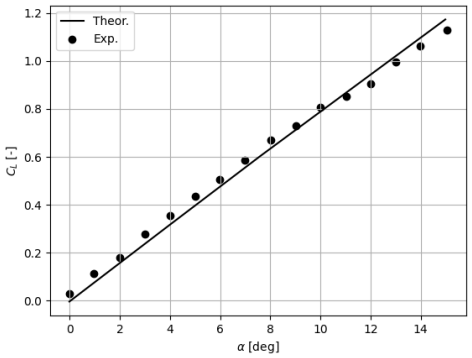

(b) Comparison C_L - α: theory versus Equation 3.11 [44].

Figure 3.7: Validation of theoretical prediction of lift coefficient for annular wings [44].

One of the benefits of an annular wing compared to a rectangular wing is the delay of stall. Kanoria [47] has determined this computationally, but also Fletcher [24] noticed this during wind tunnel experiments. Stall leads to the shedding of vortices and flow separation, but the stall form tends to be benign. Fletcher [24] has observed that for high aspect ratio ring wings, the stall behavior becomes more abrupt, as is depicted in his results in Figure 3.8a.

Anderson [48] has investigated the propeller location with respect to the duct. In the below-stall region, there is not much difference between the different configurations of propeller inside the duct. After the onset of stall, the difference between a tractor and pusher configuration become larger. For the pusher configuration, separated flow from the annular wing hits the propeller which causes uneven loading, resulting in a reduced propeller effectiveness according to Anderson [48]. The pusher configuration does delay stall marginally but the tractor configuration has a much bigger effect. As this configuration re-energizes the boundary layer, it delays stall significantly in a low power case. Figure 3.8b illustrates the effect of stall with different propeller locations compared to a case without the propeller.

Aerodynamic moment

One of the parameters required for the longitudinal static stability analysis is the aerodynamic moment of the ducted propulsor around the aerodynamic center of the aircraft. Werle [49] has devised a method that determines the moment around the aerodynamic center of the duct itself in Equation 3.13.

$$C_m = C_{mc} + \frac{4}{3 \cdot \pi} \cdot A \cdot \alpha_0 \cdot C_{L/Y} \tag{3.13}$$

If the duct were to be treated as a nacelle, Torenbeek [50] would provide a statistical method to determine the aerodynamic moment of duct on aircraft level for fan-based engines. This method is found in Equation 3.14 and does not vary with engine parameters. A more accurate method of predicting the pitching moment coefficient for the duct is required to properly analyze the performance.

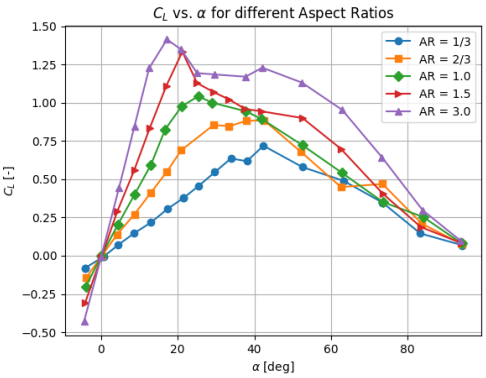

(a) Variation of lift coefficient with angle of attack for various aspect ratio ring wings [24].

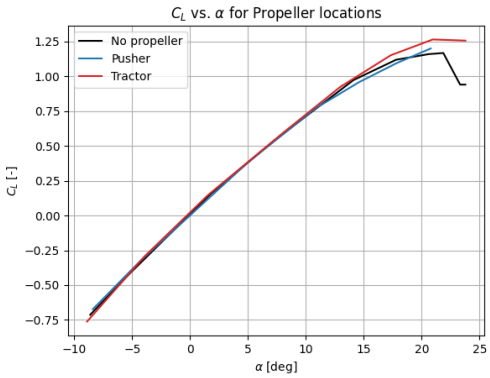

(b) Variation of lift coefficient with angle of attack for different propeller locations [48].

Figure 3.8: Variations in lift coefficient including onset of stall for different aspect ratio wings and different propeller locations.

$$C_{m_{\text{ac,nacelle}}} = \begin{cases} -0.05 & \text{for } z_{cg} - z_{eng} \geq 0 \\ 0.02 & \text{for } z_{cg} - z_{eng} < 0 \end{cases} \tag{3.14}$$

Lamar [46] has proposed a method to determine the pitching moment coefficient for nonplanar wings. This method is given in Equation 3.15, where x_p and x_e are represented by Equation 3.16 and Equation 3.17, respectively. The results are depicted in Figure 3.9 where the experimental results of Fletcher [24] are compared with the leading edge suction analogy formulation of Lamar. This shows a good agreement between the theoretical prediction and the experimental data. Figure 3.10 shows a more detailed prediction by Maqsood [44], the values used in the equations are: $a = 0.3$, $b = -0.786$, $c = -0.26$ and $p_1 = 0.63$, $p_0 = -0.35$. Only at an angle of attack of 9° is the prediction off which can be attributed to the way x_e is predicted.

$$C_M = x_p \cdot K_p \cdot sin(\alpha)cos(\alpha) + x_e \cdot K_v \cdot sin^2(\alpha) \tag{3.15}$$

$$x_p = a \cdot AR^b + c \tag{3.16}$$

$$x_e = p_1 \cdot AR + p_0 \tag{3.17}$$

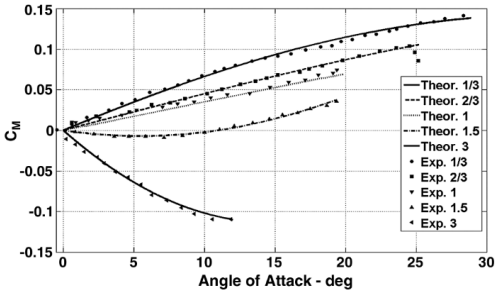

Figure 3.9: Pitching moment comparison between experimental [24] and Lamar [46] suction analogy [44].

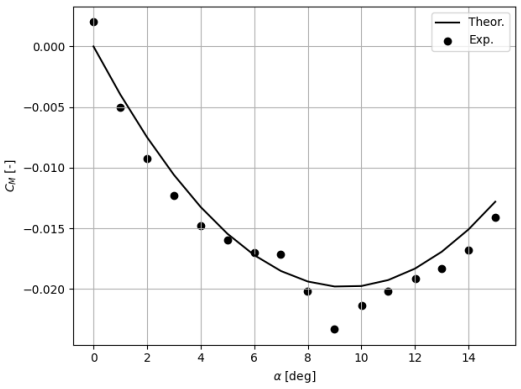

Figure 3.10: Comparison C_m - α: theory versus Equation 3.15 [44].

Drag

Fletcher [24] realized that the gradient of the induced drag of the annular wing is half that of a planar wing, which can also be concluded from Figure 3.11 from Raymer [51]. The induced drag for the annular wing is defined in Equation 3.18.

$$C_{D_i} = \frac{C_L^2}{2 \cdot \pi \cdot AR} \tag{3.18}$$

Compared to the advantages with respect to lift mentioned previously, an annular wing has more wetted area and is hence expected to have a larger zero-lift drag. Traub [52, 24] showed that the beneficial induced drag is offset by the larger zero-lift drag. Traub [53] concluded from this that annular wings are aerodynamically more efficient than planar wings, since the drag increase does not follow the same scale as the increase in lift as can be observed in Figure 3.12.

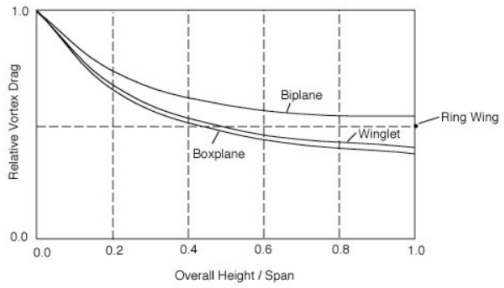

Figure 3.11: Induced drag variations over height/span for nonplanar wings [51].

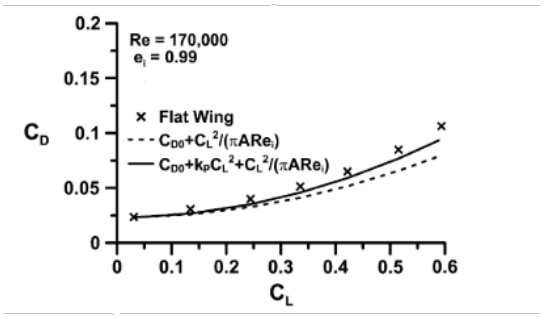

Figure 3.12: Drag polar comparison between flat wing and annular wing [53].

However, Wan [54] places a critical note when examining the performance of annular wings that the lift and drag coefficients are compared when using the projected surface area. The actual surface area of the ring wing is π times larger. Therefore, it cannot be assumed that the performance of the annular wing is superior to that of a flat, planar wing.

When investigating the interaction between the duct and the propeller, Black [12] noticed that the duct drag slowly decreases with increasing rotational speed of the installed propeller as well as in power loading. This can indicate that the axial pressure forces compensates for the increase in viscous drag [12]. In general, it can be stated that at low inflow velocities the duct contributes to the net thrust, but at higher inflow velocities the duct will decrease the net thrust.

In setting up a numerical relation to predict the drag of an annular wing, Lamar [46] has found that the drag can be predicted by Equation 3.19. The factor K depends on the aspect ratio as can be observed in Equation 3.20. Figure 3.13 shows the comparison between the theoretical prediction of duct drag and the experimental data [44].

$$C_D = C_{D_0} + K \cdot C_L^2 \tag{3.19}$$

$$K = a \cdot (AR)^b \tag{3.20}$$

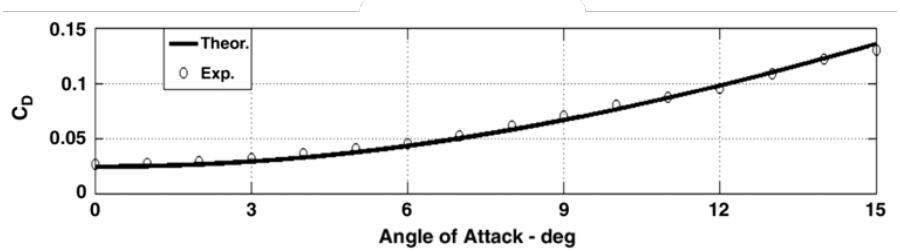

Figure 3.13: Comparison C_D - α: theory versus Equation 3.19 [44].

A suggested performance improvement for annular wings is the application of stagger. Traub [53] has researched the effect of stagger on an annular wing and its effect on the lift and drag coefficients. The negative stagger illustrated in Figure 3.14, has shown a significant reduction in the minimum drag coefficient. In addition, a reduction in pressure drag was also found. The lift coefficient was similar to the un-staggered situation. The nose-up pitching moment for a negative staggered situation is much stronger than without stagger. The drag reduction can be related to the reduction of the laminar separation bubble while displacing it further aft. Thus, applying a stagger to the duct of the Propulsive Empennage could reduce the drag of the empennage. However, the interaction of a staggered duct with a propulsor has not yet been researched in detail.

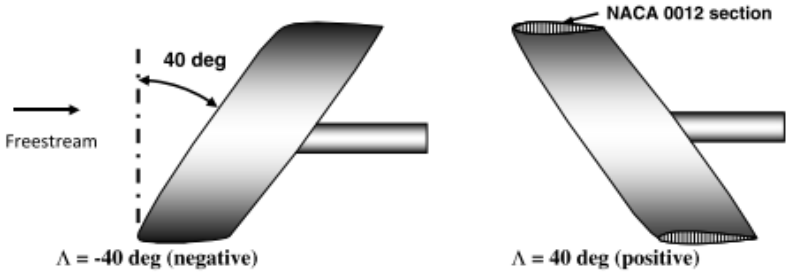

Figure 3.14: Diagram of the experimentally tested staggered ducts. Left: negative stagger of 40 degrees, right: positive stagger of 40 degrees [53].

3.3.2. Streamtube Compression

The main performance increase of ducted propulsion lies within the principle of restricting the natural contraction of the flow after the propeller. Using the actuator-disk model combined with conservation laws and momentum theory shows that the velocity increase in the wake is twice the induced velocity at the propeller. The conservation of mass then shows that the contraction of the slipstream is inversely proportional to the increase in velocity [25]. Depending on the duct shape, the slipstream inside the duct is forced to keep the same cross-sectional area or potentially increase. When the flow remains attached to the surface of the duct, the velocity increase at the far wake can be reduced, hence reducing the power requirements of the propeller [19]. For this theory to hold, it should be noted that within the momentum theory it is assumed that the slipstream is fully expanded to ambient pressure. The expansion ratio σ_{duct} in Equation 3.21 is therefore an important parameter in ducted propulsion.

$$\sigma_{duct} = \frac{A_{exit}}{A_{prop}} \tag{3.21}$$

This expansion ratio can be used to determine the total thrust of the ducted propulsor by using Equation 3.22 [19]. A correction factor K_{thrust} is added to this equation to correct for viscous effects and other deviations from the theoretical derivation. The exact value of this correction factor has to be determined.

$$\frac{T_{prop}}{T_{total}} = \frac{1}{2 \cdot \sigma_{duct}} \cdot K_{thrust} \tag{3.22}$$

Apart from the increase in thrust due to streamtube compression, the duct itself will generate a small portion of thrust at low inflow speeds and depends on the inflow angle. This thrust is generated because of an increased suction area around the leading edge of the duct and is the largest in static conditions. Figure 3.15a shows the flow streamlines in a ducted propulsor at static conditions. Black [12] has experimentally determined the thrust generated by the duct and the pressure distribution is depicted in Figure 3.15. The thrust component rapidly decreases into a drag component with increasing inflow speeds. However, an additional thrust component under near-static conditions can be beneficial for power loading in take-off conditions.

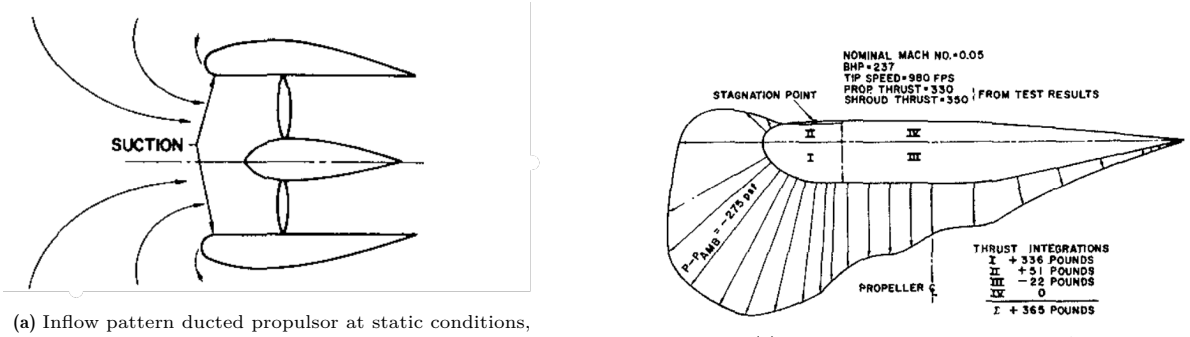

(a) Inflow pattern ducted propulsor at static conditions, with no slipstream contraction.

(b) Pressure distribution duct profile.

Figure 3.15: Duct pressure distribution at M = 0.05 with a propeller thrust of 330 pounds [12].

3.3.3. Duct Design Parameters

There are several design parameters that influence the performance of the duct. The airfoil profile/shape determines flow characteristics and enhances or reduces interference effects.

- **Aspect ratio -** similar to unswept wings, lower aspect ratio annular wings have larger maximum lift-drag ratios. This also applies to the wake characteristics of airfoils [24].
- **Duct diameter -** determines the size of the fan inside the duct and thus also affects the thrust generation of the PE. Together with the chord of the annular wing, it determines the aspect ratio mentioned above. The duct diameter is also linked to the weight of the duct and hence influences the stability of the aircraft.
- **Position of the rotor -** the location of the propeller inside the duct affects the flow inside the duct and affects the streamline compression and swirl recovery inside the duct. Moreover, the position of the rotor inside the duct also determines the expansion ratio that the duct has. This has an effect on propeller thrust generation as explained by Pereira [19].
- **Camber/airfoil shape -** is one of the factors that determines the expansion factor in Equation 3.21 and affects the lifting performance of the annular wing.

3.4. Pylon and Support

The pylon and the support strut are the parts that connect the ducted fan and the propulsion system to the fuselage. The design of this component aims to keep drag and weight to a minimum without losing structural integrity. The pylon also houses critical systems like fuel lines, electrical harnesses and potentially hydraulic components.

3.4.1. Structural Sizing

The pylon connects the engine to the wing or, in the case of the DUUC, to the fuselage. This structural purpose implies that it needs to withstand the forces and moments induced by the propulsor. The applied loads, together with the equipment to fit in the pylon, are the sizing factors for the pylon and support strut. A weight estimation specifically for a pylon specifically is not available, the weight is generally included in the empirical nacelle mass estimations, for example Equation 3.23 where the nacelle mass $[lb]$ depends on the take-off thrust, according to Torenbeek [50].

$$m_{nacelle} = 0.065 \cdot T_{take-off} \tag{3.23}$$

Specifically for the DUUC, the pylon is completely outside the duct, whilst the support is fully inside. The position of the ducted propulsor with respect to the fuselage has implications for the structural sizing of the pylon. Vos [11] concluded that there is a strong resemblance with the weight estimation of horizontal tail planes and the pylon for the Propulsive Empennage. Assuming that the surface is fixed and not swept, Equation 3.24 applies. Where V_{dive} $[kts]$ is the dive speed. This equation shows that the diving speed and surface of the pylon are driving factors and are based on statistical data from conventional aircraft. Also note that the primary function of the pylon is not to provide stability [11].

$$m_{pylon} = S_{pylon} \cdot (3.81 \cdot S_{pylon}^{0.2} \cdot V_{dive} - 0.287) \tag{3.24}$$

For a more detailed weight estimate of the pylon, in the conceptual design stage, should consider the loading conditions at take-off, diving, crash landing and propeller blade loss [15]. The primary loads expected in static loading are high bending stresses and shear loads. Vibrations should also be taken into account for the blade loss condition. The more detailed sizing is considered outside the scope of the research.

3.4.2. Aerodynamic Performance

The geometry of the pylon significantly influences the flow patterns around the junction with the connected surfaces. Generally, this is the wing, but in the case of the DUUC it is the duct and fuselage. Fairings are typically used to reduce super velocities and decrease the possibility of a local shock wave according to Vos [55].

The additional drag resulting from the interference between the two surfaces can be determined by the method described by Hoerner [56]. A difference is made between a T-junction and a plane-junction in Equation 3.25 and Equation 3.26, respectively. The main difference is the fact that on a T-junction, there is flow on the other side of the wall behind the junction. Whilst for the plane-junction there is no flow behind the wall. A schematic representation is shown in Figure 3.16a and Figure 3.16b, respectively.

$$C_{d,interference} = 17 \cdot \left(\frac{t}{c}\right)^2 - 0.05 \tag{3.25}$$

$$C_{d,interference} = 0.8 \cdot \left(\frac{t}{c}\right)^3 - 0.0003 \tag{3.26}$$

When the pylon and the support are treated as a fixed dihedral finite wing, it will provide a small contribution to the lifting capacity of the empennage. When considering the DUUC, with a dihedral angle of 30°, the part between the duct and the fuselage can be considered a V-tail. Because of this high dihedral, the lifting contribution is considered small and potentially neglible.

The asymmetric downwash effect from the wing can cause a destabilizing lateral moment on the Vee-tail. At high dihedral angles, the longitudinal moment curves will increase with the risk of creating a 'loop', which can compromise the moment balance of the aircraft. However, since the dihedral angle is between 20°-45°, this will not be considered a problem according to Zhang [57].

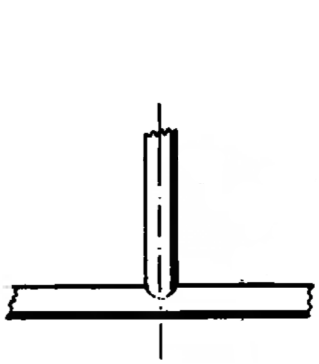

(a) Schematic view of a T-junction used to calculate the interference drag between the surfaces [56].

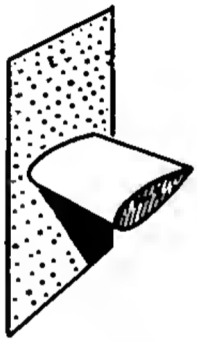

(b) Schematic view of a plane-junction used to calculate the interference drag between the surfaces [56].

Figure 3.16: Schematic representation of the distinct junction types for calculating interference drag.

3.5. Empennage Sizing

The design of a traditional empennage, consisting of a horizontal and vertical tail surface, is done with the purpose of providing stability and control of the aircraft [58]. The explicit functions that the empennage performs are:

1. To provide static and dynamic stability,
2. To enable control of the aircraft, through movable parts,
3. To provide a state of equilibrium in each flight condition.

The tail planes are built from a static lifting surface and a control surface that both contribute to the main functions. It is important to note that a trim device or way of trimming should be present in order to accommodate the equilibrium state in each flight condition. In this section, the procedure of sizing of the empennage is explained by means of the initial sizing method with the tail volume coefficient and based on a higher order method. In addition, longitudinal and directional static stability will be treated.

3.5.1. Tail Volume Coefficient

The tail volume coefficient is a non-dimensional parameter involved in the preliminary design phase where the tail size is estimated based on statistical data. This method of sizing for planar wings multiplies the ratio between the surface of the horizontal tail and the wing by the length of the tail arm, l_{HT} and l_{VT}, respectively. This tail arm length is normalized with the mean aerodynamic chord ($\bar{c}$). The tail volume coefficient for the horizontal tail is given in Equation 3.27. A similar approach is used to size the vertical tail surface: however, the tail arm length is normalized by the wing span (b) of the aircraft. The equation is shown in Equation 3.28 setup by Scholz [59]. Torenbeek [50] argues that the controllability of the aircraft is directly related to the tailplane volume.

$$C_{ht} = \frac{S_{ht} \cdot l_{ht}}{S_w \cdot \bar{c}} \tag{3.27}$$

$$C_{vt} = \frac{S_{vt} \cdot l_{vt}}{S_w \cdot b} \tag{3.28}$$

The tail arm lengths are defined from the center of gravity of the aircraft to the aerodynamic center of the tail surface, Figure 3.17. Similar-sized aircraft are used to determine a range of the tail volume coefficients in the design process. The value of the horizontal tail volume coefficient ranges between: $0.5 < C_{ht} < 1.2$, where a value around 0.8 is considered good according to Kumar [60]. Similarly for the vertical tail: $0.05 < C_{vt} < 0.10$ with a value of 0.07 considered good [61]. It should be emphasized that the surface area obtained through the tail volume coefficient does not directly imply a stable and trimmable design as it is a method to conceptually determine the required surface area.

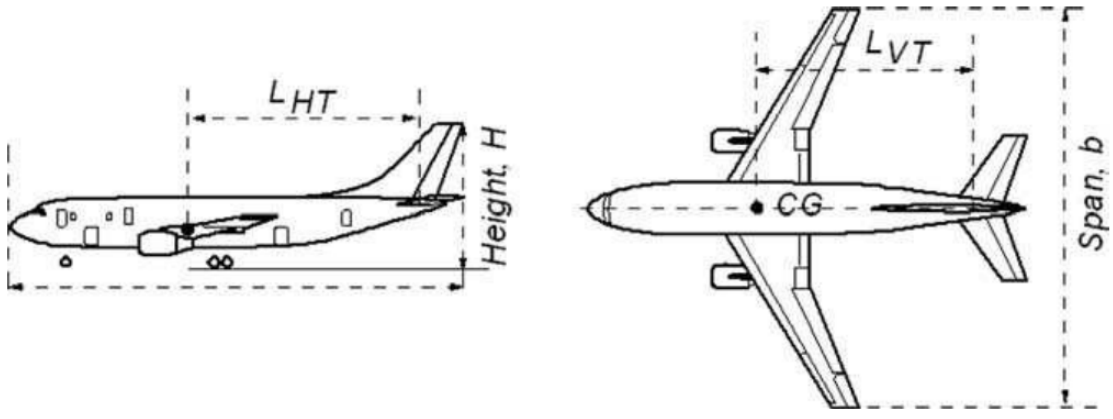

Figure 3.17: Tail lever arms for tail volume coefficient [60].

For the DUUC reference aircraft, the tail volume coefficients are given in Table 3.1. The ATR72-600 does have a T-tail configuration which result in different tail volume coefficients than a Boeing 737-700

for example. Airplanes with a T-tail configuration tend to have a lower C_{vt}, as the horizontal tail surface acts as an end plate of the vertical tail surface [60]. However, the Boeing 737 has a lower C_{vt} which can be attributed to the difference in wing configuration between the two aircraft.

Table 3.1: Tail volume coefficient for DUUC reference aircraft.

Reference aircraft	C_{ht}	C_{vt}
ATR72-600 [62]	1.050	0.119
Boeing 737 - 700 [61]	0.919	0.081

The horizontal tail effectiveness of the horizontal tailplane can be determined by multiplying the tail volume by the aerodynamic efficiency of the surface (C_{L_α}). This results in Equation 3.29. A way to determine this for the PE is taking the projected surface of the PE and input that as the horizontal tail surface, according to van den Dungen [16].

$$\eta_{ht} = \left(\frac{S_{ht} \cdot l_{ht}}{S_w \cdot \overline{c}} \right) \cdot C_{L_\alpha} \tag{3.29}$$

The fan thrust effects, aerodynamic contributions of the ducts, supports and pylons are included in the lift gradient of the PE. In the work of van den Dungen [16], it is concluded that the tail effectiveness of a planar tail cannot be directly equated to the effectiveness of the Propulsive Empennage. This would result in unrealistic values for the AR of the duct. Design changes in the AR of the duct will influence both the projected surface area and the lift curve slope of the tail. The question that arises is whether using a projected surface area of the tail in the tail volume coefficient is a representative way of sizing the duct in the Propulsive Empennage.

3.5.2. Higher Order Method

Torenbeek [50] argues that longitudinal stability is primarily affected by the area ratio between the horizontal tail and the wing. The requirement for the area ratio leads to the aerodynamic limits of the center of gravity of the aircraft. This plot can then be combined with the center of gravity limits of the airplane without horizontal tail. This leads to the X-plot in Figure 3.18. This plot explains the combination of the minimum tail area required to balance the aircraft combined with the best wing positioning.

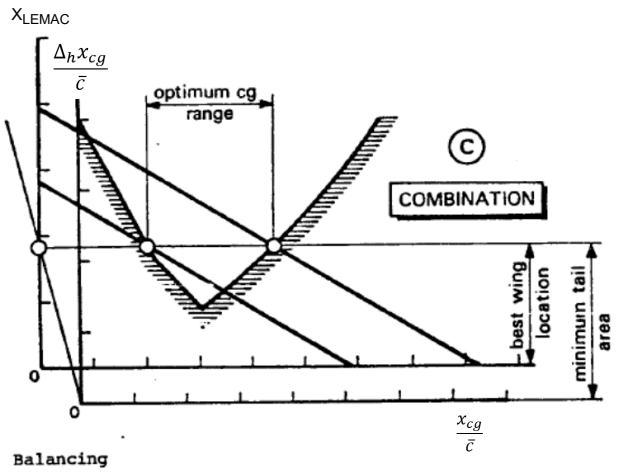

Figure 3.18: Balancing the airplane [50].

This method relies primarily on the force and moment balance of the aircraft. This method cannot be applied to unconventional configurations without making changes. It should be noted that the tailless

aircraft that Torenbeek considers does include a propulsion group on the wing. Additionally, the area ratio between the tail and the wing is considered a free variable, which has not been the case for the DUUC in previous design iterations.

The Performance, Handling Qualities and Load Analysis Toolbox (PHALANX), developed by the TU Delft, is a flight dynamics simulation model used for advanced analysis. This tool has been used by van den Dungen [16] to model the DUUC and compare it with the ATR72-600 baseline. Figure 3.19 illustrates the results that show the changes in the location of the center of gravity during flight. This shows that the center of gravity shift of the DUUC in the harmonic mission has a completely different shape compared to the ATR.

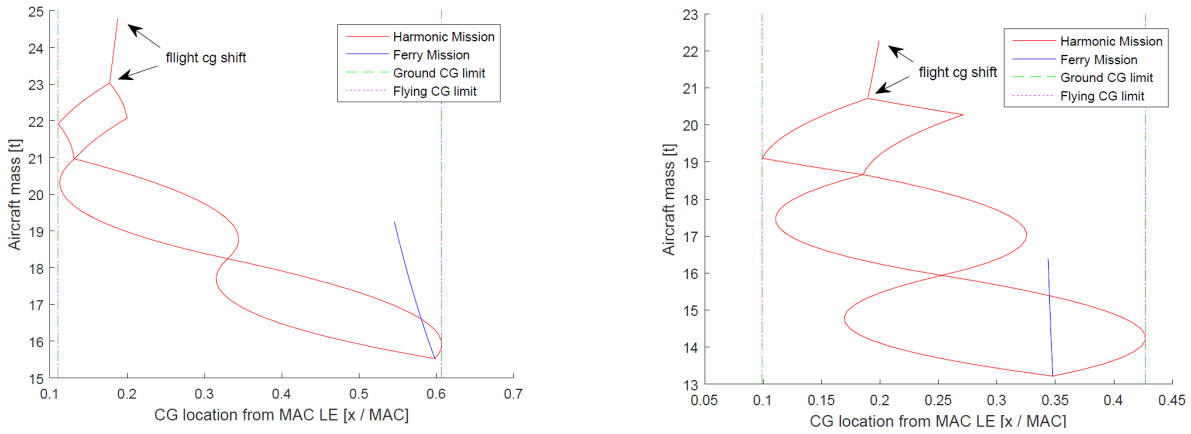

(a) Center of gravity shift DUUC.

(b) Center of gravity shift ATR72-600

Figure 3.19: Center of gravity shift comparison [16].

3.5.3. Longitudinal Static Stability

To be able to determine the longitudinal static stability requirements and relations for the DUUC, the first step is determine the how this is done for conventional aircraft. Figure 3.20 illustrates the forces and moments that play a role in a conventional aircraft configuration with respect to longitudinal static stability.

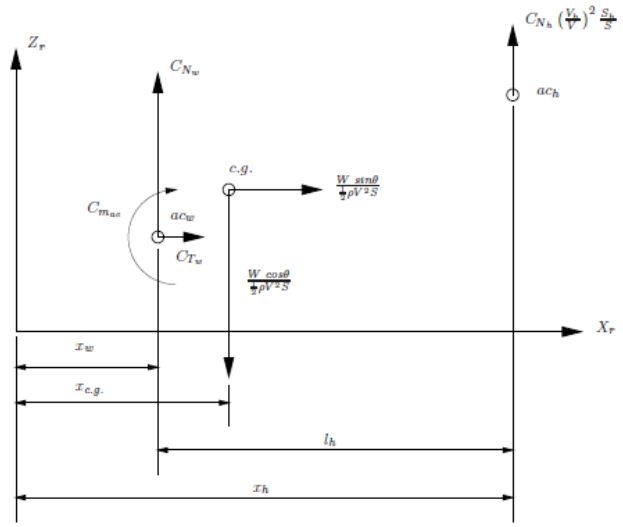

Figure 3.20: Simplified FBD of the forces and moments for equilibrium in a conventional aircraft configuration [63].

A translation step can be performed for the DUUC in Figure 3.21 based on the information from the previous research of van den Dungen [16]. From both FBD's the sum of forces in x- and z-direction can

be made as well as the moment definition about the y-axis.

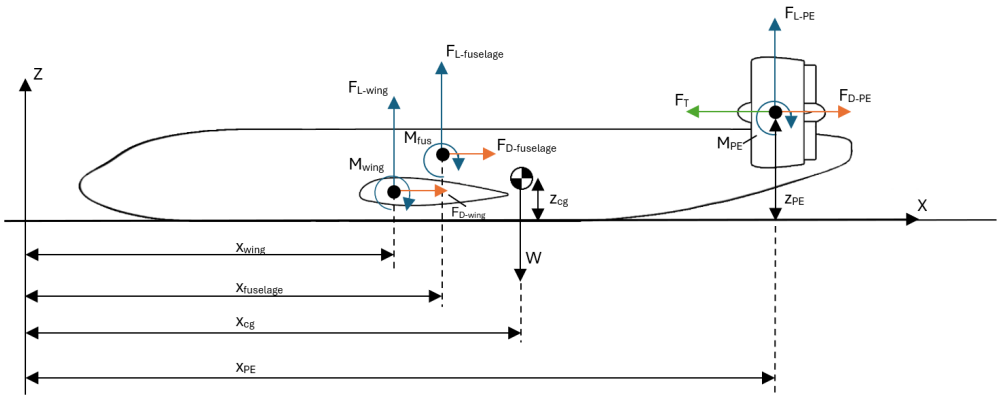

Figure 3.21: Free Body Diagram DUUC with force and moment definition used in LSS.

To have longitudinal static stability, the force balance requires a body that generates a moment around the center of gravity of the aircraft to counteract the moment generated by the wing and fuselage [50]. Usually this is done by the horizontal stabilizer but in case of the DUUC should be done by the complete Propulsive Empennage which has some implications with respect to the conventionally applied relations.

The moment coefficient around the aerodynamic center without the tail is usually built up from a contribution from the wing, fuselage and nacelles as defined by Mulder et al. [63]. Care must be taken in the bookkeeping of these components for the DUUC. The nacelle contribution is not present in the case of the DUUC if the tail is removed. This contribution relates the frontal area of the fan with a drag-induced moment, as can be concluded from Equation 3.15.

Similarly, the location of the center of gravity without the tail is determined using contributions from the wing, fuselage, nacelles and thrust [63]. Van den Dungen [16] found that the nacelle contribution, which refers to a vertical force, is already implemented in the tail moment calculation and therefore is set to zero.

When examining Figure 3.22, the trimmed condition is shown as point A. Disturbances in the form of a small change in angle of attack change the lift forces on the aircraft and tail. By definition, the stick-fixed neutral point is the center of gravity at which $dC_M/d\alpha = 0$, assuming a constant elevator angle. For static stability, the center of gravity must be before the neutral point to achieve the condition in Equation 3.30 according to Torenbeek [50].

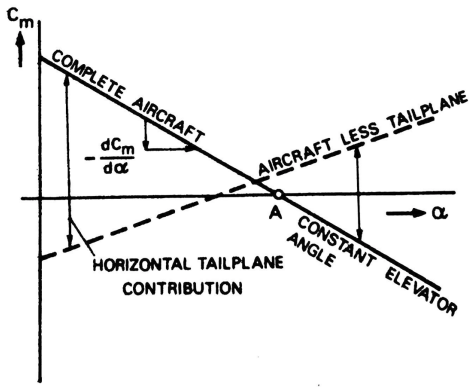

$$\frac{dC_m}{d\alpha} < 0 \qquad (3.30)$$

Figure 3.22: Pitching moment curve and trimmed condition [50].

The location of the center of gravity relative to the neutral point provides the static margin. The static margin is expressed as in Equation 3.31. It should be noted that the horizontal tail volume coefficient as discussed in subsection 3.5.1 is represented in this equation. The influence of the thrust is assumed to be negligible in this relation according to Torenbeek [50] for low engine aircraft. But as the ATR reference aircraft is a high wing aircraft with engine mounted wings, the thrust effect should be included as this will introduce a stabilizing moment.

$$\frac{x_n - x_{cg}}{\bar{c}} = \frac{C_{L_{ht_\alpha}}}{C_{L_\alpha}} \cdot \left(1 - \frac{d\epsilon}{d\alpha}\right) \cdot \frac{S_{ht} \cdot l_{ht}}{S \cdot \bar{c}} \left(\frac{V_{ht}}{V}\right)^2 \tag{3.31}$$

The position of the Propulsive Empennage has a significant effect on the moment balance based on the tail lever arm but also on the location of the center of gravity. In this report, alternative positioning of the empennage and their effect will be investigated.

3.5.4. Directional Static Stability

Static direction stability is related to the restoring moment that is generated when the aircraft is in a side-slip condition. The coefficient C_{n_β} represents this stabilizing moment and, for good handling qualities, should be positive. This coefficient has contributions from the wing, fuselage, vertical tail, nacelles and pylons for conventional aircraft as setup by Mulder et al. [63]. The PE will also have to generate a restoring moment. When the coefficients are combined for the entire aircraft, Equation 3.32 is found.

$$C_{n_\beta} = C_{n_{\beta_{PE}}} + C_{n_{\beta_w}} + C_{n_{\beta_{fus}}} \tag{3.32}$$

A special case should be treated in terms of directional stability. Namely, the One Engine Inoperative (OEI) condition, where, as the name implies, one of the engines is not operating. A FBD of an aircraft in OEI condition is shown in Figure 3.23, it should be observed that there is an asymmetric thrust production and the inoperative engine is producing a drag component. The yawing moment created by this can be counteracted by the empennage. For the PE, it must be considered that if one of the DFS is inactive, the control vanes have a different effectiveness and might even be unusable. This should be incorporated into the analysis of the required moment as well as the different operating condition of the working engine. Adib [22] has shown that the rudder loses effectiveness with an increase in the advance ratio.

From a design perspective, the outboard position of the PE will determine the moments and required rudder force, and thus its positioning limits will be researched in this report.

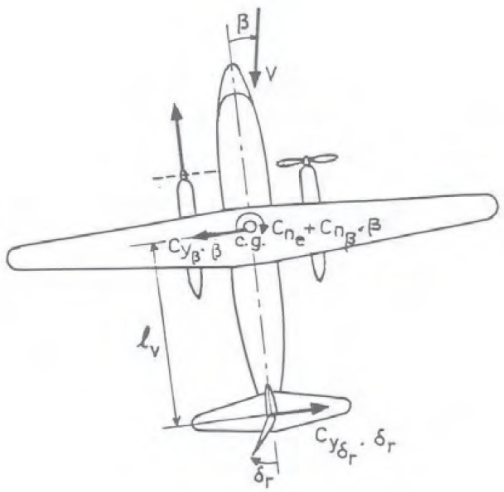

Figure 3.23: FBD aircraft in OEI condition with asymmetric thrust and restoring moment [63].

Part II

Methodology

4

Aerodynamic Model

The aerodynamic performance of the Ducted Fan Systems and Propulsive Empennage within the IAFM will be determined by semi-empirical relations. All components of the DFS are treated separately and the definition/terminology of Figure 2.4 is used. The first step is to determine the inflow properties for the components, after which the zero-lift drag is defined followed by the lift induced drag. The lift, drag and pitching moment are calculated and the thrust for per DFS is explained. The definition for the propulsive efficiency is given with an explanation of the reference frame.

4.1. Bookkeeping

Before the aerodynamic model is setup it is important to understand the force bookkeeping that is done. Table 4.1 explains the definitions of lift, drag and thrust with respect to the DFS. A graphic illustration of the force definition is shown in Figure 4.1. The forces are defined in the flow-axis system.

Table 4.1: Force bookkeeping for the aerodynamic model with respect to the DFS.

Force	Explanation
Lift	The lift force for the DFS is defined as the sum of all the forces in y-direction. As defined in Figure 4.1a.
Drag	The drag force is defined as a sum of all the forces in positive x-direction for the DFS. This does not include the subtraction of a thrust force which would be in negative direction. The definition is illustrated in Figure 4.1b.
Thrust	The thrust force is defined as the sum of forces in negative x-direction for the DFS. This includes a combination of contributions from the duct and propeller. This is shown in Figure 4.1c.

4.2. Inflow Properties

In order to setup the aerodynamic relations, the first step is to determine the inflow properties per component. For the components inside the DFS, a differentiation is made between a 'power-on' and 'power-off' situation which represents the engine being active or not. In this section the inflow angle and velocity is determined. The results for a test case at a velocity of 128 meters per second, which is equal to the free stream condition during cruise of the reference aircraft and an angle of attack of 5 degrees is given in Table 4.2, respectively. All values are taken at half the radial position of the blade. It is a major simplification but it is assumed that value at that position is the average across the blade, to allow for a more engineering approach of calculating the coefficients.

Duct

The inflow of the duct is influenced by the flow field created by the wing. The downwash created by the wing's bound and trailing edge vortices result in a corrected inflow angle that can be calculated using

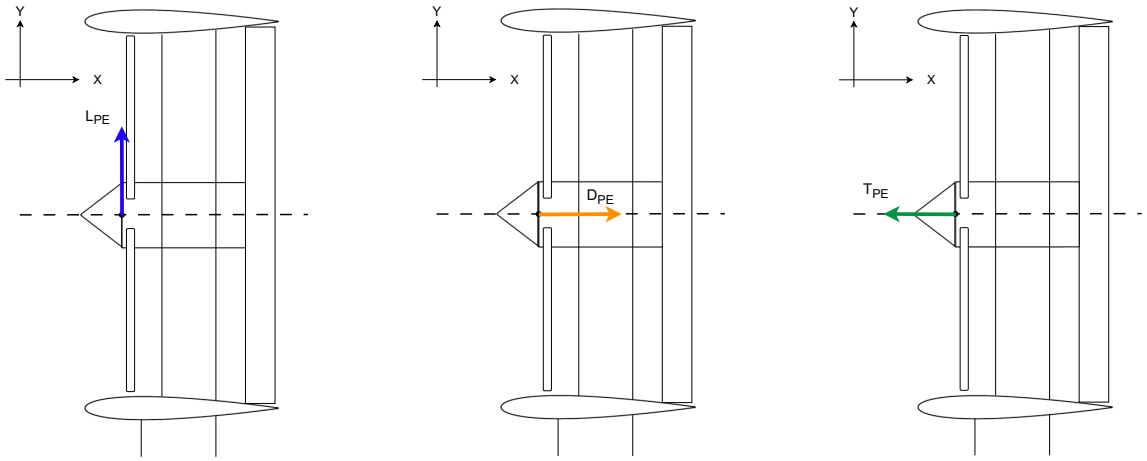

(a) Lift force definition for the DFS. **(b)** Drag force definition for the DFS. **(c)** Thrust force definition for the DFS.

Figure 4.1: Force bookkeeping for the Ducted Fan System.

Table 4.2: Local inflow velocity and local inflow angle per component in the DFS at $V_\infty = 128$ m/s and $\alpha = 0$.

	V_{in}/V_∞		α_{loc}/α	
Power condition	**Power on**	**Power off**	**Power on**	**Power off**
Duct	128	128	4.5	4.5
Pylon	131	128	3.25	3.25
Propeller	146	146	4.5	4.5
Support	155	143	9.8	2.3
Control Vanes	138	130	4.6	2.3

Equation 4.1. The downwash angle (ϵ) is calculated in Equation 4.2 where the downwash at zero angle of attack (ϵ_0) is given by Equation 4.3. The rate of change in downwash angle can be determined by the derivative of Equation 4.3 given in Equation 4.4 [64].

$$\alpha_{in-duct} = \alpha_w - i_w - \epsilon + i_{duct} \tag{4.1}$$

$$\epsilon = \epsilon_0 + \frac{d\epsilon}{d\alpha} \cdot \alpha_w \tag{4.2}$$

$$\epsilon_0 = \frac{2 \cdot C_{L,w}}{\pi \cdot AR_w} \tag{4.3}$$

$$\frac{d\epsilon}{d\alpha} = \frac{2 \cdot C_{L_\alpha,w}}{\pi \cdot AR_w} \tag{4.4}$$

When the control vanes are deflected, the flow field around is also affected. This has not been taken into consideration in previous work yet but the effect has to be determined to be able to determine the influence on the design. To allow a numerical prediction of the correction in the inflow angle, the setup shown in Figure 4.2a in the Athena Vortex Lattice [65] (AVL) has been used. The lift coefficient of only the duct has been compared at different deflection angles with the original lift curve slope of the duct without elevator deflection. The lift coefficient values are shown in Figure 4.2b, where the blue line represents the lift curve slope with an un-deflected elevator. The colored markers give the values that are found at the given elevator deflection angles. A positive deflection of the elevator implies a trailing edge down deflection.

Extracting the angle of attack that corresponds to the intersection of the lift coefficient found and the slope of the duct lift curve leads to a linear relationship with the deflection angle, given in Equation 4.5. This shows a negative trend, which means that with a positive deflection of the elevator, the inflow angle of the duct becomes slightly negative. This can be explained by the channeling effect due to the dominant change in pressure distribution on the lower side of the top airfoil and on the upper side of the bottom airfoil. The final inflow angle for the duct is represented in Equation 4.6.

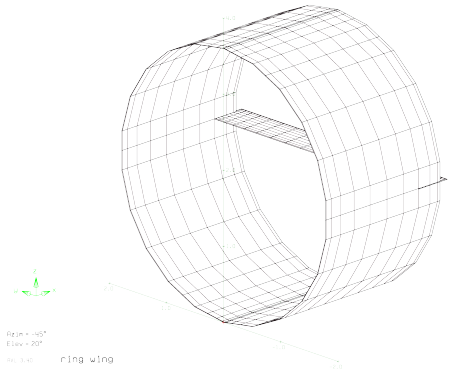

(a) AVL setup used to determine the effect of elevator deflection on the duct's inflow angle.

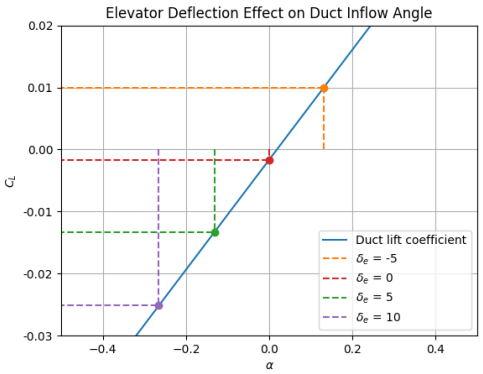

(b) Intersection points at different elevator deflection angles with the duct lift curve slope without deflection.

Figure 4.2: Elevator deflection effect on the duct inflow angle with control vanes places at x/c = 0.85, $AR_{duct} = 2.0$ and $c_{elevator} = 0.5$ m.

$$\alpha_{correction} = -0.0264 \cdot \delta_e - 0.0004 \tag{4.5}$$

$$\alpha_{in,duct} = \alpha_{duct} + \alpha_{correction} \tag{4.6}$$

The inflow velocity in both power on and off conditions can also be corrected for the downwash of the wing by using Equation 4.7. The result of Equation 4.4 is an input for this equation. In cruise condition this correction will be approximately 0.5 m/s.

$$V_{in,duct} = V_\infty \cdot \left(1 - \frac{(\frac{d\epsilon}{d\alpha})^2}{2}\right) \tag{4.7}$$

Propeller

The inflow parameters of the propeller are affected by the shape of the duct and the nacelle. In power-on and off conditions, the inflow velocity is dictated by the shape of the duct, hence the inflow velocity can be calculated by the continuity equation. Equation 4.8 shows the dependence on the diameter of the different sections, Figure 2.5 shows the respective diameters.

$$V_{in,prop} = V_{in,duct} \cdot \left(\frac{D_1}{D_2}\right)^2 \tag{4.8}$$

The inflow angle in both power-off and power-on condition is set to be equal to the DFS angle of attack. It is assumed that the chordwise position of the propeller plane inside the duct does not affect the inflow angle significantly when it remains in the first 40% of the duct chord. The propeller is then still in front or slightly after the thickest point of the duct airfoil.

Support strut

The inflow velocity of the support strut in power-off conditions can be calculated using the continuity equation. The inflow angle is determined to be zero because of the straightening effect of the duct surrounding the support.

In power-on conditions, the support is located in the swirl of the propeller. Where previously a propeller slip model has been used by Harinarain [13], the IAFM relies on the engineering approach of velocity vectors. This implies that the inflow velocity and angle can be determined by the axial and tangential velocity of the propeller. This is shown in Equation 4.9 and Equation 4.10, a graphic representation is shown in Figure 4.4. When the DFS is in power off condition, the duct does not fully guide the flow. Especially since the duct is not very long, the alignment of the flow with the duct is incomplete near the

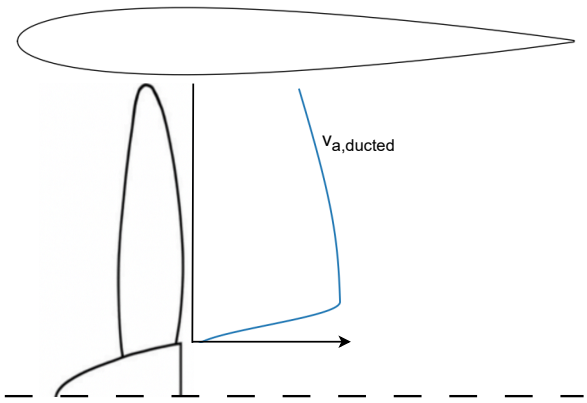

Figure 4.3: Radial axial velocity distribution behind a 6 bladed ducted propeller, lightly loaded propeller by means of a BEM analysis [66].

exit. An exact empirical prediction of the angle of attack alignment of the flow in power off conditions of a ducted fan is not available and hence it is assumed that the residual angle of attack inside the duct is half of the free stream condition.

The radial distribution of the axial velocity on a propeller blade is modified due to the presence of the duct on the tip of the blade. Figure 4.3 show an average value of V_{ax} that is taken to model the axial velocity distribution towards the tip. The support strut follows the same cant angle as the pylon, and thus the inflow angle needs to be corrected for the cant angle [67].

$$V_{in,support} = \begin{cases} V_{in-duct} \cdot \left(\frac{D_1}{D_3}\right)^2 & \text{power off} \\ \sqrt{V_{tan}^2 + \left(V_{in,duct} \cdot \left(\frac{D_1}{D_3}\right)^2 + 2 \cdot V_{ax}\right)^2} & \text{power on} \end{cases} \tag{4.9}$$

$$\alpha_{in,support} = \begin{cases} 0.5 \cdot \alpha_{duct} & \text{power off} \\ \arctan\left(\frac{V_{tan}}{V_{in,duct} \cdot \left(\frac{D_1}{D_3}\right)^2 + 2 \cdot V_{ax}}\right) \cdot cos(\phi) & \text{power on} \end{cases} \tag{4.10}$$

Nacelle

The nacelle, which is for the majority located after the propeller plane has a complicated flow field. Where between the propeller plane and support strut, the flow is swirling around the nacelle. After the support strut some rotation is taken from the flow. The exact amount of rotation that is taken from the flow is not determined numerically 20%. Research of Li et. al [68] showed a swirl retrieval of 42% in an open rotor case. The configuration test had six SRVs compared to the singular wing (support) in the DFS. The support does however have a larger surface area and hence it is assumed that a bit more than a third of the 42% could be recovered in the case of the DFS. This comes to a value of 16%. It must be noted that this value has not been validated.

A schematic representation of this is shown in Figure 4.4. The inflow velocity is determined to be the average of the velocity before and after the support strut, Equation 4.11. The inflow angle is set to be half of the support strut inflow angle. The inflow angle is required to determine the lift and drag coefficient of the nacelle.

$$V_{in-nacelle} = \frac{V_{ax,support} + V_{ax,control}}{2} \tag{4.11}$$

$$\alpha_{in,nacelle} = \frac{\alpha_{in,support} \cdot 1.84}{2} \tag{4.12}$$

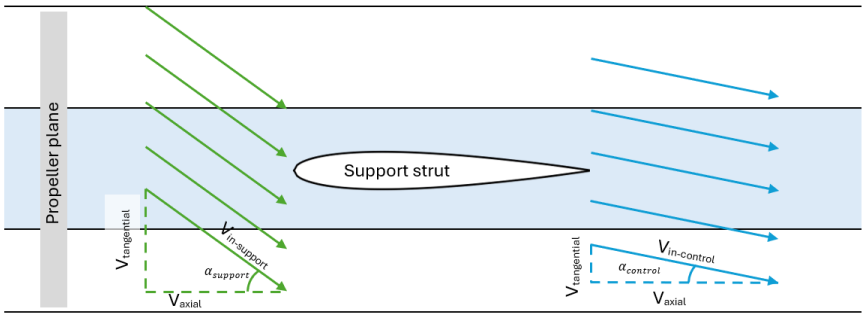

Figure 4.4: Schematic representation of nacelle flow stream, nacelle indicated in light blue.

Control Vanes

The inflow velocity of the control vanes is depending on the effective inflow velocity of the support strut. When the power is off the velocity can be determined using the continuity equation. The inflow velocity is given in Equation 4.13. When the power is on, it is assumed that the inflow velocity of the control vanes is

$$V_{in,control} = \begin{cases} V_{in,duct} \cdot \left(\frac{D_1}{D_5}\right)^2 & \text{power off} \\ V_{effective} = V_{in,support} \cdot \left(\frac{D_3}{D_5}\right)^2 & \text{power on} \end{cases} \tag{4.13}$$

It is assumed that the support strut takes 16% the rotation from the flow, and hence the inflow angle for the control vanes is 84% of the inflow angle of the control vanes. If the control vanes are deflected, the deflection angle is added, Equation 4.14.

$$\alpha_{in,control} = \alpha_{in,support} \cdot 0.84 + \delta_{r,e} \tag{4.14}$$

Pylon

As the pylon is outside the duct, it is assumed that the inflow parameters are not influenced by the power-on or off situations inside the duct. The inflow conditions for the pylon are similar to those of the duct described above. However, the inflow angle is corrected for the cant angle of the pylon. An additional correction is applied because of the interference of the duct and fuselage on the flow on the pylon. The value for this correction is between 1 and 2 ° according to Jacobs [69]. The inflow angle is defined as Equation 4.15 [67].

$$\alpha_{in,pylon} = \alpha_{in,duct} \cdot cos(\phi) - \alpha_{correction} \tag{4.15}$$

4.3. Zero Lift Drag

The zero lift drag of the components inside the DFS can be determined using Equation 4.16 set up by Sadraey [70]. Where the skin friction coefficient ($C_{f,i}$) is determined by Equation 4.17, where the Reynolds number of each component is determined based on their characteristic length and local velocity.

$$C_{D0,i} = C_{f,i} \cdot ff_i \cdot f_M \cdot \left(\frac{S_{wet}}{S_{ref}}\right) \tag{4.16}$$

$$C_{f,i} = \frac{0.455}{[log_{10}(Re_i)]^{2.58}} \tag{4.17}$$

A Mach correction factor is applied by f_M to correct for compressibility effects, calculated in Equation 4.18 is applied according to Sadraey [70]. The form factor (ff_i) is different for the type of components and will be explained in subsection 4.3.2. The reference area for all components will be the

wing area in order to ensure a fair comparison between the different aircraft types. The wet area of the components is determined by subsection 4.3.1.

$$f_M = 1 - 0.08 \cdot M^{1.45} \tag{4.18}$$

4.3.1. Wetted Area

The wetted area of a wing can be calculated using Equation 4.19, according to Torenbeek [50]. Where λ is the taper ratio, S is the exposed surface area of the wing and τ is the thickness to chord ratio of the tip divided by root (Equation 4.20). This equation can also be applied to the horizontal and vertical stabilizer. For the DFS, this relation is used for the pylon, support strut and control vanes.

$$S_{wet,wing} = 2 \cdot S_{wing} \cdot \left(1 + 0.25 \cdot (t/c)_{root} \cdot \frac{1 + \tau \cdot \lambda}{1 + \lambda}\right) \tag{4.19}$$

$$\tau = \frac{(t/c)_{tip}}{(t/c)_{root}} \tag{4.20}$$

Equation 4.19 is modified to account for the circular shape of the duct for the DFS. For an untapered duct, the wetted area is given by Equation 4.21.

$$S_{wet,duct} = 2 \cdot \pi \cdot d_{duct} \cdot c_{duct} \cdot (1 + 0.25 \cdot (t/c)_{max}) \tag{4.21}$$

Where it was unclear how the wet area for the nacelle has been determined in previous studies, the wet area (Equation 4.22) is calculated with geometric relations using the exposed area of a conical-ended cylinder. Here, S_{wet1} represents the wetted area of the cylinder part and S_{wet2} the conical end.

$$\begin{aligned} S_{wet,nacelle} &= S_{wet1} + S_{wet2} \\ S_{wet1} &= \pi \cdot d_{nacelle} \cdot l_{nacelle} \\ S_{wet2} &= \frac{1}{2} \cdot \pi \cdot d_{nacelle}^2 \end{aligned} \tag{4.22}$$

4.3.2. Form Factor

For an unswept wing, the form factor depends on the maximum thickness-to-cord ratio, Equation 4.23. As the duct in the DFS can be treated as a folded wing, this equation is assumed to be applicable. The same equation is applied to determine the form factor of the pylon and support.

$$ff_{duct} = 1 + 2.7 \cdot (t/c)_{max} + 100 \cdot (t/c)_{max}^4 \tag{4.23}$$

The shape of the nacelle is comparable to that of a fuselage, and hence the form factor equation for the fuselage, established by Sadraey [70], is applied in Equation 4.24 and depends on the ratio between the length and the diameter, also known as the slenderness ratio.

$$ff_{nacelle} = 1 + \frac{60}{(l/d)^3} + 0.0025 \cdot \frac{l}{d} \tag{4.24}$$

If the wing surface is swept, such as the wing itself or the vertical tail surface, Equation 4.25 can be applied. The distance between the leading edge and the maximum thickness point is given by x_t and φ_m is the sweep angle [71].

$$ff_{swept} = \left(1 + \frac{0.6}{x_t} \cdot (t/c)_{max} + 100(t/c)_{max}^4\right) \cdot \left(1.34 \cdot M^{0.18} \cdot cos(\varphi_m)^{0.28}\right) \tag{4.25}$$

4.4. Lift Induced Drag

The prediction of the lift-induced drag of the wing profile's and duct are defined in Equation 4.26, based on the method described by Raymer [51].

$$C_{Di} = \frac{C_L^2}{\pi \cdot AR \cdot e} \tag{4.26}$$

The oswald factor (e) in Equation 4.26 is calculated in Equation 4.27, where $\Lambda_{c/4}$ represents the sweep angle at the quarter chord of the wing. For the duct, the oswald factor is equal to 2 as stated by Traub [52].

$$e = \frac{1.78 \cdot (1 - 0.045 \cdot AR^{0.68})}{cos^{0.15}(\Lambda_{c/4})} \tag{4.27}$$

4.5. Lift Coefficient

The lift coefficient for the DFS is built up from three different numerical relations. The duct, wing profiles and nacelle each have a different way of determining the lift coefficient. The total lift coefficient for the PE is the sum of the normalized component lift coefficient.

Duct

To predict the duct's lift coefficient, the Weissinger's [72] lift prediction model has been used, which has proven to be accurate for high and low aspect ratio ring wings. The lift curve slope of the duct is given by Equation 4.28, where ζ is defined in Equation 4.29. The lift curve slope required for Equation 4.28, is the lift curve slope obtained for the 2D airfoil profile.

$$C_{l_{\alpha,duct}} = \frac{\pi}{2} \cdot \zeta_{duct} \cdot C_{l_\alpha} \tag{4.28}$$

$$\zeta_{duct} = \frac{1}{1 + \frac{\pi/2}{AR} + \frac{tan^{-1}\left(1.2 \cdot \frac{1}{AR}\right)}{AR}} \tag{4.29}$$

A differentiation needs to be made between when the propeller is on and off when determining the lift coefficient of the duct, Equation 4.30. In the power-on situation, lift curve slope is multiplied by a factor that has been determined by Harinarain [13].

$$C_{l,duct} = \begin{cases} C_{l_\alpha} \cdot \alpha & \text{power off} \\ C_{l_\alpha} \cdot (1 + 0.2 \cdot \sqrt{T_{c,prop}}) & \text{power on} \end{cases} \tag{4.30}$$

Wing profiles

The lift coefficient of the wing profiles is defined by the lift gradient multiplied by the inflow angle of attack. The C_{l_α} can be approximated for symmetric airfoils based on the thickness, Equation 4.31 set up by Hoerner [73]. In general, the slope of the lift curve C_{l_α} can be approximated by Equation 4.32 for symmetric airfoil, with α in radians. This limits the approximation to the linear part of the lift curve slope and does not include stall.

$$C_{l_\alpha} = 0.11 + 0.09 \cdot \frac{t}{c} \tag{4.31}$$

$$C_{l_\alpha} = 2\pi \tag{4.32}$$

The lift coefficient model for the control vanes from the previous work has to be elaborated, as they are placed in the swirl of the propeller. When a front view of the elevators inside the DFS is shown, Figure 4.5a is illustrated. The propeller swirl causes the inflow angle of one of the elevators to be negative, while the other is positive, as shown in Figure 4.5b. The inflow angle is calculated as in section 4.2 but switches sign depending on which control vane is analyzed. When the control vanes are undeflected, there is no difference in lift generated as the forces cancel out. However, when the control vanes have a positive deflection, for example, the lift on control vane 1 will have a positive lift while the control vane 2 will have a negative lift. With a greater deflection, the lift on control vane 2 will eventually become positive but the generated load will be lower than control vane 1.

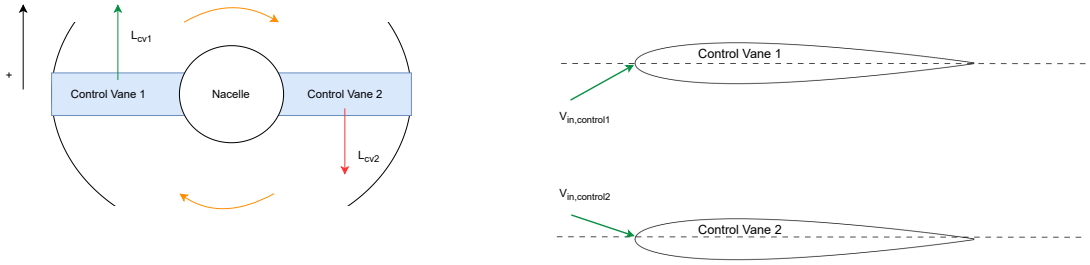

(a) Influence of the propeller swirl onto the lift generation of the elevators inside a DFS.

(b) Positive and negative inflow angle illustrated for the control vanes.

Figure 4.5: Schematic front view of the elevators inside a DFS in the propeller swirl including lift direction.

Nacelle

In other studies, it was assumed that the nacelle does not produce any lift, Allen [74]claims that a inclined body of revolution produces a certain amount of lift. Thus, the lift coefficient of the nacelle is based on his prediction method for flow over a slender inclined body of revolution. The prediction of the lift coefficient for the nacelle is given in Equation 4.33. The base area S_b is the projected area of the nacelle where the planform area A_p represents the profile area as seen from the side. The drag coefficient at $\alpha = 90$ can be approximated by the drag of an infinite cylinder [75].

$$C_{l,nacelle} = \frac{S_b}{A} \cdot sin(2 \cdot \alpha) \cdot cos\left(\frac{\alpha}{2}\right) + C_{d,\alpha=90} \cdot \frac{A_p}{A} \cdot sin^2(\alpha) \cdot cos(\alpha) \tag{4.33}$$

4.6. Pitching Moment Coefficient

Before the pitching moment coefficient of the PE is setup, it needs to be defined on component level first in subsection 4.6.1 after which they are combined in a combined subsection 4.6.2.

4.6.1. Component Based

Similar to section 4.5, the pitching moment coefficient is also built up from three different numerical relations. The duct, wing profiles and nacelle each have a different approach in determining the pitching moment coefficient.

Duct

The pitching moment prediction model, set up by Maqsood [44], is used to predict the pitching moment coefficient of the duct. This prediction model has shown good agreement with the experimental results as explained in section 3.3. Equation 4.34 shows the relation used for the prediction model. The parameters x_p and x_e are found in Equation 3.16 and Equation 3.17 respectively and hold for aspect ratios of the duct below 3.

$$C_{m,duct} = x_p \cdot K_p \cdot sin(\alpha) \cdot cos(\alpha) + x_e \cdot K_v \cdot sin^2(\alpha) \tag{4.34}$$

Wing profiles

The category of wing profiles holds the pylon, support and control vanes. The pitching moment coefficient for these profiles is calculated with the reference point at a quarter chord and by means of the panel method in XFoil. The pressure distribution is integrated to calculate the pitching moment coefficient, Equation 4.35 according to Drela [76].

$$C_{m,airfoil} = \frac{1}{c} \cdot \int_{surface} (x - x_{ref}) \cdot p(x) \cdot dA \tag{4.35}$$

Nacelle

A new prediction method for the lift coefficient for the nacelle has been implemented and for consistency the same modeling technique is applied for the pitching moment coefficient. By modeling the flow over a slender inclined body of revolution, as modeled by Allen [74], the pitching moment coefficient can be found by Equation 4.36. Here, Q presents the volume of the body and x_m is the center of the moment. The other parameters are similar to the lift and drag coefficient definition of the nacelle.

$$C_{m,nacelle} = \left[\frac{Q - S_b \cdot (l_{nacelle} - x_m)}{A \cdot c_{ref}}\right] \cdot sin(2\alpha) \cdot cos\left(\frac{\alpha}{2}\right) + C_{d_{\alpha=90}} \frac{A_p}{A} \cdot \left(\frac{x_m - x_{\alpha=90}}{c_{ref}}\right) \cdot sin^2(\alpha) \quad (4.36)$$

4.6.2. Propulsive Empennage

The pitching moment of the complete PE is defined at the quarter chord point of the duct on the center line of the propeller plane. The pitching moment coefficient is found by superposition of individual scaled components. Figure 4.6 illustrates the forces, moments and reference lengths that contribute to the pitching moment. This approach does not take into account the detailed interaction and interference between the components beyond the calculation of interference drag and lift between the component joints. The affect of the propeller on the components has been taken into account when determining the inflow properties.

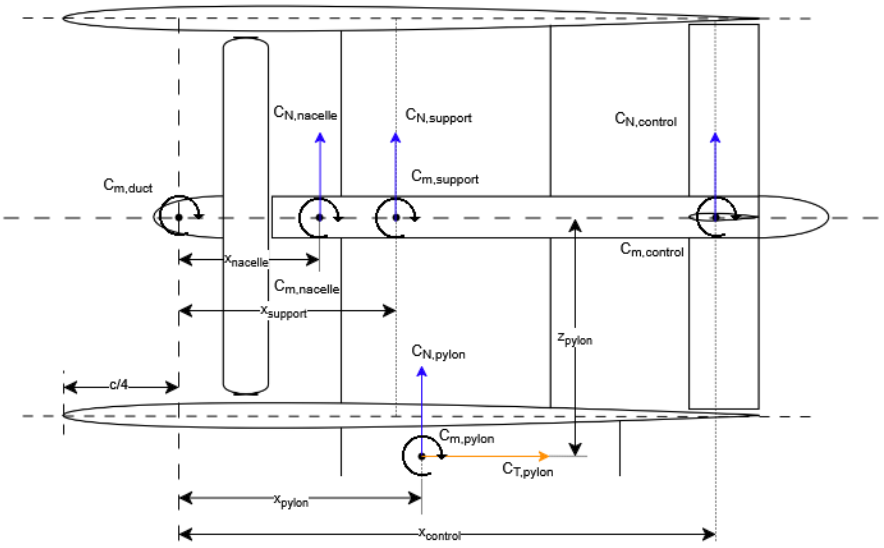

Figure 4.6: Definition of forces, moments and reference lengths for determining the pitching moment coefficient for the PE.

Equation 4.37 defines the pitching moment coefficient of the PE, where the moment contribution is given in Equation 4.38 and the force contribution is defined by Equation 4.39. The only tangential force contribution that is taken into consideration is the one of the pylon, as that component's force is the only one that is not acting through the center line of the PE. The properties are added to each other by means of the normalization explained in section 4.8.

$$\circlearrowleft + \sum C_{m,PE} = \sum C_{m,i} + \sum F_i \cdot x_i \quad (4.37)$$

$$\circlearrowleft + \sum C_{m,i} = C_{m,duct} + C_{m,support} + C_{m,pylon} + C_{m,nacelle} + C_{m,control} \quad (4.38)$$

$$\sum F_i \cdot x_i = C_{N,support} \cdot x_{support} + C_{N,pylon} \cdot x_{pylon} + C_{N,nacelle} \cdot x_{nacelle} + C_{N,control} \cdot x_{control} - C_{T,pylon} \cdot z_{pylon} \quad (4.39)$$

The normal force contribution of the propeller is taken into account separately when calculating the thrust-induced moment. To ensure that it is not used twice, it has been left out of the pitching moment coefficient of the PE.

4.7. Thrust

The studies of van den Dungen [16], Harinarain [13], Adib [22] and Stavreva [15] on the DUUC have relied on the Ducted Fan Design Code [77] (DFDC) for the calculation of the thrust for the PE. This software is limited to axisymmetric flow, and hence the angle of attack can not be modeled. Additionally, the tool is not flexible enough to model quick changes in the geometry. Thus, empirical relations are used to setup a new thrust model for the PE. The thrust for each DFS consists of three components: the thrust generated by the propeller, the thrust generated by the duct under influence of the propeller and additional thrust generated by the propeller under influence of the duct. To get to the total thrust of the PE, the thrust of the DFS are multiplied by two as it is assumed that both DFS operate in the same conditions.

The thrust generated by the propeller is calculated with a Blade Element Momentum (BEM) that based on the propeller profile used and operating conditions determines the thrust and normal force of the propeller. The propeller blade is split into small segments as illustrated in Figure 4.7, and the total force is the sum of all these elements. This method is also used to calculate the thrust generated for the reference aircraft for comparison.

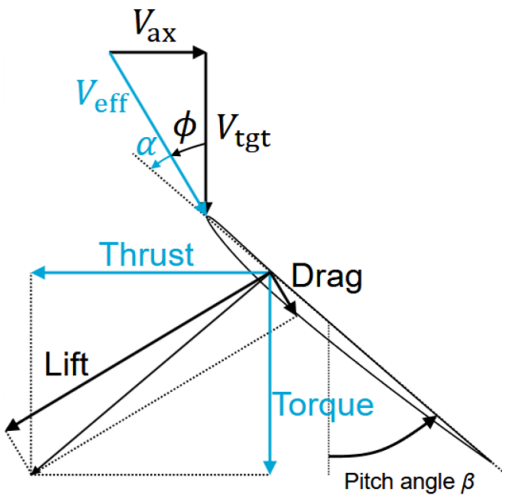

Figure 4.7: Velocity composition and force definition on a blade segment in the BEM model [78].

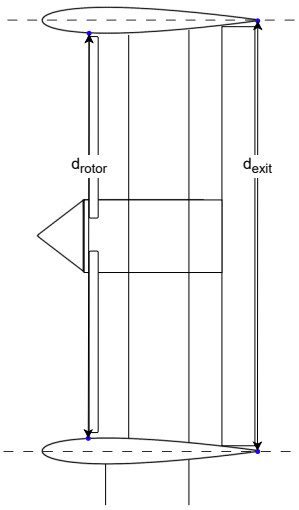

Figure 4.8: Diameter definition at the rotor and exit-plane of a DFS.

Ducted fans generate additional thrust at low inflow velocities. This small thrust rapidly changes to a drag component when the duct inflow velocity increases. Since the main focus of the DUUC analysis is on cruise conditions, the thrust generation of the duct under the influence of the propeller will not be treated in the aerodynamic model.

Because of the shape of the duct around the propeller, the slipstream of the propeller is not contracted as much as it usually does when there is no duct present. This will lead to some additional thrust. Pereira [19] has shown that with using the conservation of mass, momentum and energy an equation can be set up that shows the relationship between four fundamental characteristics of open en ducted rotors. The relationship between thrust, power requirement, rotor disk area and the expansion ratio is given in Equation 4.40. Here, the subscripts $_{SR}$ represent the Shrouded Rotor and $_{OR}$ represent the Open Rotor case. The effective expansion ratio is represented by σ_{duct} and given by Equation 4.41. The definition of of the diameter of the exit and rotor-plane are illustrated in Figure 4.8

$$\frac{P_{in_{SR}}}{P_{in_{OR}}} = \frac{1}{\sqrt{2\sigma_{duct}}} \left(\frac{T_{SR}}{T_{OR}}\right)^{3/2} \left(\frac{A_{OR}}{A_{SR}}\right)^{1/2} \tag{4.40}$$

$$\sigma_{duct} = \frac{A_{exit}}{A_{rotor}} = \left(\frac{d_{exit}}{d_{rotor}}\right)^2 \tag{4.41}$$

When diameter of the rotor in the open and shrouded case have the same dimension ($A_{SR} = A_{OR}$) and both cases consume the same amount of power ($P_{SR} = P_{OR}$). The relation of thrust between the two cases is expressed as Equation 4.42, which shows that the thrust is only depending on the expansion ratio.

$$\frac{T_{SR}}{T_{OR}} = (2 \cdot \sigma_{duct})^{1/3} \tag{4.42}$$

4.8. Normalization

In order to be able to compare all coefficients with each other, an area weighted ratio is used to normalize the the coefficients. Because different components have different inflow velocities, a velocity ratio is also applied in the normalization. Equation 4.43 shows an example of how the lift coefficient of the support strut is normalized. The reference area that will be used is the reference area of the wings of the ATR72-600. The free stream velocity depends on the operating condition at that point.

$$C_{L_i} = C_{l_i} \cdot \left(\frac{S_i}{S_w}\right) \cdot \left(\frac{V_i}{V_\infty}\right)^2 \tag{4.43}$$

After all coefficients of the different components are added, they can be de-normalized by multiplying by the wing reference area and free stream velocity. When multiplying by half the air density, the total force can be found.

4.9. Propulsive Efficiency

The propulsive efficiency can be defined in several ways. For the evaluation of the propulsive efficiency of the aircraft the definition as in Equation 4.44 will be used. Where the force in x-direction F_x is based on the reference frame provided in subsection 4.9.1. The force in x-direction for the DUUC and ATR are given in Equation 4.45 and Equation 4.46, respectively.

$$\eta_{propulsive} = \frac{F_x \cdot V_\infty}{P_{in}} \tag{4.44}$$

The power input, P_{in} is extracted from the performance data of the PW127 engine used in the ATR and DUUC aircraft.

4.9.1. Reference Frame

The PE is a system synergizing the propulsor and stabilizer. When the propulsive efficiency would be compared to a traditional turboprop configuration or only the tail, it would be impossible to make a justifiable comparison. Hence, the decision has been made to compare the propulsive efficiency of the PE with that of the propulsion and tail group of the reference aircraft. The blue highlighted groups are considered for propulsive efficiency in Figure 4.9. It must be noted that the slipstream effects of the open rotor propeller onto the wing are not taken into consideration for the ATR aircraft.

The sum of forces for the DUUC is given in Equation 4.45. The definitions of these forces are given in chapter 4. For the ATR72-600 a similar relation is given in Equation 4.46. Note that the forces in the definitions below are the sum of both DFS and for the ATR of both engines.

$$\overset{+}{\leftarrow} \sum F_{x_{DUUC}} : T_{prop} + T_{duct} - D_{PE} \tag{4.45}$$

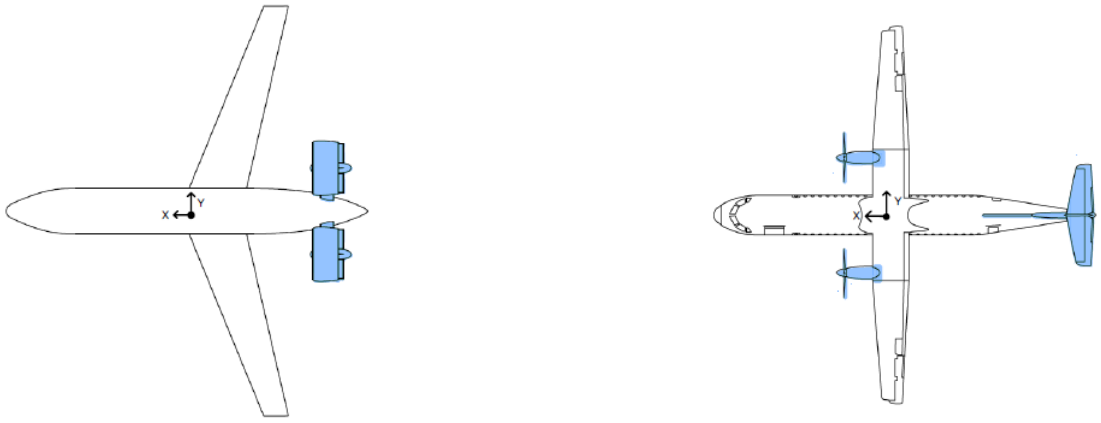

(a) Reference frame DUUC.

(b) Reference frame ATR72-600.

Figure 4.9: Different references frames for propulsive efficiency.

$$\overset{+}{\longleftarrow} \sum F_{x_{ATR72}} : T_{prop} - D_{nacelle} - D_{empennage} \tag{4.46}$$

4.9.2. Performance Improvements

The DFS has two performance improvement factors inside the duct that will improve propulsive efficiency compared to the open rotor engine. Due to the presence of the duct around the propeller tip, the swirl losses are reduced, and thus the performance increases. A numerical prediction is made to model the increase in efficiency based on experimental data, related to the gap-to-span ratio (GSR) which has been discussed in Figure 3.3. The slope at an advance ratio of 0.6 has been used to increase the efficiency based on the GSR. The GSR [%] is defined in Equation 4.47, where the efficiency improvement slope is defined in Equation 4.48 according to Yongle [34].

$$GSR = \frac{l_{gap}}{R_{prop}} \tag{4.47}$$

$$a_\eta = -0.02884 \tag{4.48}$$

Secondly, the support and control vanes have a secondary function as a swirl recovery vane. It is difficult to determine the exact amount of swirl recovery that each component delivers, but based on the inflow angle of the component, a certain amount of swirl recovery can be estimated. As the support and control surfaces do not fill the whole cross-sectional area, a certain factor needs to be applied to how much of the swirl continues in the duct. An estimate is made that about half of the swirl intensity continues after the support and again half of the swirl passes the control vanes.

The propulsive efficiency of the ATR is affected by the interaction between the propeller and the wing. This interaction has not been included as there is no available empirical method to predict this efficiency increase. This raises the critical point that the interaction effects are considered inside the PE but not in the ATR. However, it is expected that this level of detail will not be required in the analysis.

4.10. Model Validation

The lift, drag and pitching moment coefficient for the components inside the DFS, calculated by the IAFM, are validated with experimental data. The coefficients for the assembled DFS are compared in power-on and power-off conditions. The thrust generation is compared with a reference case in the DFDC.

4.10.1. Lift Coefficient

The lift curve slope of the duct is depicted in Figure 4.10a. The IAFM results is compared with experimental data from a duct with an AR of 1.5, similar to the ring wing that is modeled in AVL. These experimental sources are also compared to the leading edge suction analogy that is explained in section 3.3. The explanation of the reference areas and normalization that are used in the experimental data and in the AVL analysis is given in Appendix C.

When analyzing Figure 4.10a, the maximum deviation between the IAFM and the experimental data is +8%, whilst the maximum deviation with the leading edge suction analogy is -6%. As the IAFM predicts a value between the theoretical model and the experimental data with a margin of <10%, it is set that the IAFM provides a value that is accurate enough for this study. This prediction only approximates the linear part of the lift curve slope and does not treat stall. As mentioned in section 3.3 the stall angle of ducts with aspect ratios below 3 have a stall angle above 17 degrees angle of attack. As it is assumed that the critical angle of attack for the wing is around 16 degrees. Hence, the wing would stall before the duct, and thus stall is not included in the IAFM for stall.

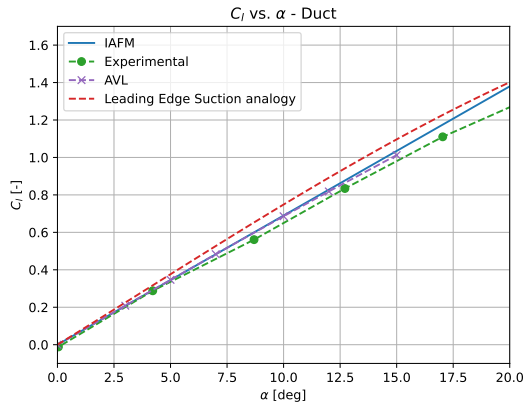

(a) C_{L_α} comparison curve for a duct with Aspect Ratio 1.5 and airfoil profile NACA0016 without the presence of other DFS components except the duct.

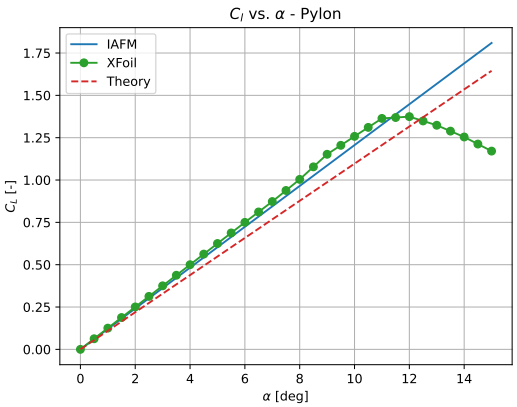

(b) C_{L_α} comparison curve for the NACA0012 airfoil between XFoil data and IAFM.

Figure 4.10: Lift coefficient validation for the duct and pylon of the DUUC.

The lift coefficient for the pylon has been compared with the theoretical lift coefficient of Equation 4.32 and the XFoil lift coefficient for NACA0012 specifically. The IAFM in Figure 4.10b predicts the lift coefficient for NACA0012 linearly until an angle of attack of 20 degrees. Since the lift coefficient prediction closely matches the XFoil results, the decision has been made to use the XFoil approximation to include the stall prediction as well. The small deviation between the theoretical prediction and the XFoil results can be explained by viscous effects and wake geometry interaction.

The lift coefficient of the nacelle was assumed to be zero in earlier aerodynamic models of the PE. The new model that determines the lift based on an inclined body of revolution compared to experimental data of Allen [74] is shown in Figure 4.11. It can be observed that the values obtained from the IAFM are in agreement with the experimental data and form a linear regression of the experimental data. The reference area is the base area of the nacelle, the lift contribution is small but not zero and has to be taken into consideration into the analysis of the DUUC.

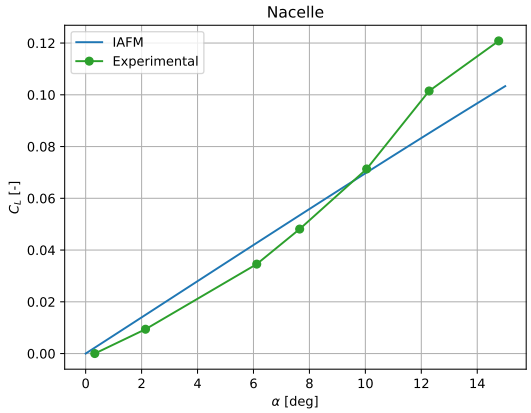

Figure 4.11: C_L versus α nacelle validation with experimental data from Allen [74].

When all components are combined into a DFS, the lift coefficient can be validated under power-on and power-off conditions. Note that in the experimental data, the exact layout has not yet been replicated for experiments. The IAFM is thus modified to represent the geometry of the experimental setup as best as possible. The validation in the power-off condition is given in Figure 4.12a and the power-on condition is shown in Figure 4.12b.

In power-off condition, the prediction model has a similar slope compared to the experimental data found by Harinarain [13] as can be observed in Figure 4.12a. The IAFM has a small over-prediction of the lift coefficient. This can be attributed to the lift curve slope of the duct being steeper than the experimental data as shown in Figure 4.10a. Additionally, it has been tried to model the pylon and support similar to the experiment but some of the dimensions had to be determined analytically. This could have offset the lift coefficient.

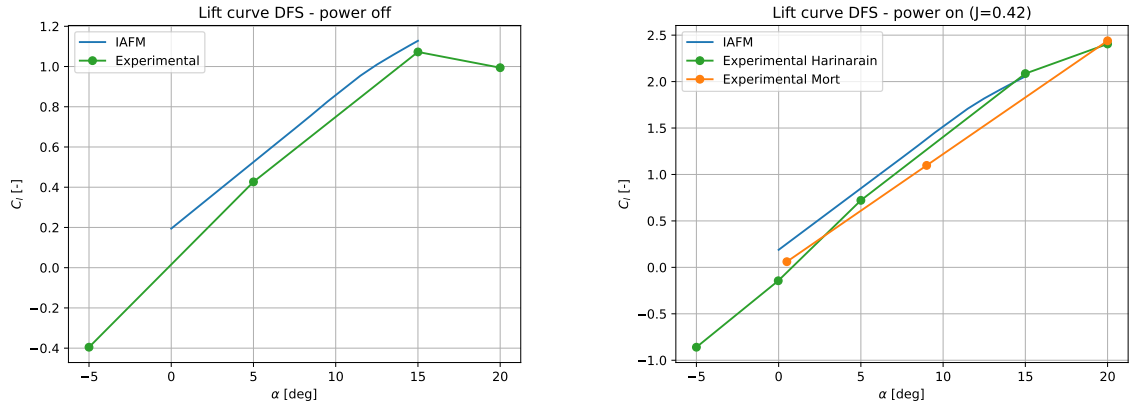

(a) C_{L_α} validation for DFS in power-off condition.

(b) C_{L_α} validation for DFS in power-on condition.

Figure 4.12: Lift coefficient validation of a ducted fan system in different power conditions.

For the power-on conditions, a similar phenomena has occurred where the slope is similar but there is a small offset, especially at the lower angles of attack. The delta between the IAFM and experimental data of Harinarain [13] decreases towards $\alpha = 15$. The experimental data of Mort [79] has an offset but also follows the same slope. The offset can be linked to the additional components that are present in the DFS but not in the experiment of Fletcher. Think about the support and pylon.

4.10.2. Drag Coefficient

As the drag coefficient is built up in two components, the validation is done separately for each component. First, the component zero lift drag is discussed after which the complete drag polar is compared

with experimental data.

Zero Lift Drag

The zero lift drag that the aerodynamic section of the IAFM produces has to be validated using existing and available data. The reference data for the horizontal and vertical tail of the ATR72-600 aircraft are obtained from the Aircraft Design Studies based on the ATR 72 modeled by Nita [62], and are evaluated in similar flight conditions and with the same reference area. As can be observed from Figure 4.13 the values from the reference and IAFM are in good agreement. For the Propulsive Empennage, specifically the duct and pylon, reference data is available from the study of van den Dungen [16] and Stavreva [15]. The zero lift drag for the pylon matches the previous research, whilst for the duct the prediction model is slightly higher. This has to do with the different definition of the form factor. For the support and control vanes, there is no reference data available, but since the methodology and component build-up are similar to that of the pylon (for which the reference is in good agreement), it is assumed that the approach is valid.

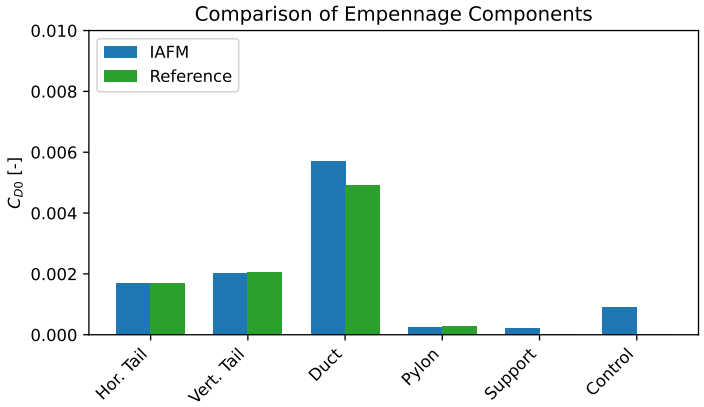

Figure 4.13: Zero lift drag components for DUUC V0.1 at $V_\infty = 128$ m/s and ATR72-600 data from reference data compared with IAFM, with a reference surface of the main wing.

Lift Induced Drag

The drag curve for the duct over a range of angle of attack is given in Figure 4.14. It is plotted together with experimental data obtained by Fletcher [24] and the numerical prediction based on the leading edge suction analogy by Maqsood [44]. As can be observed, the IAFM has a slight mismatch with the numerical prediction of Maqsood above 12 degrees in angle of attack, but does follow the experimental data more closely.

The earlier nacelle models assumed that the nacelle did not produce any lift. This also implies that the lift induced drag is zero for the nacelle and only the zero lift contribution made up the drag coefficient of the nacelle. The lift induced drag is compared to the experimental data of Allen [74] in Figure 4.15.

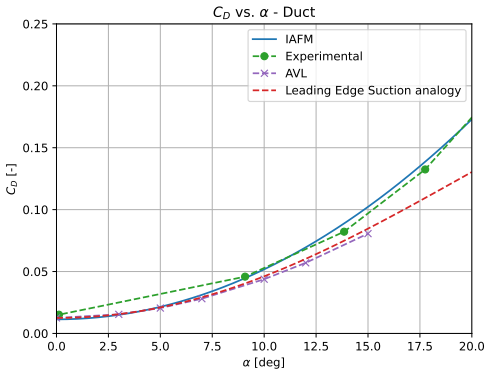

Figure 4.14: C_D versus α validation for the duct compared with experimental data from Fletcher [24] and the leading edge suction analogy prediction line setup by Maqsood [44]. An additional validation is added with an AVL model.

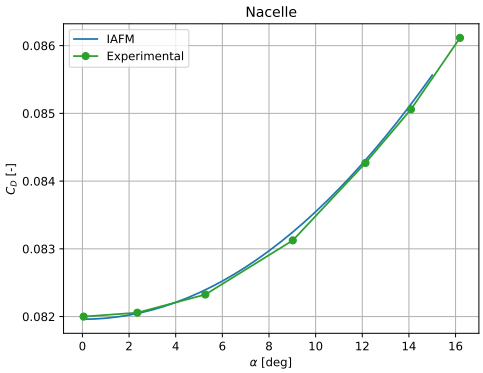

Figure 4.15: C_D versus α validation for the nacelle based on the experimental data of Allen [74].

When the drag polar of the duct combined with the experimental data and numerical prediction, Figure 4.16 is obtained. The IAFM predicts a performance between the numerical prediction of Maqsood [44] and the experimental values of Fletcher [24]. Here, the prediction is closer to the experimental data than to the numerical prediction. This can be attributed to the fact that the numerical prediction of Maqsood does not take non-linearity in the lift prediction into account.

A similar thing is done with the complete Ducted Fan System, where all the components are combined. This data is compared with the experimental data from Mort [79] in which a 7 foot ducted propeller has been investigated. Furthermore, the DFS has been recreated in AVL (shown in Figure C.1) and the results are given in Figure 4.17. The deviation from the experimental data can be explained by the fact that it does not have the same components as the tested model, such as the support rod.

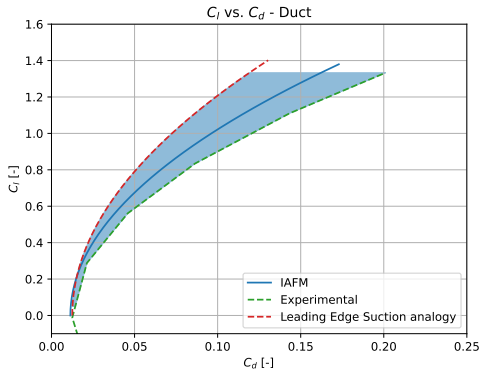

Figure 4.16: Drag polar validation of the duct in power-off condition with the experimental data from Fletcher.

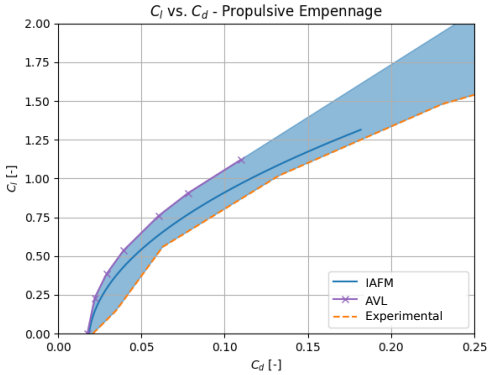

Figure 4.17: Drag polar validation of the DFS in power-off condition with experimental data from Mort [79] and AVL.

The drag coefficient under power-on conditions is compared with the experimental data of Mort [79] in Figure 4.18. The IAFM has a larger lift coefficient for a given drag coefficient value compared to the experimental data. Once again, this can be attributed to the additional components in the DFS that are not in the model tested by Mort.

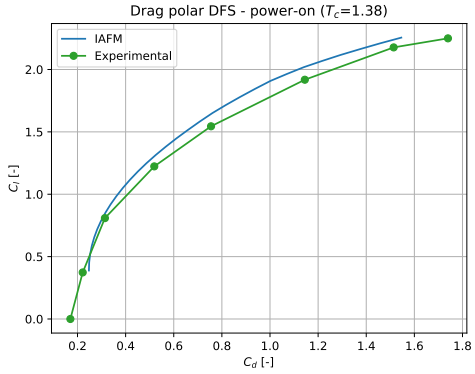

Figure 4.18: Drag polar validation of the DFS at power-on conditions with a thrust coefficient of 1.38.

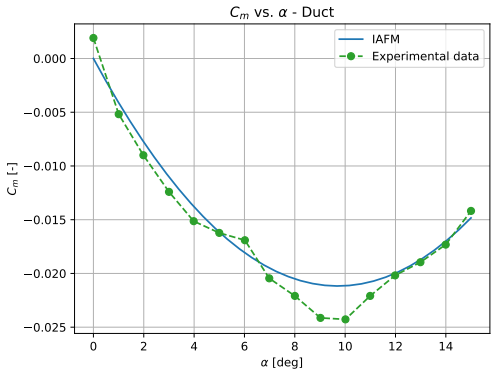

Figure 4.19: Pitching moment coefficient over alpha for the duct. Validated with experimental data from Traub [53].

4.10.3. Pitching Moment Coefficient

The pitching moment coefficient of the duct, compared to the experimental data from Traub [52] is shown in Figure 4.19. For most of the curve, the IAFM forms a regression of the experimental data points. However, between 8 and 12 degrees in angle of attack, the pitching moment coefficient does not become as negative as the experiment showed. Since this is an under-prediction of the pitching moment coefficient, it has been determined to use the IAFM for a conservative analysis.

The pitching moment coefficient for the DFS assembly is compared with the experimental data found by Mort [79]. The pitching moment coefficient of the IAFM for the DFS has a larger value than the values in the experimental data. This merely has to do with the fact that our DFS has different component and mounting structures. As the individual components have been validated, it is taken that the combined pitching moment coefficient produces results that are in the right ballpark.

4.10.4. Thrust

The thrust prediction in the IAFM is validated with a test case in the DFDC. The DFDC results have been validated with the results found by Mort [79]. The comparison between the IAFM and the DFDC results is found in Table 4.3. The propeller thrust is overestimated by the BEM model, this has likely to do with the fact that not all the losses are properly incorporated and taking the average axial velocity over the blade overestimates the tip loss reduction. The thrust of the duct is underestimated by the IAFM. The DFDC calculates the thrust of the duct based on the pressure distribution over the duct while the IAFM determines the thrust based on the expansion ratio related to the conservation laws.

When the total thrust of both models are compared, the DFDC finds a thrust 14 N higher than the prediction model. This is a 1.1% deviation of the total thrust and therefore accurate enough for the conceptual design of the DUUC.

Table 4.3: Thrust comparison between IAFM and DFDC at V = 20 m/s with a blade radius of R = 1.07 m at 1200 rpm.

Model	T_{prop} **[N]**	**Deviation [%]**	T_{duct} **[N]**	**Deviation [%]**
DFDC	992	-	336	-
IAFM	1003	+ 1.1%	311	-7.5%

5

Flight Mechanics

In the flight mechanics section of the IAFM, the mass of all components are estimated after which the Center of Gravity is determined. Combined with the aerodynamic section of the IAFM, the so-called vertical and horizontal stabilizer for the DUUC can be sized according to the stability and control requirements. The control and stability derivatives are set up and modified specifically for the DUUC. It must be mentioned that in this study only the longitudinal and directional static stability are investigated and that the lateral stability is not included. Lastly, the IAFM is validated with reference data and previous studies.

5.1. Mass Estimation

The mass of the Propulsive Empennage components must be determined to calculate the center of gravity. For comparison, the weight estimations for the reference aircraft are done in Appendix B. The methodology for the weight estimation of the wing and fuselage are also presented in the appendix where it is assumed that the methodology for these components are considered equal for the DUUC and the reference aircraft.

Duct

The mass estimation for the duct has previously relied on the sizing of a nacelle, it has been chosen to modify this model. As the duct also serves as a horizontal tail and therefore must comply with the same structural requirements, a mass estimation for the horizontal stabilizer has been used to determine the mass of the duct. The mass estimation to size the horizontal tail plane using the empirical method by Torenbeek [50] is given in Equation 5.1. Here, k_{ht} is 1.0 for fixed-incidence horizontal stabilizers. Note that the sweep angle is measured at the half chord location.

$$m_{duct} = k_{ht} \cdot S_{duct,proj} \cdot \left(62 \cdot \frac{S_{duct,proj}^{0.2} \cdot V_{dive}}{1000 \cdot \sqrt{cos(\varphi_{ht,50})}} - 2.5 \right) \tag{5.1}$$

Pylon and Support

The pylon carries the mass of the DFS and the forces and moments that are generated during flight. In previous work, the pylon mass has been estimated as a percentage of the weight that the pylon is carrying. Van den Dungen [16] used 30%, whilst Vos [11] has shown a strong resemblance with a horizontal tailplane. Stavreva [15] has sized the pylon in detail. For this research, it is important to have a weight estimate available based on the size of the pylon and the forces that act on it as there is no time for a detailed FEM analysis.

Since the shape and function of the pylon and support are shared, a similar approach has been used for its weight estimation. The pylon and support are generalized to an aluminum beam that is sized according to the maximum load of the two load cases visualized in Figure 5.1. Load case 1 is the bending moment that occurs as a result of the aerodynamic load in flight. The second load case involves the

bending moment that is created by the weight of a DFS. The bending moment is used in Equation 5.2 [80] to determine the width of the aluminum beam, this assumes that the height is already fixed to the maximum height available in the airfoil profile. That height is determined based on the NACA 4-series airfoil and chord length. The factor $k_{landing}$ is used to account for the impact during landing and is set to 1.7. This load factor is specified in Section 25.249 of the FAR [81]. Note that other load cases, including buckling, are not considered in the sizing process.

$$m_{beam} = \frac{6 \cdot M_x \cdot n_{ult} \cdot k_{landing}/\sigma_{allow}}{h_{beam}^2} \tag{5.2}$$

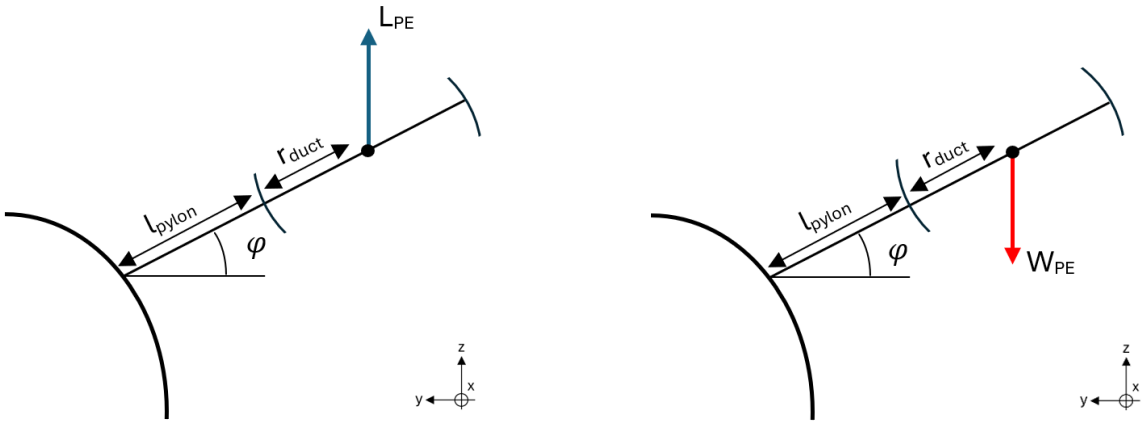

(a) Load case 1: Aerodynamic loading concentrated in center of the duct.

(b) Load case 2: Weight loading concentrated in center of the duct.

Figure 5.1: Free Body Diagram for the load cases used in the sizing for the pylon and support.

The total mass of the pylon and the support is then determined using Equation 5.3. As the moment decreases linearly throughout the beam, the width, and thus the weight, can also decrease linearly over the beam. An additional factor k_{misc} is used to account for the weight of transforming the aluminum beam into a wing. This includes the spars, cover plates, etc.

$$m_{pylon+support} = (h_{beam} \cdot w_{beam} \cdot l_{beam}) \cdot \rho_{alu} \cdot k_{misc} \tag{5.3}$$

Control Vanes

The overall mass of the control system of a transport aircraft can be determined using Equation 5.4. This also includes the control surfaces on the wing. About 25% of this weight is present on the tail, each DFS contains half of the total control surfaces on the tail. Each DFS contains half of the tail controls, and hence Equation 5.4 is multiplied by one eight. The factor k_{sc} is 0.64 for transport aircraft with leading edge high lift devices on the wing [50].

$$m_{control-vane} = \frac{1}{8} \cdot k_{sc} \cdot m_{take-off}^{2/3} \tag{5.4}$$

Nacelle

The turboprop nacelle has been estimated by the estimation provided by Torenbeek, Equation 5.5. The weight is estimated as a percentage of the take-off power of the turboprop.

$$m_{nacelle} = 0.0485 \cdot \frac{P_{take-off} \cdot \eta}{V_{critical} \cdot g} \tag{5.5}$$

Propeller

The propeller assembly is split up in the engine and the fan. To account for the systems that accompany a traditional turboprop engine, the engine mass is estimated by Equation 5.6, according to Torenbeek. The value of m_E is taken from the reference engine of the ATR72-600, the PW127F, which is equal to 481 kg according to the EASA certification sheets [82]. The parameter k_E, in Equation 5.6 accounts for the propeller driven aircraft and is equal to 1.35. The reverse thrust is related to k_{thrust} and is equal to 1.18. The number of engines is given by n_E.

$$m_{engine} = k_{eng} \cdot k_{thrust} \cdot n_{eng} \cdot m_{eng} \tag{5.6}$$

The fan mass is estimated by using the mass of each blade multiplied by the number of blades. An additional 10% is added to account for the spinner mass. Equation 5.7 determines the mass of the fan. This percentage is estimated based on the example fan and spinner masses. The estimation can be found in section C.1.

$$m_{fan} = n_{blades} \cdot m_{blade} \cdot 1.10 \tag{5.7}$$

5.2. Center of Gravity

The center of gravity of the aircraft will be determined using Equation 5.8 for the x-axis and Equation 5.9 for the z-axis. Symmetry on the y-axis of the aircraft is assumed during the whole analysis and hence the center of gravity is assumed to on the center line of the aircraft. When determining the center of gravity in the longitudinal direction, the weight can be broken down into two groups containing the major mass components. The wing and main landing gear will form one group. The second group contains the fuselage, nose landing gear and empennage. When the DUUC is compared to the ATR72, the propulsive group is either in the fuselage group or wing group respectively. A component overview of the components in mass groups for each aircraft is given in Table 5.1. For the center of gravity in z-direction, just Equation 5.9 is used and the components are not broken up in mass groups. The reference point for determining the position of each component is the nose of the aircraft and the bottom line of the fuselage, as indicated in Figure 2.9.

$$x_{cg} = \frac{\sum m_i \cdot x_i}{\sum m_i} \tag{5.8}$$

$$z_{cg} = \frac{\sum m_i \cdot z_i}{\sum m_i} \tag{5.9}$$

Table 5.1: Mass group specification per aircraft type and component for determining the center of gravity in x-direction.

Group	Aircraft	Wing	Main Gear	Nacelle	Engines	Fuselage	Nose Gear	Systems	Prop. Emp.	Vert. Tail	Horiz. Tail
Wing Group	DUUC	●	●								
	ATR	●	●	●	●						
Fuselage Group	DUUC			●	●	●	●	●	●		
	ATR					●	●	●		●	●

The center of gravity of each of the mass groups is determined first using Equation 5.8. After that Equation 5.10 and Equation 5.11 are used to find the center of gravity of the aircraft. It is assumed that the center of gravity of the Leading Edge of the Mean Aerodynamic Chord (LEMAC) is located at a quarter chord of the Mean Aerodynamic Chord (MAC).

$$x_{LEMAC} = x_{FG} - x_{CG,LEMAC} + \frac{m_{WG}}{m_{FG}} \cdot (x_{WG,LEMAC} - x_{CG,LEMAC}) \tag{5.10}$$

$$x_{CG} = x_{CG,LEMAC} + x_{LEMAC} \tag{5.11}$$

5.2.1. Wing Placement Routine

Figure 5.2 illustrates the flow scheme of the iterative process to determine the optimal wing position on the DUUC to ensure longitudinal static stability. An initial estimation of the wing position is made, followed by the calculation of the center of gravity based on that position. This center of gravity is used to determine whether it satisfies the requirements for longitudinal static stability.

If the requirements are not met, the system loops back to determine a new wing position based on the requirements and Equation 5.10, adjusting the location of the center of gravity of the wing group. This loop continues until the design meets the necessary stability requirements, at which point the process ends with the completion of wing positioning.

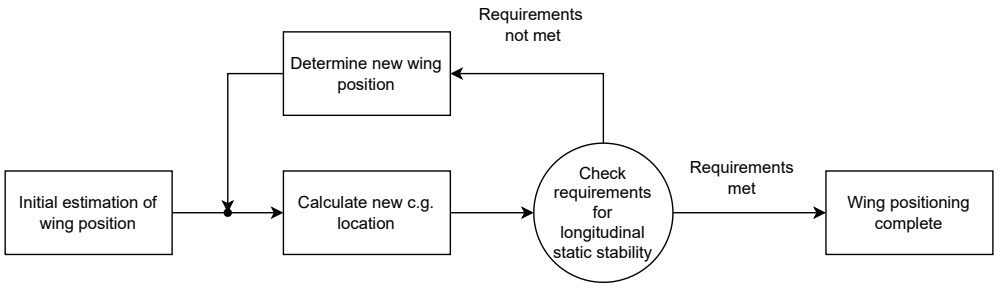

Figure 5.2: Flowchart of the wing placement routine inside the DUUC design code.

5.3. Horizontal Tailplane

In this section the relations are described that set the requirements for the horizontal tail surface. When talking about the required horizontal tail surface for the DUUC, the project area on the xy-plane is meant. This include a small portion of the pylon but mostly the area defined by the duct diameter and chord. First the control requirement is explained after which the stability requirement is lined out. The FBD that is required in the definition is given in Figure 5.3.

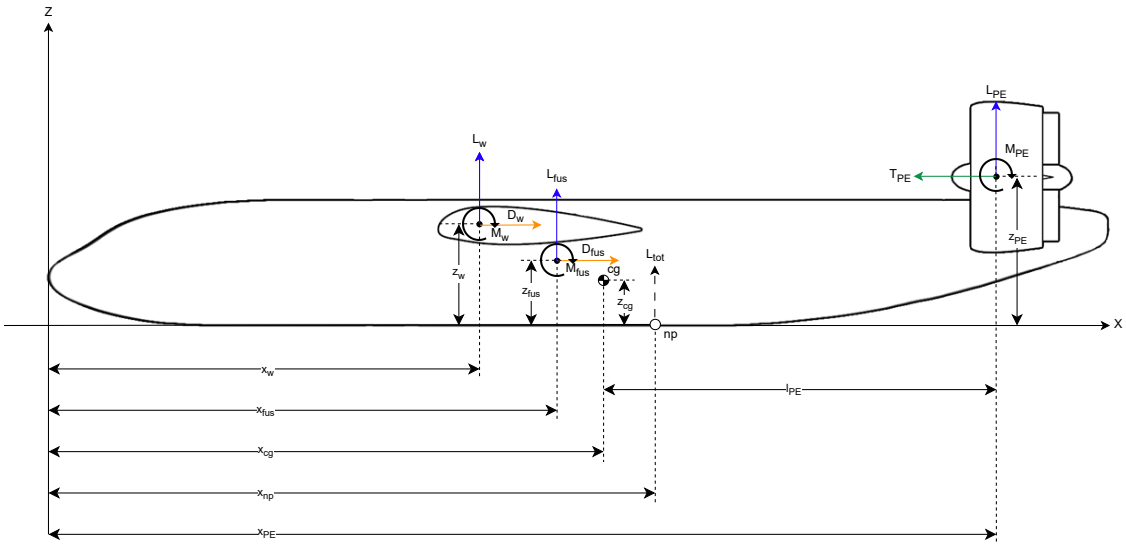

Figure 5.3: FBD with force and moment definitions for horizontal tail surface requirements. Including the definition for the tail arm length.

5.3.1. Control Requirement

In the control requirement treats the situation where the sum of the moment around the center of gravity is set to zero. For conventional aircraft, it can be generalized to Equation 5.12. It should be noted that for conventional aircraft, the moment induced by the empennage is ignored as it is usually small and negligible compared to the moment from the wing. The moment induced by the thrust of the engine is separately treated in $C_{m,eng}$. From this the required area ratio between the wing and the horizontal stabilizer can be determined to satisfy the requirement.

$$C_{M_{cg}} = C_{m,w} + C_L \cdot \overline{x_{CG-AC}} + C_{m,eng} - C_{L,ht} \cdot \eta_H \cdot \frac{S_{ht}}{S_w} \cdot \frac{l_{ht}}{c_{MAC}} = 0 \tag{5.12}$$

The area ratio is given by Equation 5.13 and since the wing area is a fixed parameter in this research, the horizontal stabilizer area is found by using the linear definition in Equation 5.14.

$$\frac{S_{ht}}{S_w} = K_{1_{control}} \cdot \overline{x_{CG-AC}} + K_{2_{control}} \tag{5.13}$$

$$\begin{aligned} K_{1_{control}} &= \frac{C_L}{C_{L,ht} \cdot \eta_{ht} \cdot \frac{l_{ht}}{c_{MAC}}} \\ K_{2_{control}} &= \frac{C_{m,w} + C_{m,eng}}{C_{L,ht} \cdot \eta_{ht} \cdot \frac{l_{ht}}{c_{MAC}}} \end{aligned} \tag{5.14}$$

For the DUUC, the moment induced by the thrust of the engines ($C_{m,eng}$) has a different definition than for a conventional aircraft. As mentioned at the beginning of this section, for conventional aircraft, the moment of the tail around its aerodynamic center is assumed to be negligible. It is unknown however if this assumption will hold for the DUUC as the empennage has a radically different design. For this

reason, the variable $K_{2_{control}}$ in Equation 5.13 is modified to Equation 5.15 for the control requirement of the DUUC.

$$K_{2_{control,DUUC}} = \frac{C_{m,w} + C_{m,PE}}{C_{L,ht} \cdot \eta_{ht} \cdot \frac{l_{ht}}{c_{MAC}}} \tag{5.15}$$

The $C_{m,PE}$ is defined as in Equation 5.16 where a combination is made between the moment induced by the the thrust and the moment induced by the aerodynamic effects. The aerodynamic pitching moment coefficient $C_{m,aerodynamic}$ has been defined in Equation 4.37.

$$C_{m,PE} = C_{Thrust} \cdot z_{PE} + C_{m,aerodynamic} \tag{5.16}$$

5.3.2. Stability Requirement

In the stability requirement the horizontal stabilizer is sized such that the gradient of the pitching moment with angle of attack is negative. When $C_{m,CG}$ at $\alpha = 0$ is chosen, the aircraft is indifferently stable. Equation 5.17 is then used to define the area ratio between the wing and the horizontal tail surface.

$$\frac{\partial C_m}{\partial \alpha} = C_{L_{\alpha_w}} \cdot \overline{x_{CG-AC}} - C_{L_{\alpha_{ht}}} \cdot \eta_{ht} \cdot \frac{S_{ht}}{S_w} \cdot \left(1 - \frac{\partial \epsilon}{\partial \alpha}\right) \cdot \left(\frac{l_{ht}}{c_{MAC}} - \overline{x_{CG-AC}}\right) \tag{5.17}$$

This definition for conventional aircraft leads to the linear relationship in Equation 5.18 where the slope is defined as Equation 5.19.

$$\frac{S_H}{S_W} = K_{1_{stability}} \cdot \overline{x_{CG-AC}} \tag{5.18}$$

$$K_{1_{stability}} = \frac{C_{L_{\alpha_W}}}{C_{L_{\alpha_H}} \cdot \eta_H \cdot \frac{S_H}{S_W} \cdot \left(1 - \frac{\partial \epsilon}{\partial \alpha}\right) \cdot \left(\frac{l_H}{c_{MAC}}\right)} \tag{5.19}$$

This definition can also be applied to the DUUC. The efficiency of the horizontal stabilizer for the DUUC is different compared to the reference aircraft as there is no slipstream effect of the propeller present at the DUUC that would influence the empennage. The influence of the wing on the inflow of the horizontal stabilizer and DUUC is taken into consideration by $\partial\epsilon/\partial\alpha$.

A Static Margin (SM) is included in the analysis to indicate the distance between the neutral point and the center of gravity. The margin used is 5% of the MAC, which is a typical value for subsonic transport aircraft according to Nelson [64].

5.4. Vertical Tailplane

The vertical tailplane of an aircraft is sized based on a control and stability requirement. Where the One Engine Inoperative condition is taken into consideration which leads to a minimum size of the vertical stabilizer. A Free Body Diagram of the DUUC in the OEI condition is shown in Figure 5.4, in order to size the Propulsive Empennage for directional static stability. When the area of the vertical tailplane for the DUUC is discussed in this section, the projected area of the ducts in the xz-plane is meant. Note that there are two ducts present, and hence the area is multiplied by two.

5.4.1. Control Requirement

In the situation where one of the ducted fans is no longer operative, a moment is created by the asymmetric thrust generation and the drag of the inoperative engine. In a conventional configuration, this moment is counteracted by the vertical stabilizer and rudder. For the DUUC, this restoring moment has to come from the ducts and vertical control vanes. The moment equation that arises is given in Equation 5.20, where the moment contribution due to the drag and thrust of the PE is split.

$$M_{PE-T} + M_{PE-D} = M_{restoring} \tag{5.20}$$

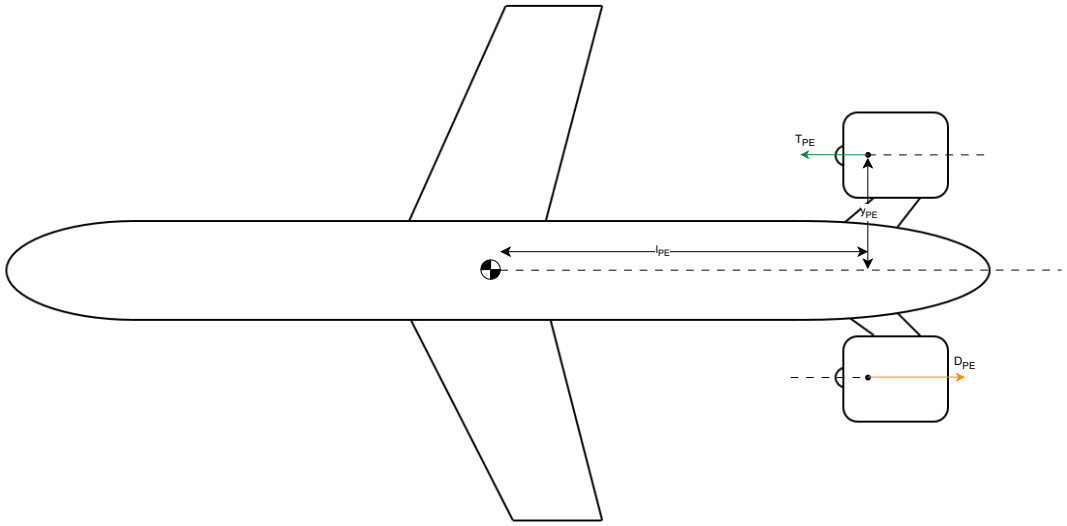

Figure 5.4: Simplified sketch of the free body diagram of the DUUC with asymmetric thrust due to a one engine inoperative condition.

The moment contribution due to thrust is defined by Equation 5.21 where the drag generates the moment in Equation 5.22. The drag of one ducted fan, including the pylon, is added to the additional drag of the windmilling propeller. A feathered situation is omitted as it is assumed to have less drag than the windmill condition. The drag of the ducted fan is determined in chapter 4.

$$M_{PE-T} = \frac{T_{take-off}}{2} \cdot y_{duct-center} \tag{5.21}$$

$$M_{PE-D} = (D_{DFS} + D_{windmilling}) \cdot y_{duct-center} \tag{5.22}$$

To estimate the windmilling drag of the propeller, an approximation of Raymer [51] is used in Equation 5.23. Here, σ is defined as in Equation 5.24.

$$C_{d0-propeller} = \frac{0.5 \cdot \sigma \cdot A_{prop}}{S_{ref}} \tag{5.23}$$

$$\sigma = \frac{n_{blade}}{AR \cdot \pi} \tag{5.24}$$

The restoring moment of the PE is a combination of the side force of the duct and the control vane effectiveness. As the duct is an axisymmetric body, the side force can be derived with a similar approach as the lift force of the duct. However the inflow angle is now not the angle of attack α but the sideslip angle β. The inflow angle of the duct must be corrected because of a sidewash effect as concluded by Harinarain [13]. The side force contribution of the support and pylon is also taken into consideration, as well as the normal force of the propeller. Equation 5.25 gives the relation for the side force coefficient.

$$C_Y = C_{L_{\beta,duct}} \cdot \beta_{effective} + C_{L_{\delta r}} \cdot \delta_r + C_{Y_{pylon}} + C_{Y_{support}} \tag{5.25}$$

The surface area of the vertical tail of a conventional empennage would be given by Equation 5.26.

$$S_{vt} = \frac{M_{PE-T} + M_{PE-D}}{\frac{1}{2} \cdot \rho \cdot V_\infty^2 \cdot C_Y \cdot l_{vt}} \tag{5.26}$$

5.4.2. Stability Requirement

When examining the directional stability of the DUUC, Equation 5.27 has to be used. An FBD of the situation is shown in Figure 5.5. The aim is to have $C_{N_\beta}>0$ for stability. The fuselage and wing contribution have a destabilizing effect. As the aircraft operates at low speeds and the sweep of the

wing is small, the contribution is assumed to be negligible and is omitted when determining the required vertical tail surface. It must be noted that the effective sideslip angle is different for both DFS on the DUUC. The DFS that is effected by the flow over the fuselage has σ as a sideslip angle which is defined in Equation 5.24.

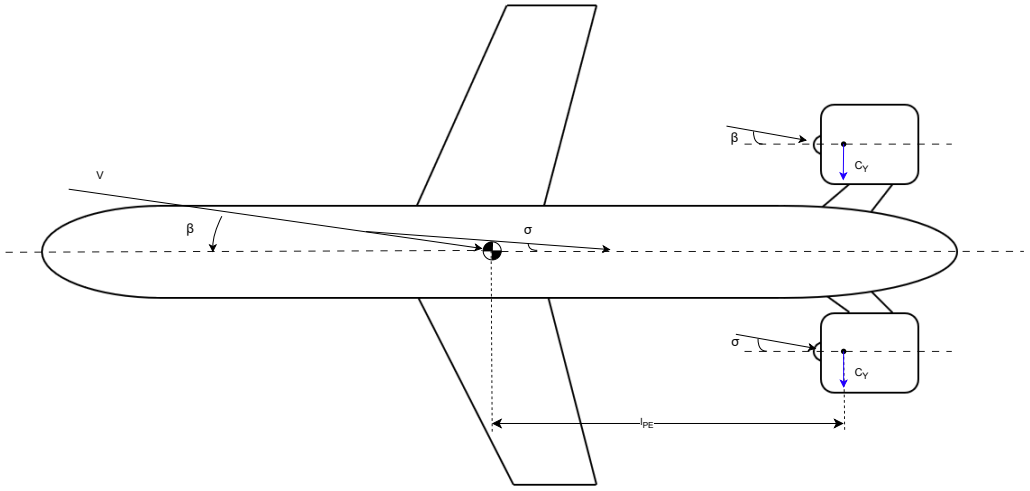

Figure 5.5: FBD of the DUUC under sideslip condition with effective sideslip per DFS.

$$C_{N_\beta} = C_{N_{\beta,fus}} + C_{N_{\beta,w}} + C_{Y_{\beta,PE}} \tag{5.27}$$

Equation 5.27 can be modified to Equation 5.28 where the ratio between the vertical tail surface and wing surface can be defined for a conventional configuration.

$$\frac{S_{vt}}{S_w} = \frac{C_{N_\beta} - C_{N_{\beta,fus}}}{-C_{Y_{\beta,PE}}} \cdot \frac{b_w}{l_{vt}} \tag{5.28}$$

The fuselage contribution $C_{N_{\beta,fus}}$ is determined using Equation B.4 defined by DATCOM [71]. Where the dimensions and geometric shape of the fuselage plays a role. The coefficients $K_{R,J}$ and K_N are defined in Appendix B. Roskam [83] provides an assumption for the total value of C_{N_β} which is $\geq \frac{0.001}{deg}$.

$$C_{N_{\beta,fus}} = -\frac{360}{2 \cdot \pi} \cdot k_N \cdot K_{R,J} \cdot \frac{l_F^2 \cdot d_F}{S_w \cdot b} \tag{5.29}$$

The side force coefficient $C_{Y_{\beta,PE}}$ can be derived from Equation 5.25 provided in the control requirement.

5.5. Stability Derivatives

The stability derivatives with respect to angle of attack and sideslip are covered in this section. Reference lengths that are used can be found in the airplane definition in Figure 5.4.

5.5.1. Stability Derivatives with Respect to Angle of Attack

The lift curve slope of the entire aircraft is defined by adding the two main contributors to each other using an area based normalization. The definition for a conventional aircraft is shown in Equation 5.30. The tail efficiency factor η_h is defined as the ratio between the dynamic pressure at the wing and at the horizontal stabilizer q_h/q_w and is less than 1 by definition.

$$C_{L_\alpha} = C_{L_{\alpha_w}} + C_{L_{\alpha_{ht}}} \cdot \eta_{ht} \cdot \left(\frac{S_{ht}}{S_w}\right) \cdot \left(\frac{\partial \alpha_{ht}}{\partial \alpha}\right) \tag{5.30}$$

For the DUUC, aircraft the lift curve slope of the horizontal stabilizer has to be replaced by the lift curve slope of the PE, which is defined in Equation 5.31. The project area in the xy-plane is defined in Equation 5.32 which leads to the definition for C_{L_α} in Equation 5.33. The tail efficiency factor is defined similar to the conventional case, the value however is slightly higher as the PE do not have to take the propeller slipstream effects into consideration in the intake.

$$C_{L_{\alpha,PE}} = C_{L_{\alpha,duct}} \cdot \frac{2 \cdot S_{proj,duct}}{S_{proj}} + C_{L_{\alpha,pylon}} \cdot \frac{2 \cdot S_{pylon}}{S_{proj}} \cdot cos(\phi) + C_{L_{\alpha,support}} \cdot \frac{2 \cdot S_{support}}{S_{proj}} \cdot cos(\phi) \tag{5.31}$$

$$S_{proj} = 2 \cdot c_{duct} \cdot d_{duct} + (2 \cdot b_{pylon} \cdot c_{pylon}) \cdot cos(\phi) \tag{5.32}$$

$$C_{L_\alpha} = C_{L_{\alpha,w}} + C_{L_{\alpha,PE}} \cdot \eta_{PE} \cdot \left(\frac{S_{proj}}{S_w}\right) \cdot \left(\frac{\partial \alpha_{PE}}{\partial \alpha}\right) \tag{5.33}$$

The pitching moment coefficient with respect to alpha determines the stability of the aircraft. Where the aim should be to have a negative value for $dC_m/d\alpha$. For this analysis, a simplified version is used where all the tangential forces of all components are ignored and the slipstream and thrust effects are not considered. The three main contributors to stability derivative are the wing, fuselage and empennage. C_{m_α} for a conventional aircraft is defined in Equation 5.34. The length l_{ht} is the length between the center of gravity and the quarter chord of the horizontal stabilizer.

$$C_{m_{\alpha_{conv}}} = C_{N_{\alpha,w}} \cdot \frac{x_{c.g.} - x_w}{\bar{c}} + C_{N_{\alpha,fus}} \cdot \frac{x_{c.g.} - x_{fus}}{\bar{c}} - C_{N_{\alpha,ht}} \cdot \left(1 - \frac{\partial \epsilon}{\partial \alpha}\right) \cdot \left(\frac{V_{ht}}{V_\infty}\right)^2 \cdot \frac{S_{ht} \cdot l_{ht}}{S \cdot \bar{c}} \tag{5.34}$$

Usually, the fuselage provides a strong destabilizing effect whilst the wing is slightly destabilizing and the horizontal stabilizer provides a stabilizing effect. The definition in Equation 5.34 can be used to determine C_{m_α} for the DUUC, except the contribution of the horizontal stabilizer is replaced by the term in Equation 5.35. The projected surface area S_{PE} includes the projection in the xy-plane of the both ducts and the pylons. The control vanes are not includes as their area that is outside the duct is small and their force gradient is smaller compared to the contribution of the ducts.

$$C_{N_{\alpha_{PE}}} \cdot \left(1 - \frac{\partial \epsilon}{\partial \alpha}\right) \cdot \left(\frac{V_{PE}}{V}\right)^2 \cdot \frac{S_{proj} \cdot l_{PE}}{S_w \cdot \bar{c}} \tag{5.35}$$

The above-mentioned relation only takes the contributions with respect to the x-axis into consideration. The pendulum stability of the aircraft, which has to do with the z-contributions, has not specifically been mentioned in previous studies. The drag component with respect to the center of gravity in the z-axis are usually small for conventional aircraft but are worth investigating for the DUUC. Perkins [84] describes that the contribution of the wing is stabilizing if the center of gravity in z-direction is below the wing's aerodynamic center. The contribution of the wing, on the pendulum stability is given in Equation 5.36.

$$\left(\frac{\partial C_m}{\partial C_L}\right)_{wing,pendulum} = C_L \cdot \left(\frac{2}{\pi \cdot e \cdot AR} - \frac{0.035}{\partial C_L/\partial \alpha}\right) \cdot \frac{z_a}{c} \tag{5.36}$$

Where usually the z-contribution of the tail is ignored because of the magnitude, it first has to be considered for the DUUC in order to determine how great the contribution is. Equation 5.37 gives the contribution for the PE, where the wing contribution of Perkins [84] is modified to represent the tail contribution.

$$\left(\frac{\partial C_m}{\partial C_L}\right)_{PE,pendulum} = \left(\frac{\partial C_D}{\partial C_L} - C_L \cdot \frac{\partial \alpha}{\partial C_L}\right) \cdot \frac{z_a}{c} \tag{5.37}$$

The final equation to determine the pitching moment coefficient with respect to angle of attack is given in Equation 5.38.

$$\begin{aligned} C_{m_{\alpha_{DUUC}}} = C_{N_{w_\alpha}} \cdot \frac{x_{c.g.-x_w}}{\bar{c}} + C_{N_{fus_\alpha}} \cdot \frac{x_{c.g.-x_{fus}}}{\bar{c}} - C_{N_{PE_\alpha}} \cdot \left(1 - \frac{\partial \epsilon}{\partial \alpha}\right) \cdot \left(\frac{V_{PE}}{V}\right)^2 \cdot \frac{S_{proj} \cdot l_{PE}}{S \cdot \bar{c}} \\ + \left(\frac{\partial C_m}{\partial C_L}\right)_{wing,pendulum} + \left(\frac{\partial C_m}{\partial C_L}\right)_{PE,pendulum} \end{aligned} \tag{5.38}$$

5.5.2. Stability Derivatives with Respect to Sideslip Angle

The side slipping motion of an aircraft generates a lateral force that is usually negative at positive angles of sideslip. For a conventional tailplane, the contribution of the vertical stabilizer is given by Equation 5.39 according to Mulder et al. [63]. The sideslip angle has to be corrected for the presence of the fuselage by a small sidewash angle σ. The effective inflow angle of the vertical stabilizer then becomes α_v in Equation 5.40.

$$C_{Y_{\beta_{vt}}} = -C_{Y_{\alpha,vt}} \cdot \left(1 - \frac{\partial \sigma}{\partial \beta}\right) \cdot \left(\frac{V_{vt}}{V_\infty}\right)^2 \cdot \frac{S_{vt}}{S_w} \tag{5.39}$$

$$\alpha_{vt} = -(\beta - \sigma) \tag{5.40}$$

The principle of calculating this coefficient can be applied to the PE, where only the force gradient of the vertical stabilizer is replaced by lift curve slope of the duct's. As the ducts are axi-symmetrical their lift curve slope also applies to an angle of sideslip. As the inflow angle of the control vanes, and support are dependent on the operating conditions inside the duct, added to the fact that their surface is very small, their effect on the sideslip coefficient is neglected. Thus, only the duct's influence is taken into consideration. Each of the ducts will generate a force, the projected area of the PE in the xz-plane is multiplied by two to include both contributions. The definition of C_{Y_β} for the DUUC is given in Equation 5.41.

$$C_{Y_{\beta_{DUUC}}} = -C_{L_{\alpha,duct}} \cdot \left(1 - \frac{\partial \sigma}{\partial \beta}\right) \cdot \left(\frac{V_{duct}}{V_\infty}\right)^2 \cdot \frac{2 \cdot S_{proj}}{S_w} \tag{5.41}$$

It must be noted that the presence of two ducted fans next to each other will influence the flow field around each other and hence also influence the effective sideslip angle. This effect has been research for open rotors and show that the effect is small when the distance between the two is above three times the blade radius as specified in the paper of Stokkermans [85]. Since there is no specific information available on the effect of distance between ducted fans, the interference effect between the two DFS with respect to the side slip coefficient is not taken into consideration.

The stability derivative C_{n_β} defines the weathercock stability of the aircraft. The contribution of a vertical stabilizer is defined in Equation 5.42. Here, the tail lever arm l_{vt} (at small angles of attack)

is defined as the distance between the center of gravity and the quarter chord point of the vertical stabilizer.

$$C_{n_{\beta_{vt}}} = C_{Y_{\beta,vt}} \cdot \left(1 - \frac{\partial\sigma}{\partial\beta}\right) \cdot \left(\frac{V_{vt}}{V_\infty}\right)^2 \cdot \frac{S_{vt} \cdot l_{vt}}{S_w \cdot b} \tag{5.42}$$

For the DUUC, this definition can be applied where the C_{Y_β} is used as defined in Equation 5.41 and the definition of l_{PE} defines the location between the center of gravity and the quarter chord point of the duct. It must be noted that only of the DFS is experiencing the influence of the fuselage whilst the other does not. The coefficient for the DUUC is given in Equation 5.43.

$$C_{n_{\beta_{DUUC}}} = C_{Y_{\beta,DUUC}} \cdot \left(1 - \frac{\partial\sigma}{\partial\beta}\right) \cdot \left(\frac{V_{PE}}{V_\infty}\right)^2 \cdot \frac{2 \cdot S_{proj} \cdot l_{PE}}{S_w \cdot b} \tag{5.43}$$

5.6. Control Derivatives

The control derivatives will determine the control regime of the aircraft. As lateral stability is not included in this analysis, only elevator and rudder deflections are considered, and roll is ignored. DUUC V0.1 contains a control vane configuration where the controls are placed in an "X" configuration. This setup is illustrated in Figure 5.6. The ideas has been mentioned to improve the control vane setup by moving the control surfaces to the edge of the duct but this has not been researched yet. In this thesis, the "duct-edge" configuration is added to compare the with the DUUC V0.1 configuration. The duct-edge control vane setup is depicted in Figure 5.7.

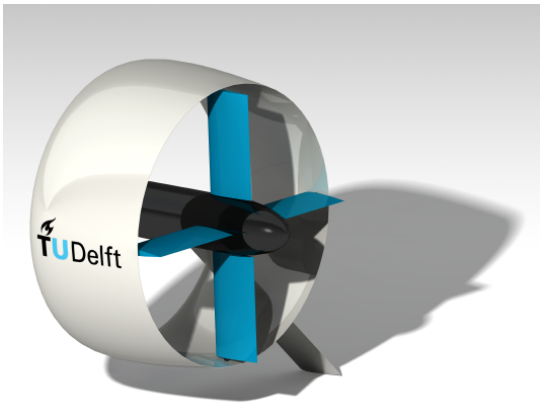

Figure 5.6: Rear view of a DFS with the control vanes in "X" configuration [1].

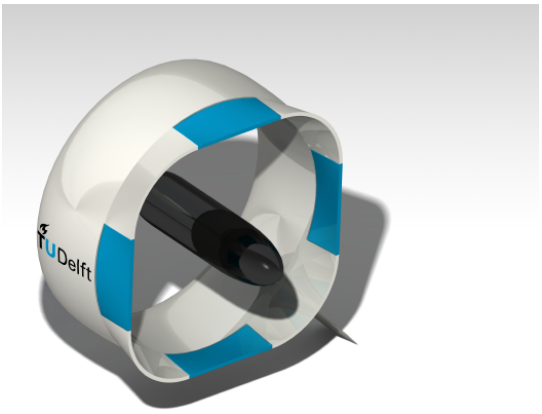

Figure 5.7: Rear view of a DFS with the control vanes in "duct-edge" configuration [1].

5.6.1. Control Derivatives with Respect to Elevator Deflection

The change in normal force due to the deflection of the elevator is defined by Equation 5.44. Where the slope of the lift curve $C_{N_{\delta_e}}$ is the slope of the lift curve defined by the 2D airfoil section of the control vane when the control vanes are in the X-configuration.

$$C_{N_{\delta_e}} = C_{N_{\delta e}} \cdot \left(\frac{V_{control-vane}}{V_\infty}\right)^2 \cdot \frac{S_{elevator}}{S_w} \tag{5.44}$$

When the control vanes are in the duct-edge configuration, the $C_{N_{\delta_e}}$ has been experimentally determined by means of an AVL exercise where an equivalent box wing has been modeled with control vanes on the trailing edges of each section. The setup used for this is illustrated in Figure 5.8. The definition for the control derivative remains unchanged when a different configuration in control vanes is used. Changing the control vane configuration does change some other effects inside the DFS which will be explained in chapter 6.

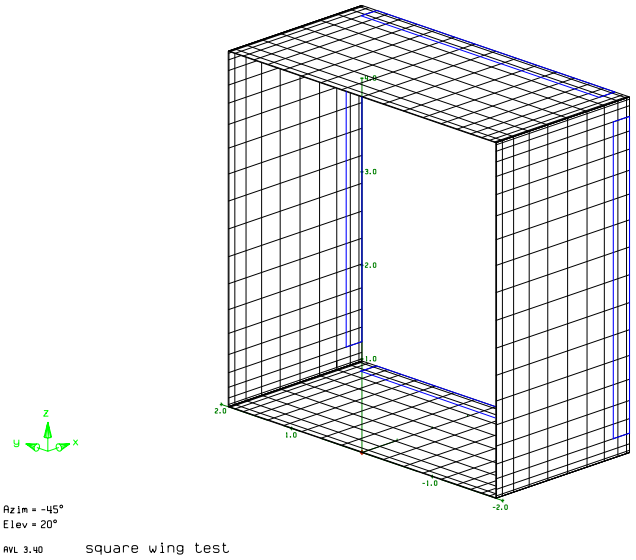

Figure 5.8: AVL setup that is used to determine the $C_{N_{\delta_e}}$ and $C_{Y_{\delta_r}}$ value for the PE when the control vanes are in the duct-edge configuration. The control vanes are indicated in blue.

The effect of elevator deflection on the pitching moment coefficient is expressed in $C_{m_{\delta_e}}$. The definition for both configuration control vanes does not change and is equal to Equation 5.45. It must be noted that the elevator area $S_{elevator}$ is the combined area of the elevators of both DFS.

$$C_{m_{\delta_e}} = C_{N_{\delta_e}} \cdot \left(\frac{V_{control-vane}}{V_\infty} \right)^2 \cdot \frac{S_{elevator} \cdot l_{PE}}{S_w \cdot \bar{c}} \tag{5.45}$$

5.6.2. Control Derivatives with Respect to Rudder Deflection

As the situation in the ducts is axis symmetric, it can be observed that the force gradients from the elevators also apply for the rudder deflections. The lateral force change due to rudder deflection is expressed as Equation 5.46 for the DUUC. Where the force gradient for the X-configuration rudder is defined as the lift curve slope of the 2D airfoil section. For the duct-edge configuration the value is obtained in a similar fashion as explained in subsection 5.6.1.

$$C_{Y_{\delta_r}} = C_{Y_{\delta_r}} \cdot \left(\frac{V_{control-vane}}{V} \right)^2 \cdot \frac{S_{elevator}}{S} \tag{5.46}$$

The control derivative $C_{n_{\delta_r}}$ is then given by Equation 5.47. The definition remains unchanged when the control vane model changes.

$$C_{n_{\delta_r}} = -C_{Y_{\delta_r}} \cdot \frac{l_{PE}}{b} \tag{5.47}$$

5.7. Model Validation

The flight mechanics section of the IAFM is validated using reference data and compared to the output of the IAFM when the ATR is modeled. The mass estimation is validated after which that can be compared in the center of gravity estimation. The horizontal tail and vertical tail sizing routine are shown and the control and stability derivatives are compared to the reference case.

5.7.1. Mass Estimation

The component mass is validated with the ATR reference data and the previous mass estimations of the Propulsive Empennage. To determine the influence of the deviations in the estimation, the mass difference is also expressed as a percentage of the Maximum Take-Off Mass of the ATR. Table 5.2 gives the validation and deviations.

Table 5.2: Mass prediction of empennage components and validation with various references.

Component	**IAFM Mass** $[kg]$	**Estimation Nita** [62] $[kg]$	**Estimation van den Dungen** [16] $[kg]$	**Estimation Stavreva** [15] $[kg]$	**Δ Mass (maximum)** $[kg]$	**Δ Mass (maximum)** [%]
Hor. Tail	146	124			+ 22	+ 0.09
Ver. Tail	178	178			+ 0	+ 0.00
Duct	261		265	231	- 30	- 0.13
Pylon + Support	269		359	115	+ 151	+ 0.66
Nacelle	228	241	196	219	- 32	- 0.14
Engines	1532	1532			+ 0	+ 0.00

The largest difference between the IAFM and the reference data can be found in the estimation of the pylon and support. The maximum deviation is less than 1% of the MTOM. However, the relative component deviation for the pylon and support is 56%. This has to do with the approach that is used to estimate the mass. Stavreva performs a detailed FEM analysis to determine the mass of the component based on several load cases. Van den Dungen does a prediction that treats the pylon and support as a horizontal stabilizer. The scope of this analysis does not allow for a detailed FEM analysis and the value is between the value of Stavreva and van den Dungen. The decision is made to keep the current approach for the mass prediction from the IAFM.

The deviation for the horizontal tail has to do with the double sweep correction that is applied in the reference study but is not present in the IAFM. For the nacelle, the methodologies from Stavreva and van den Dungen are different from those of Nita. To be able to compare the ATR aircraft with the DUUC configuration, the approach of Nita has been chosen to allow for a fair comparison.

Concluding that the overall difference relative to the MTOM is less than 2%, the IAFM is not adjusted and will be used in the overall performance evaluation.

5.7.2. Center of Gravity

The above described method is used to model the reference aircraft in the IAFM and compare the available values for the ATR72-600 aircraft [62], in order to validate the IAFM before the application to the DUUC. Figure 5.9 shows that the IAFM is in good agreement with the reference values. The minor differences present are due to slightly different mass predictions for the wing and the center-of-mass location of the fuselage body.

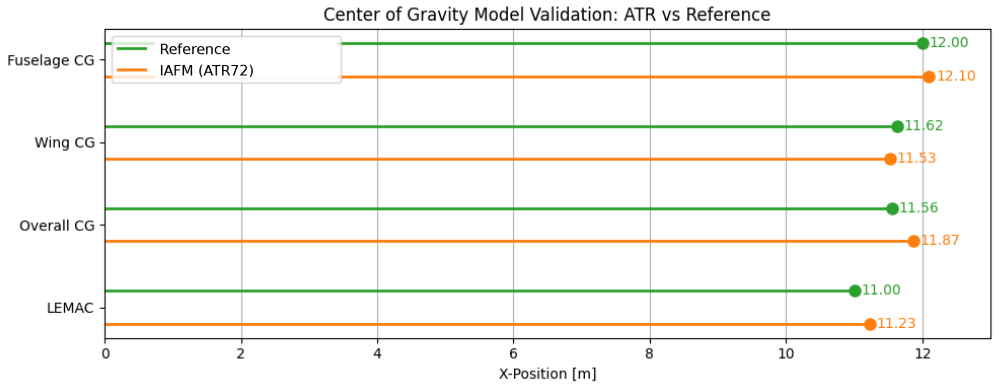

Figure 5.9: Center of Gravity position measured from the nose of the aircraft for the different mass groups.

5.7.3. Horizontal Tail Sizing

To validate that the horizontal tail sizing routine is setup properly, the ATR aircraft is modeled and the horizontal tail is sized based on the data available. The prediction model output compared to the reference data of Scholz [86]. Figure 5.10 shows the stability and control requirements lines of the reference data in dashed compared to the IAFM. It is observed that the control line of the IAFM is slightly less steep and has a higher value for the constant in the linear relationship. For the stability relation, the IAFM slopes are less steep. The values of the slopes are given in Table 5.3 for easier comparison.

Table 5.3: Reference [86] and IAFM values for the control and stability requirements in the horizontal tail sizing routine.

Parameter	Unit	Reference value	IAFM value
$K_{1_{control}}$	[-]	-0.4887	-0.4723
$K_{2_{control}}$	[-]	0.2076	0.2379
$K_{1_{stability}}$	[-]	0.3050	0.2937
x_{cg}	[m]	0.3086	0.3286
S_{ht}/S_w	[-]	0.1442	0.1445

The difference in values for the control requirements can be attributed to the fact that the center of gravity is slightly different and hence the tail lever arm (l_{ht}) is at a different location. Additionally, the moment induced by the engine $C_{M,eng}$ is calculated with power by Nita [62], but the IAFM uses thrust for convenience in the setup for the DUUC. Hence, a small offset. For the stability requirement, the different center of gravity has the same effect as with the control line and the lift curve slope of the wing is different in the IAFM. Where Nita [62] uses a formulation where the sweep at a half chord is included, the IAFM uses the quarter chord sweep which results in a small offset.

Figure 5.11 shows a zoomed version of Figure 5.10 in order to see the effect of the difference predicted values in terms of the relative area ratio between the horizontal tail and the wing. The reference data give an area ratio of 0.1442 whilst the IAFM predicts 0.1445. This deviation of 0.2% leads to an over-prediction in the area of the horizontal tail surface of 0.018 m^2, which is deemed accurate enough for this analysis. And as the model is over-predicting, the model is on the conservative side.

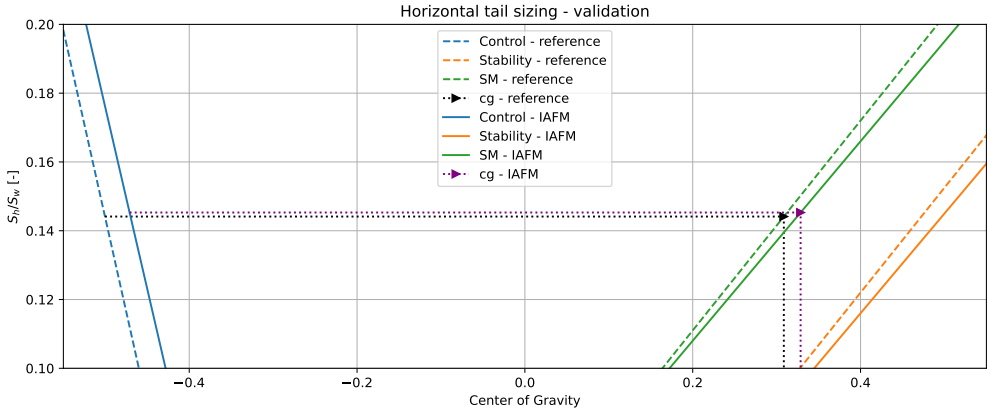

Figure 5.10: Validation of the area ratio between the horizontal tail and wing surface. Control and stability requirements from the IAFM compared with reference data.

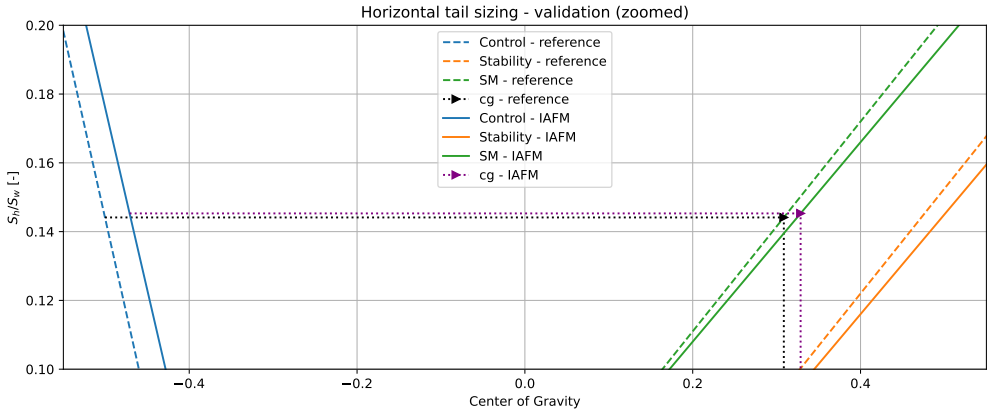

Figure 5.11: Difference in area ratio between reference data and IAFM for horizontal tail sizing routine.

5.7.4. Vertical Tail Sizing

The vertical tail sizing routine is validated in a similar fashion to the horizontal tail routine. The slightly different center of gravity that has been mentioned before also has effect on the tail lever arm for the vertical stabilizer which results in different prediction lines for both the side force coefficient and the yawing moment coefficient, given in Figure 5.12a and Figure 5.12b respectively.

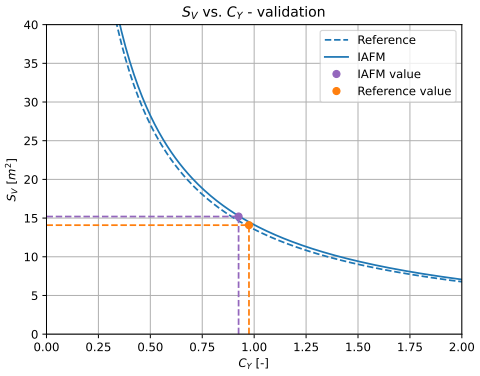

(a) Validation of restoring moment of the vertical tail with respect to the vertical tail surface.

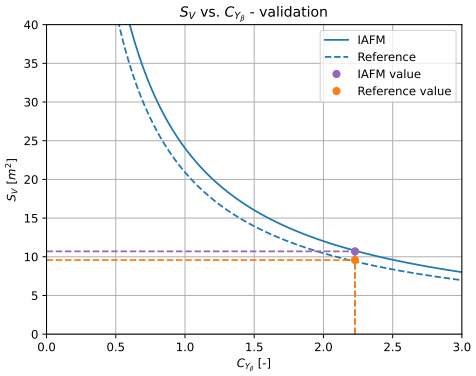

(b) Yawing moment coefficient validation with respect to the vertical tail surface.

Figure 5.12: Vertical tail sizing routine validation with reference data from Scholz [62].

In Figure 5.12a it can be seen that the side-force coefficient C_Y is also predicted differently in the IAFM. This has to do with the sweep applied by Nita [62], which deviates from the technical information in the certification sheet of the ATR [18]. This leads to a difference in vertical tail surface of 1.15 m^2 which is equal to 8%. When the same side force coefficient (0.975) is used the model only has a deviation of 2.8 % from that it is concluded that the model is accurate enough for the analysis. Again, the IAFM is over-predicting and hence on the conservative side.

For both the reference and IAFM, the same C_{Y_β} value is found. The difference in tail lever arm results in the deviation between the two lines and result in a difference in tail area of 1.13 m^2 equal to 11.8 %. When the same lever arm is used, the IAFM matches the reference data exactly, from which is concluded that the model is accurate enough but care must be taken with the tail lever arm in the analysis.

5.7.5. Stability Derivatives

The stability derivatives with respect to angle of attack and sideslip are shown in Table 5.4. The values are compared to the numerical prediction model of Vecchia [87]. The difference between the IAFM and

reference values are attributed to rounding errors in the iteration loops and the difference in tail arm length. Where the tail arm length for the reference aircraft is set to be 14.3 meters, the IAFM uses 13.8 due to a different prediction in center of gravity.

Table 5.4: Validation of stability derivative model with reference values [87].

Derivative	Unit	Reference value	IAFM value
C_{L_α}	$[rad^{-1}]$	5.7327	5.7231
C_{M_α}	$[rad^{-1}]$	-1.6671	-1.6672
C_{Y_β}	$[rad^{-1}]$	-0.7283	-0.7278
C_{N_β}	$[rad^{-1}]$	0.1441	0.1286

5.7.6. Control Derivatives

Similarly to the stability derivatives, the IAFM of the control derivatives are compared to reference data of Vecchia. The results are given in Table 5.5. The small deviations are due to rounding error and the different tail arm length. When the same tail arm length is used, the maximum error reduces to 1.8 % which is acceptable.

Table 5.5: Validation of control derivative model with reference values [87].

Derivative	Unit	Reference value	IAFM value
$C_{L_{\delta_e}}$	$[rad^{-1}]$	0.3051	0.3048
$C_{M_{\delta_e}}$	$[rad^{-1}]$	-1.7245	-1.6837
$C_{Y_{\delta_r}}$	$[rad^{-1}]$	-0.6312	-0.6310
$C_{N_{\delta_r}}$	$[rad^{-1}]$	-0.3273	-0.2921

Part III

Results

6

Results

In this chapter, the results of the DUUC V0.1 analysis are explained in terms of aerodynamic performance and evaluation of flight mechanics. A sensitivity analysis is performed to show how certain requirements affect the performance and design of the DUUC. Before the results are shown, the reference aircraft is explained together with the Key Performance Indicators (KPI's) and the two main configurations that will be analyzed.

Reference Aircraft

The reference aircraft to which the DUUC is compared is the ATR72-600. This short-haul aircraft focuses on efficiency and passenger comfort and is designed according to the top level requirement as given in Table 6.1. An image of the ATR72-600 is shown in Figure 6.1.

Figure 6.1: Image of the ATR72-600 aircraft [18].

Table 6.1: Harmonic mission top level requirements of the ATR72-600 [11, 88]

Parameter	Value	Unit
Payload mass (68 pax)	7500	[kg]
Range (max payload)	1528	[km]
Cruise altitude	7000	[m]
Cruise Mach number	0.45	[-]

In previous studies, the DUUC wing-body was based on sizing requirements and information from the Boeing 737-800 and ATR mission requirements. In this study the decision has been made to base the wing-body on the ATR aircraft as well and to transfer the DUUC design into a high-wing configuration. This allows for a comparison that is more fair and there is significantly more data publicly available from the ATR. Certain stability effects will then be one-to-one comparable instead of having to make a translation from a high-wing to low-wing configuration.

Table 6.2: ATR72-600 baseline parameters used for the comparison with the DUUC [62, 88, 87].

Parameter	Value	Unit
MTOM	22,800	[kg]
OEM	13,010	[kg]
Wing span	27.05	[m]
Fuselage length	27.17	[m]
Fuselage diameter	2.83	[m]

The ATR data that are used to form the baseline of the comparison are given in Table 6.2. Additional data and calculations for certain parameters like fuselage weight and wing weight are provided in Appendix B.

Key Performance Indicators

The overall performance of the DUUC will be evaluated by means of a few KPI's.

- Operational Empty Mass
- Maximum Take Off Mass
- Lift to Drag ratio
- Aircraft drag
- Propulsive efficiency
- Fuel fraction

6.1. Empennage Comparison

The performance of the PE is compared with the performance of the ATR empennage to determine the advantages and disadvantages of each empennage.

6.1.1. Aerodynamic Performance

The lift curve for the ATR72-600 and the PE are depicted in Figure 6.2. The lift coefficients for both empennages are normalized with the wing surface area. As illustrated in this figure, the PE produces more lift compared to the conventional empennage. However, the lift curve slope of the conventional empennage is steeper. This difference decreases when the PE is turned on and the C_{L_α} value is multiplied by a square root factor of the thrust coefficient.

The symmetric empennage for the ATR does not produce any lift when the angle of attack is zero. The PE does produce some lift on the nacelle and as a result of the installation angle of the support inside the PE. Additionally, it is shown that towards the stall region of the conventional empennage, the PE has not reached the stall yet. This is due to the delay in stalling of the ducts which will occur towards 17 degree angle of attack.

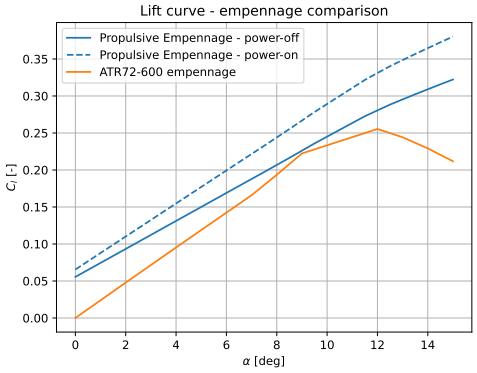

Figure 6.2: Lift polar comparison between the PE and ATR empennage.

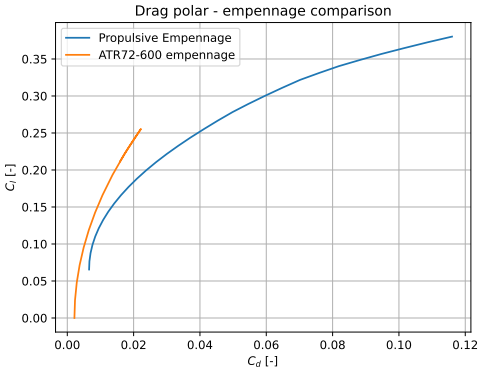

Figure 6.3: Drag polar comparison between the PE and ATR empennage.

The drag polar in Figure 3.12 shows that the PE has a higher value of zero-lift drag, but also a faster increase in lift induced drag compared to the empennage of the ATR. From this figure, it can be concluded that the use of the PE would not be favorable in aerodynamic performance compared to the conventional empennage.

When determining the pitching moment coefficient of the aircraft with respect to the angle of attack, the moment of the empennage is usually neglected due to its size. When comparing the pitching moment coefficient of the ATR72 with the DUUC in Figure 6.4 it is demonstrated that for the DUUC, the pitching moment contribution of the tail is not negligible and should be taken into account.

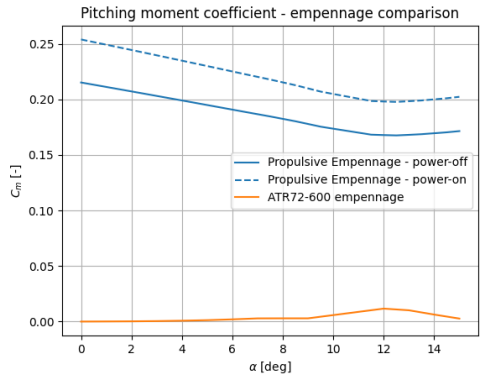

Figure 6.4: Pitching moment coefficient over angle of attack comparison between empennages.

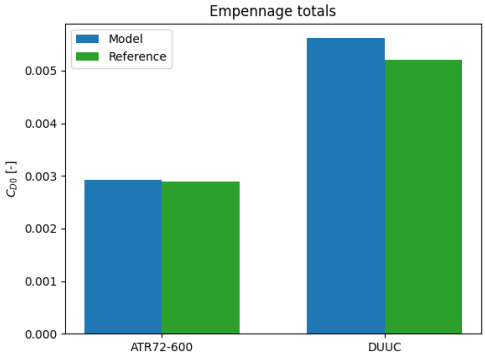

Figure 6.5: Zero lift drag empennage comparison between the ATR72-600 and the PE at $V_\infty = 128$ m/s, with a reference surface of the main wing.

Zero Lift Drag

The zero lift drag of the empennage of the ATR and the empennage of the DUUC V0.1 are compared in Figure 6.5. From this can be observed that the C_{D0} for the PE is almost twice as large as the conventional empennage of the ATR. This can be attributed to the increase in wetted area between the two empennages. The conventional empennage has a wet area of 62 m^2 whilst the PE has 107 m^2. The ducts have the largest contribution to the wetted area of the empennage.

6.1.2. Mass Estimation

The mass estimation for one DFS is given in Table 6.3 in the V.01 configuration. When the force-generating surfaces are compared between the two empennages, it can be observed that the DUUC is more than 750 kg heavier compared to the ATR. The propulsion generating components have the same weight for both airplanes. However, the tail load for the DUUC is 3050 kg larger compared to the ATR. Figure 6.6 shows the weight division for both aircraft.

Table 6.3: Component mass estimation of one DFS V0.1 excluding control vanes.

Component	Value [kg]
Duct	261
Pylon	105
Support	165
Nacelle	228
Engine + fan	921
Total	1680

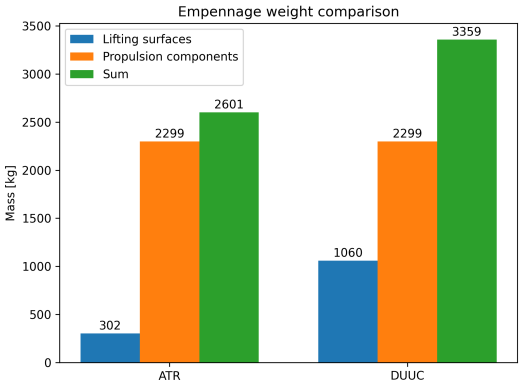

Figure 6.6: Empennage mass comparison between ATR and DUUC.

6.2. Configuration Comparison

For the evaluation of the feasibility of the aircraft employing a Propulsive Empennage concept, two main configurations will be analyzed.. Configuration 1, is the configuration that has been analyzed in the past that employs the PE at the rear end of the fuselage acting in a location similar to a conventional tailplane. Configuration 1 is depicted in Figure 6.7. The second configuration is a configuration where the PE is placed at the front of the aircraft, just after the cockpit, where the PE acts like a canard, shown in Figure 6.8. The PE location on the fuselage is given in Table 6.4, the longitudinal direction is normalized with the fuselage length where the lateral and vertical position are normalized with fuselage

diameter. Note that for configuration 2, the fuselage length as been shortened because of unused tail area on the fuselage.

For both configurations it has been tried to keep the PE in the same distance from the end of the aircraft. So for configuration 1, 10% of the rear end. That would imply for configuration 2 that it would need to be 10% from the front of the aircraft. The PE would then be on 2.1 meter from the front and interfere with the cockpit. Thus it has been decided to place the empennage at 20% of the fuselage length, which would equal 15% of the fuselage length if the original fuselage length was taken. Because of the shape of the tail, configuration 1 is closer to the center line of the aircraft in y-direction.

Table 6.4: PE position on the fuselage for both configurations.

Configuration	l_{fus} $[m]$	d_{fus} $[m]$	**x** [-]	**y** [-]	**z** [-]
ATR72-600	27	2.87	0.90	0.00	1.00
Configuration 1	27	2.87	0.90	0.18	0.90
Configuration 2	21	2.87	0.15	0.25	0.90

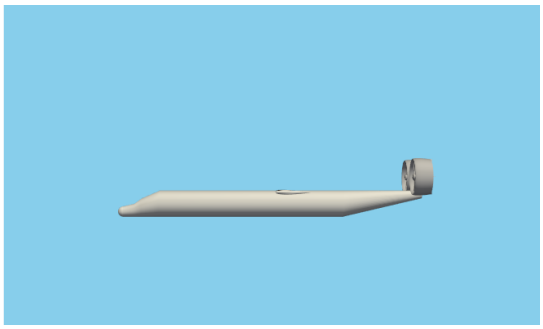

Figure 6.7: Configuration 1 - PE placed at the rear end of the fuselage.

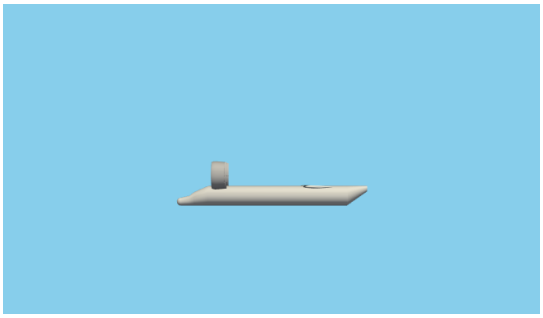

Figure 6.8: Configuration 2 - PE placed at the front of the fuselage just after the cockpit.

6.2.1. Center of Gravity

The longitudinal and vertical center of gravity is evaluated for different loading conditions of the aircraft. These values are compared with similar loading conditions of the ATR aircraft. The lateral center of gravity is assumed to be on the center line of the aircraft, as design changes have been made symmetrically over the y-axis.

Longitudinal Center of Gravity

The center of gravity in the x-direction for DUUC in configurations 1 and 2 is given in Table 6.5 where the values are compared with the ATR. The table indicates that the DUUC with the PE at the rear of the aircraft exhibits a large aft center of gravity, as expected. Configuration 2 has a better alignment of the center of gravity with respect to the ATR aircraft. However, the center of gravity excursion is still larger than that of the conventional aircraft.

When configuration 1 is loaded with fuel and payload, a forward shift in center of gravity is experienced of 5.9%. The center of gravity of the configuration is pushed forward by 3.8% in minimum fuel conditions, which is dangerously close compared to the baseline. With the center of gravity of the wing group reaching 0.623 for the DUUC with rear PE configuration, compared to 0.443 for the ATR, it implies that approximately 40% extra downforce is required for the DUUC to create a stable condition. This will come at the cost of additional trim drag and will decrease the aerodynamic performance of the DUUC.

The maximum variation in center of gravity of the ATR aircraft is 0.6% which shows the stability of the aircraft. When this is compared to 5.9% and 3.9% of the DUUC, this highlights its sensitivity to loading conditions.

The large deviations in center of gravity have some implications on the loading sequence of passengers and payload to ensure that the aircraft does not tip to its tail. Operational constraints can be applied,

or an additional tail wheel can be installed that can be deployed during ground operations. Although this is not beneficial, it can prevent operational constraints.

Table 6.5: Longitudinal center of gravity results for both DUUC configurations compared to the ATR for different loading conditions.

Aircraft	Payload condition	Fuel condition	x_w/x_{fus}	$x_{cg_{FG}}/x_{fus}$	$x_{cg_{WG}}/x_{fus}$	x_{cg}/x_{fus}
ATR72-600	No	No	0.417	0.449	0.431	0.428
	Full	Max	0.417	0.449	0.443	0.446
	Full	Min	0.417	0.449	0.435	0.445
	No	Max	0.417	0.448	0.443	0.445
	No	Min	0.417	0.448	0.435	0.442
DUUC config. 1	No	No	0.574	0.570	0.623	0.588
	Full	Max	0.574	0.513	0.622	0.554
	Full	Min	0.574	0.513	0.623	0.538
	No	Max	0.574	0.570	0.622	0.597
	No	Min	0.574	0.570	0.623	0.589
DUUC config. 2	No	No	0.809	0.385	0.774	0.398
	Full	Max	0.809	0.412	0.776	0.429
	Full	Min	0.809	0.412	0.777	0.421
	No	Max	0.809	0.385	0.776	0.413
	No	Min	0.809	0.385	0.777	0.399

Vertical Center of Gravity

The vertical center of gravity is compared for the ATR and the DUUC. The center of gravity of all components except for the empennage are constant in center of gravity between the ATR and DUUC. The vertical center of gravity contributions of all components for the ATR and DUUC V0.1 in OEM are given in Table 6.6 and Table 6.7 respectively. The center of gravity is shown in Figure 6.9. The height of the fuselage is illustrated with a black dashed line, while the aerodynamic center of the wing is illustrated in red. A reduction of 0.41 m is observed which is equal to 14 % of the fuselage height. The main issue with this reduction is that the moment arm is decreased for the stabilizing contribution of the wing to the stability of the pendulum.

The addition of only fuel will make both aircraft less stable in terms of pendulum stability as the vertical center of gravity moves up. However, the effect on the DUUC is smaller, since the center of gravity in the OEM condition is already closer to the center of gravity of the fuel. When fuel and passengers are added to the aircraft, the vertical center of gravity is calculated again. The difference between the ATR and the DUUC decreases; this has to do with the low position in the vertical center of gravity of the payload. However, the difference is still 8% of the fuselage height.

Table 6.6: Vertical center position and mass of each component in ATR.

Component	z_{cg} [m]	mass [kg]	$z_{cg} \cdot mass$
Fuselage	1.44	3370	4853
Systems	1.44	3113	4482
Wing	2.58	3309	8537
Landing Gear	0.14	1018	142
Engines	2.44	1989	4853
Hor. tail	7.30	146	1065
Vert. tail	5.09	178	906
Total		13123	24841
		$z_{cg_{OE}}$	1.89

Table 6.7: Vertical center position and mass of each component in DUUC.

Component	z_{cg} [m]	mass [kg]	$z_{cg} \cdot mass$
Fuselage	1.44	3370	4853
Systems	1.44	3113	3611
Wing	2.58	2875	7417
Landing Gear	0.14	1018	142
PE	4.57	3359	15350
Total		13735	31373
		$z_{cg_{OE}}$	2.30

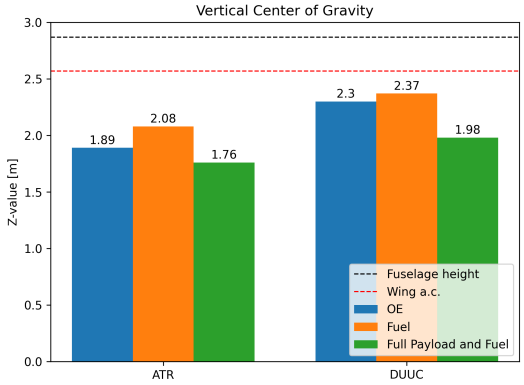

Figure 6.9: Vertical center of gravity comparison between the ATR72-600 and the DUUC with OEM and full payload and fuel configuration.

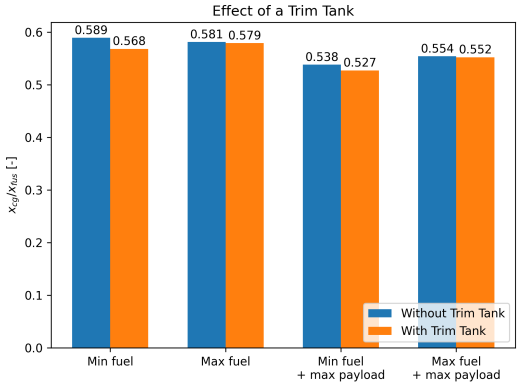

Figure 6.10: Impact of the use of a trim tank on the horizontal center of gravity. The trim tank is placed at 19 % of the fuselage on the DUUC configuration 1.

Assuming that the DUUC and ATR wings have the same performance in cruise conditions, the reduction in pendulum stability can be calculated. The reduction of the pendulum stability contribution of the fuselage in OEM is approximately 55% and is 22% under full payload and fuel conditions. The pendulum stability takes up about 5% of the total value of C_{M_α}, the reduction is not significant, but relaxes the center of gravity constraints a bit.

Trim Tank

The challenge with the center-of-gravity excursion for the DUUC could potentially be solved by using a trim tank. To compensate for the large tail load of the PE, a trim tank is placed in the front of the aircraft just after the partitioning bulkhead of the cockpit. The trim tank can hold 10% of the maximum fuel equal to 500 kg. The dimensions of the trim tank are calculated so that it fits below the floor.

The results of the use of the trim tank and the effect on the center of gravity are depicted in Figure 6.10. The effect of the trim tank is the largest in minimum fuel condition with zero payload. The center of gravity shifts forward with 2% of the fuselage length. When the maximum payload is added, the shift reduces to 1%. The effect when the aircraft is loaded with maximum fuel is negligible. The forward center of gravity shift would reduce the additional trim drag by 3% for the minimum fuel case and 1% when payload is added. The gains of the trim tank are small but it is worth considering this in the final design.

Another option could be to add a larger trim tank in the aircraft, which can further reduce trim drag under full fuel conditions. This would imply a weight penalty for additional systems that transport the fuel from the trim tanks towards the PE. However, since the systems already have to be present when installing a trim tank, the size depends only on the available space underneath the floor of the cabin. A reduction in trim drag of 9.5% is achieved when a trim tank is installed that can hold 1000 kg of fuel. This size pushes the limits in the available space beneath the cabin. The design is still conceptual, as the available space underneath the floor is not fully known.

6.2.2. Horizontal Tail Sizing

The horizontal tail area that is required versus the project surface area available for both configurations is given in Table 6.8. Both configurations meet the required horizontal tail surface that would be necessary for the stability and control requirement. The DUUC configuration 2 is placed slightly closer to the fuselage and hence the pylon contribution to the lifting surface is reduced. The size of the duct also influences the available surface for the vertical tail and hence also these requirements need to be satisfied simultaneously.

Table 6.8: Horizontal tail area required to satisfy the control and stability requirements compared to the ATR empennage.

Component	**DUUC configuration 1**		**DUUC configuration 2**		**ATR72-600**
	Required	Available	Required	Available	Required/Available
Hor. tail	12.81		13.79		11.70
Duct		11.96		12.96	
Pylon		1.73		1.00	
Total $[m^2]$		**13.69**		**13.96**	**11.70**

In order to get both configurations stable, the installation angle has to be adjusted. This installation angle comes with a penalty of installation drag or trim drag. Table 6.9 gives the installation angle per configuration, including a comparison of the drag increase due to the installation angle.

Table 6.9: Installation angle of the horizontal tail of the ATR and the PE for configuration 1 and 2.

Parameter	**DUUC configuration 1**	**DUUC configuration 2**	**ATR72-600**
i_{ht} [deg]	-3.5	0	-1.5
$C_{D_{trim}}$ [-]	0.0261	0.0183	0.0011
l_{PE} , l_{ht} [m]	9.50	6.39	13.82

6.2.3. Vertical Tail Sizing

The required and available respective vertical tail surface area is demonstrated in Table 6.10. The tail lever arm of configuration 2 is significantly smaller than the lever arm for configuration 1 and to ensure that the requirements can be met, the center of thrust application had to be moved closer to the fuselage. This is the reason that the pylon of configuration 2 has been made smaller compared to one with the PE at the rear.

Table 6.10: Vertical tail area required to satisfy the control and stability requirements compared to the ATR empennage.

Component	**DUUC configuration 1**		**DUUC configuration 2**		**ATR72-600**
	Required	Available	Required	Available	Required/Available
Vert. tail	11.56		12.85		14.9
Duct		11.96		12.96	
Pylon		0		0	
Total $[m^2]$		**11.96**		**12.96**	**14.9**

When the results are examined, configuration 1 requires a lower surface in vertical tail area. This has to do with the fact that the PE is closer to the center line of the aircraft due to the tailoring of the tail. This results in a lower necessary restoring moment in a OEI condition. Furthermore, the rudder area of both configurations are not incorporated the in the available area. The rudders are currently placed at 80% of the duct chord. This implies that roughly 25% of the rudder surface are pointing out of the

PE and hence that area would add some additional available surface area. Thus, both design satisfy the requirements for vertical tail area.

6.2.4. Tail Volume Coefficient

With the tail surface areas determined in the previous sections, the tail volume coefficients can be calculated and compared with the allowable tail volume coefficients from the literature. The horizontal and vertical tail volume coefficients for both DUUC configurations are illustrated in Figure 6.11 and Figure 6.12, respectively. It must be noted that the definition of the tail lever arm changes definition when the empennage is placed in front of the center of gravity. Thus the lever arm will always be positive.

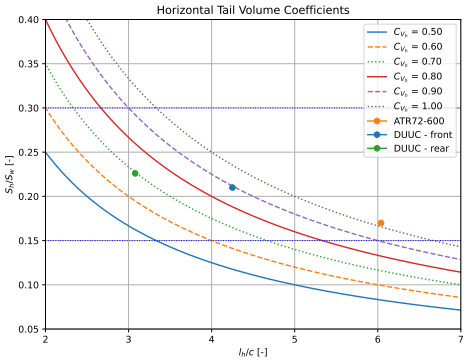

Figure 6.11: Horizontal tail volume coefficient of the DUUC within literature limits.

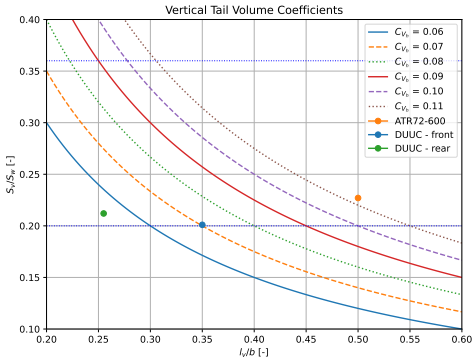

Figure 6.12: Vertical tail volume coefficient of the DUUC within literature limits.

Both configurations have smaller tail lever arm compared to the conventional empennage of the ATR. This has to do with the aft center of gravity. The smaller tail arm for DUUC in configuration also has as in implication that it needs a larger area ratio to generate sufficient force for stability. DUUC configuration 2 does fall beyond vertical tail volume coefficients that are common for transport aircraft. The vertical tail volume coefficient for DUUC configuration 1 will be 0.07 while configuration will have 0.05 for C_{VT}.

The horizontal tail volume coefficients express the same behavior, but are still within the common design ranges for transport aircraft. The horizontal tail volume coefficients will be 0.90 and 0.70 for configurations 1 and 2, respectively. The tail volume coefficients are far from the values from similar sized aircraft. Complementing this with the fact that there are no other statistical data available for aircraft employing a Propulsive Empennage would make it very difficult to use the tail volume concept in the preliminary sizing process of an aircraft with a PE.

6.2.5. Aerodynamic Performance

The aerodynamic performance of the aircraft configurations analyzed is shown in Figure 6.13. The cruise lift coefficient for each configuration is listed in Table 6.11 where also the weight of the aircraft in cruise is given. DUUC configuration has a shorter fuselage and hence the weight of this aircraft is also lower.

From Figure 6.13 it becomes obvious that the aerodynamic performance of both DUUC configurations do not outperform the ATR aircraft. The configuration with the PE at the front of the aircraft performs better than the configuration with the empennage at the back. This has to do with the fact that the empennage at the front has a lift contribution that is positive instead of negative. Additionally, the installation angle is smaller and hence the installation drag or trim drag is lower.

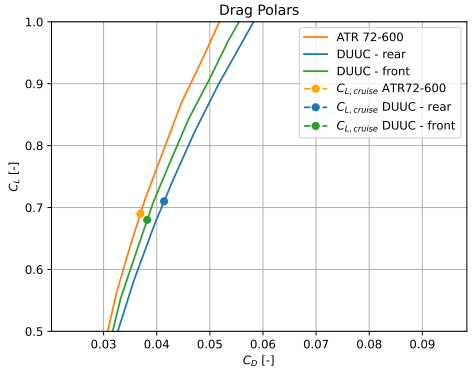

Figure 6.13: Drag polar comparison between different configurations.

Table 6.11: Cruise lift coefficient and weight for each configuration at an altitude of 7000 meter at 128 m/s.

Configuration	$C_{L_{cruise}}$ [-]	Mass [kg]
ATR72-600	0.69	20623
DUUC config. 1	0.71	21235
DUUC config. 2	0.68	20550

Fuel Fraction

The fuel fraction for the ATR has been extracted from the work from van den Dungen [16] who has used the Initiator to calculate this value. The fuel fraction is defined as the fuel mass divided by the maximum take-off mass. The results of the comparison is found in Table 6.12. Here can be observed that configuration 1 has a 5% increase in fuel fraction while configuration 2 performs closer to the ATR. This has to do with the fact that configuration 2 is slightly lighter but does use a bit more fuel due to an increased drag in cruise.

Table 6.12: Fuel fraction results with respect to the ATR72.

Configuration	Fuel fraction	Deviation from baseline [%]
ATR72-600	0.0695	-
DUUC - config. 1	0.0728	+ 4.74 %
DUUC - config. 2	0.0711	+ 2.30 %

Propulsive Efficiency

The propulsive efficiency of the ATR is found to be 0.79 with the definition of Equation 3.3. This efficiency is also evaluated in cruise phase for both DUUC configurations and the results are listed in Table 6.13. The results show a maximum deviation of 10%. This has to do with the additional drag of the aircraft. Configuration 2 performs slightly better as it has a bit less drag. It must be noted that the thrust benefit the ducted propulsors have is included, and hence annulled by the additional drag of the aircraft.

Table 6.13: Propulsive Efficiency comparison between the ATR and DUUC configurations at V=128 m/s.

Configuration	$\eta_{propulsive}$	Deviation from baseline [%]
ATR72-600	0.79	
DUUC - config. 1	0.71	- 10.1 %
DUUC - config. 2	0.73	- 7.4 %

6.2.6. Stability Derivatives

The stability derivatives obtained for the DUUC are given in Table 6.14 where the PE is placed at the rear and front of the aircraft. The DUUC configurations are compared with the IAFM values for the reference aircraft.

Table 6.14: Stability derivatives for the two configurations of the DUUC compared with the derivatives from the ATR.

Derivative	Unit	ATR72-600	DUUC - config. 1	DUUC - config. 2
C_{L_α}	$[rad^{-1}]$	5.7331	6.1197	6.4308
C_{M_α}	$[rad^{-1}]$	-1.667	-2.0822	-0.3124
C_{Y_β}	$[rad^{-1}]$	-0.7286	-0.9173	-0.8182
C_{N_β}	$[rad^{-1}]$	0.1441	0.3222	-0.2091

The lift curve slope of both configurations is slightly higher compared to the traditional empennage. This has to do with a higher value of the tail efficiency factor η_h as this does not have the slipstream effect of the propellers that affects the inflow of the horizontal tail. For configuration 2, where the PE is in front of the wing, the downwash factor is zero, which leads to a higher value. Additionally, the DUUC aircraft has a clean wing configuration leading to an increase value of C_{L_α}.

The pitching moment derivative with respect to alpha for the DUUC with the rear PE is more negative compared to the ATR as the tail is more effective, as explained in the previous paragraph. The C_{M_α} value for the second configuration is still negative but significantly lower compared to the baseline. A comparison of the component distributions is illustrated in Figure 6.14. As the value C_{M_0} is an offset, it has been decided to keep it zero for this analysis as it is not trivial to calculate this value for a wing, let alone for the innovative PE. Since the fuselage in configuration 2 is smaller, the destabilizing contribution as observed in Figure 6.14 decreases.

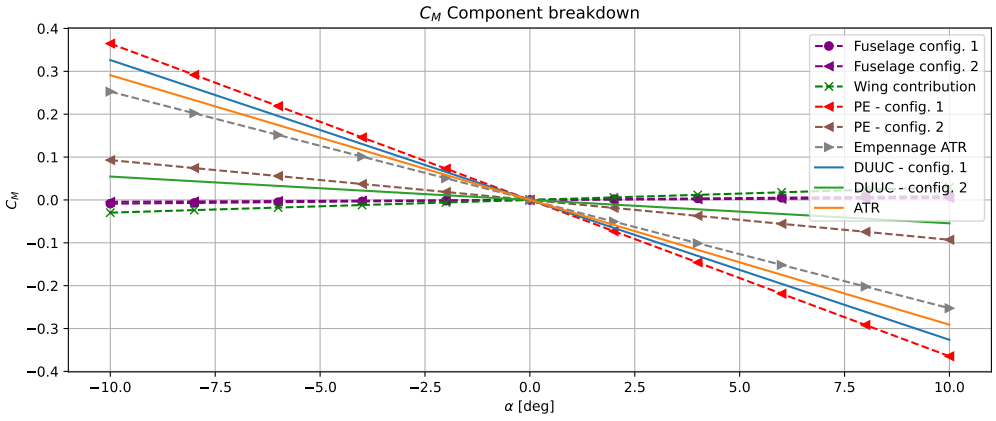

Figure 6.14: C_{M_α} contribution of aircraft components and aircraft sum comparison.

Another significant thing to observe from Table 6.14 is that the sign of the weathercock stability changes sign when the PE is placed at the front of the aircraft. This causes the aircraft not to be directionally stable by configuration. This implies that additional rudder deflection would be necessary to deal with sideslip and hence additional drag.

6.2.7. Control Derivatives

The control derivatives for both DUUC configurations 1 and 2 are given in Table 6.15 and compared to the values found for the ATR. For each DUUC configuration, the two control vane configurations are analyzed for which the results can also be found in Table 6.15. When the DUUC is in configuration 2, the control deflections have changed sign, in order to generate the same response since the empennage is now in front of the cg of the aircraft.

Table 6.15: Control derivatives for the two configurations of the DUUC and for two different control vane configurations compared with the derivatives from the ATR.

Derivative	**Unit**	**ATR72-600**	**DUUC - config. 1**		**DUUC - config. 2**	
			X-configuration	Duct-edge	X-configuration	Duct-edge
$C_{L_{\delta_e}}$	$[rad^{-1}]$	0.3048	0.1070	0.3960	0.1070	0.3960
$C_{M_{\delta_e}}$	$[rad^{-1}]$	-1.6837	-0.4549	-1.6835	-0.3112	-1.1519
$C_{Y_{\delta_r}}$	$[rad^{-1}]$	-0.6310	-0.1070	-0.3960	-0.1070	-0.3960
$C_{N_{\delta_r}}$	$[rad^{-1}]$	-0.2921	-0.4549	-1.6835	-0.3112	-1.1519

From the values listed in Table 6.15 with respect to the elevator deflection, it can be observed that the X-configuration control vanes have a very low response. This has as a consequence that a larger deflection is required to obtain the required result and hence would generate more drag. When the control vanes are moved to the duct edge, the control regime is very close to the baseline of the ATR.

The rudder control authority is for the DUUC duct's edge configuration show a very large value compared to the baseline of the ATR.

Reduced Control Vane Load

As discussed in section 4.5, the force generated by the control vanes has to be corrected for the inflow direction in the propeller swirl when the control vanes are in X-configuration. To determine the effect of this correction, a test case is studied in which the inflow angle of the control vanes is equal to 5 degrees over a range of elevator deflections. Figure 6.15 shows that if the model were not corrected, the lift curve would look like the blue line. With an angle correction of $-2 \cdot \alpha$ to one of the control vanes, the lift curve is depicted in orange. The difference between the two, shown in red, decreases at larger deflection angles as one of the control vanes enters the nonlinear part of the 2D lift curve generated in XFoil. The lift coefficient per control vane corresponding to each elevator deflection is given in Table 6.16.

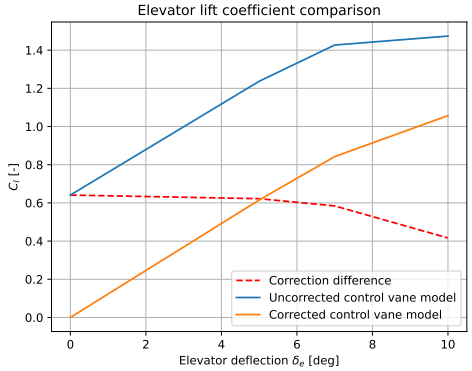

Figure 6.15: Control Vane lift coefficient correction for propeller swirl.

Table 6.16: Elevator lift coefficient per angle of attack over a range of elevator deflection.

α	δ_e	α_{cv1}	α_{cv2}	C_{l-cv1}	C_{l-cv1}	C_{l-eff}
5	0	5	-5	0.6410	-0.6410	0.0000
5	5	10	0	1.2370	0.0000	0.6150
5	7	12	2	1.4267	0.2582	0.8424
5	10	15	5	1.4737	0.6410	1.0573

This reduced load for the elevator is also valid and applied to the rudder inside the DFS. The results of then control vane loads in duct-edge configuration do not change. The corrected model shows a 25% reduction in the response of the control vanes based on a deflection. This has to be taken into consideration when choosing a suitable control vane configuration for the DUUC design.

6.3. Sensitivity Study

A sensitivity study has been performed to determine the effect of certain critical design parameters that have been mentioned before. Changing design parameters has multiple effects on the aircraft design; the most significant effect related to each parameter is shown. The design parameters that are investigated are the PE positioning and duct diameter.

6.3.1. Propulsive Empennage Position

One of the key elements in the design of the DUUC is the positioning of the PE on the aircraft. In the scope, lateral symmetry is assumed and hence all changes that are made will be symmetric. The positioning in x- and y-direction are investigated including their effect. The longitudinal placement of the PE will affect the sizing of the horizontal tail surface and the center of gravity. The lateral positioning affects the restoring moment that the PE should generate in case of an OEI situation.

Longitudinal Position

To investigate the effect of the longitudinal position of the PE on the behavior of the aircraft, it is placed at different locations on the fuselage. The location is normalized with the length of the fuselage. A graphic representation of the positioning of PE on the fuselage is given in Figure 6.16. The range in which the PE is placed on the fuselage is $0.01 < x < 1$.

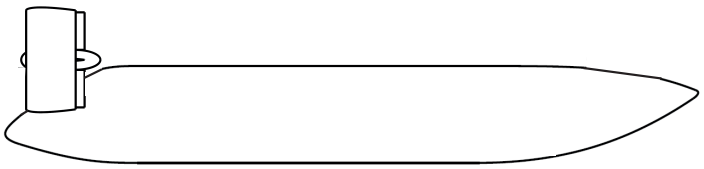

(a) Schematic of the PE position at 0.01 x/x_{fus} on the fuselage.

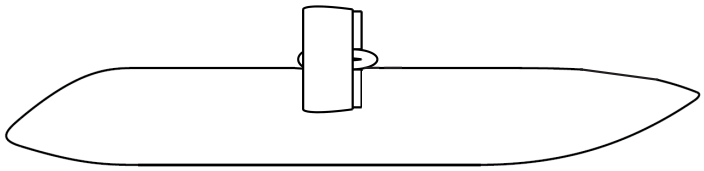

(b) Schematic of the PE position at 0.50 x/x_{fus} on the fuselage.

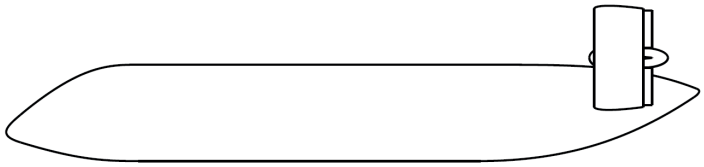

(c) Schematic of the PE position at 1.00 x/x_{fus} on the fuselage.

Figure 6.16: Schematic representation of the PE position change on the fuselage to determine the effect on the center of gravity.

The effect of the loading condition on the center of gravity is illustrated in Figure 6.17. Here, it can be observed that the loading payload on to the aircraft pulls the maximum center of gravity location forward, but also illustrates that the minimum cg value is further aft. There is a point around the point at which both payload lines cross each other, which is at the wing position of this aircraft configuration at which the fuel loading does not matter for the center of gravity.

The loading of fuel in the configuration decreases the steepness of the center of gravity line with respect to the PE position. It also increases the maximum location of the center of gravity, which also shows the extremest value for the cg. This is found with the maximum fuel load without payload in the fuselage.

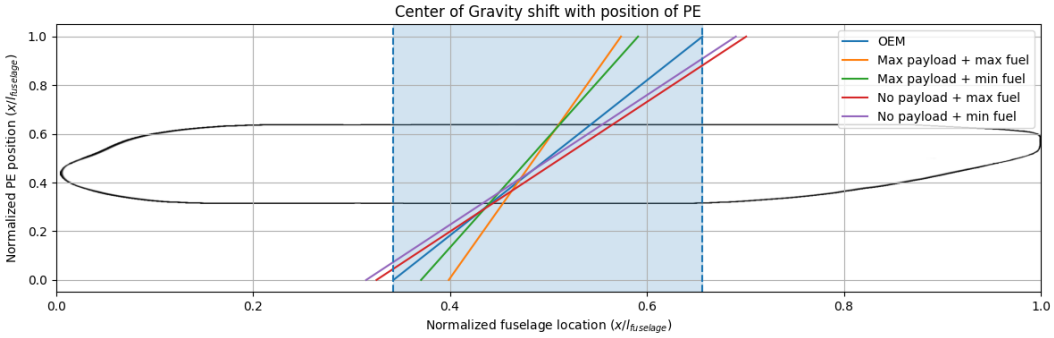

Figure 6.17: Effect of the PE position on the fuselage with respect to the center of gravity in different loading conditions.

When changing the PE position across the fuselage, not only the center of gravity changes but also the tail lever arm. This arm is defined as the length between the center of gravity and the aerodynamic center of the empennage. Figure 6.19 shows the tail lever arm with respect to the position of the PE on the fuselage. Two configurations are examined where the fuselage length of 21 meter corresponds to DUUC configuration 2 and the length of 27 meter to configuration 1 and the ATR baseline.

The center of gravity change with the moving PE has been taken into consideration in this line. The tail lever arm becomes negative when the PE is placed in front of the center of gravity. For stability relations and tail volume coefficient the tail lever arm has a positive value and the absolute value from Figure 6.19 is obtained. It becomes obvious that the rate of change in the tail lever arm is smaller for the smaller fuselage. This can be explained by the fact that a change in location on the smaller fuselage also has a smaller effect, since the arm to the center of gravity is smaller.

With a decreasing or increasing tail lever arm, a different horizontal tail surface is required to stabilize the aircraft. When the tail lever arm is small or zero, the value for required horizontal tail surface becomes infinite. The results of this analysis are given in Figure 6.18.

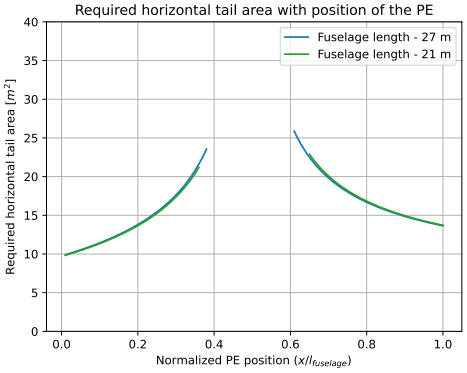

Figure 6.18: Effect of the PE position on the fuselage with respect to required horizontal tail surface.

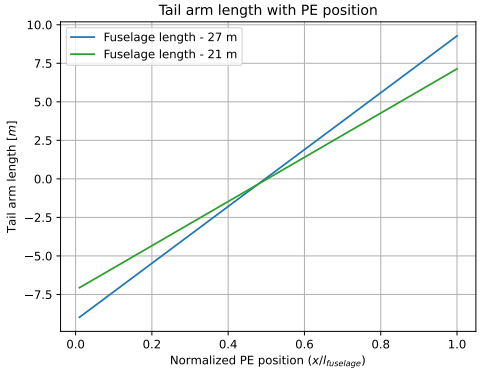

Figure 6.19: Effect of the PE position on the fuselage with respect to the tail lever arm.

In the conceptual design, the size of the PE has yet to be determined. For this reason, the effect of an increase and decrease in weight has been investigated with respect to the position of PE on the fuselage in Figure 6.20. It is apparent that a heaver PE leads to a center of gravity that is further aft when the PE is at the rear end of the fuselage. The slope of the center of gravity change with respect to the fuselage position becomes less steep and enhances the effect of moving the PE. The effect of a change of 1000 kg in the empennage weight changes the position of the center of gravity by 6.5%.

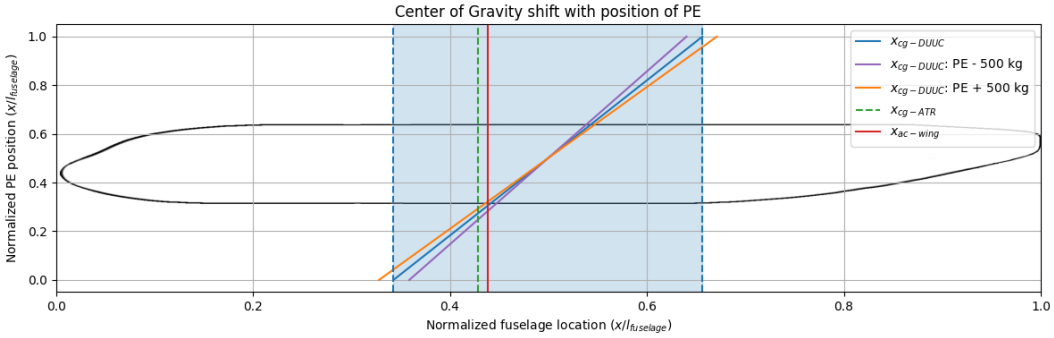

Figure 6.20: Effect of the PE position on the fuselage with respect to the center of gravity with a variation in PE weight.

Lateral Position

The lateral position of the PE on the aircraft can be changed by determining the pylon length or cant angle. The duct diameter has to be kept constant in order to have the same propulsive properties. When the pylon length is increased, the largest implication is the increase in weight and support mass. As the structural moment that these have to undertake becomes larger the structural requirements change the mass.

Figure 6.21 show the weight increase with pylon length for both DUUC configurations. The DUUC configuration is slightly heaver due to the larger duct size which implies a higher weight and steeper increase of weight with pylon length.

Increasing the pylon length changes the location of thrust application and thus the restoring moment when the aircraft has OEI. The drag of the non-working PE is also different due to the increased pylon length but also due to the application line. The restoring moment that is required to counteract the OEI condition increases linearly with pylon length as can be concluded from Figure 6.22.

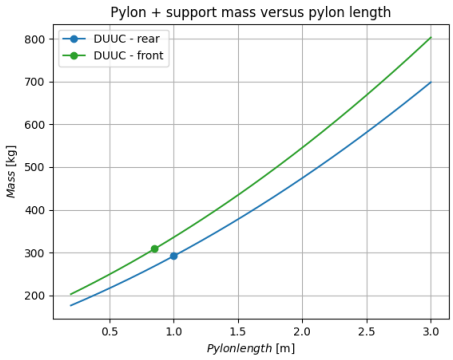

Figure 6.21: Pylon and support mass over a range of pylon length for the DUUC.

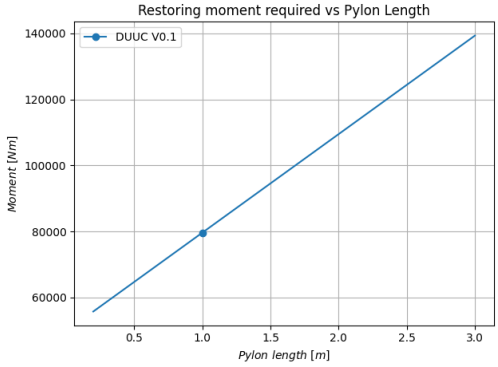

Figure 6.22: Required restoring moment with respect to pylon length for the DUUC.

Changing the cant angle also changes the bending moment the pylon and support have to undertake. As the component buckling component inside the beams decreases with a decrease in cant angle, the bending moment increases and hence the weight also increases. The results of this sensitivity parameter is shown in Figure 6.23.

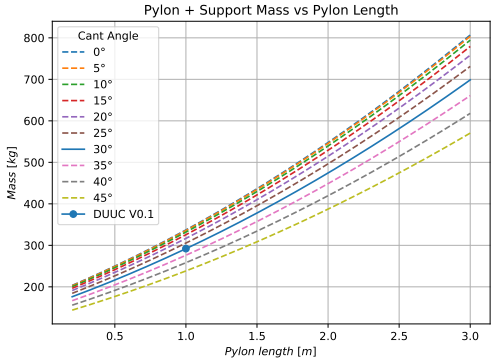

Figure 6.23: Effect of cant angle on the pylon and support mass over a range of pylon length for the DUUC.

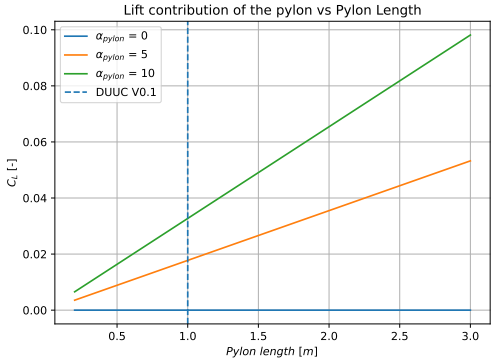

Figure 6.24: Effect of pylon length on aircraft lift over a range of pylon length for the DUUC with a cant angle of 30 degrees.

When the pylon length is increased, the lifting surface becomes larger and hence the lift contribution on aircraft level also increases. Figure 6.24 demonstrates the lift contribution of the pylon for a range of angles of attack of the pylon versus the pylon length. From Figure 6.24 it becomes clear that only at large angles of attack the contribution of the pylon becomes more significant with a significantly larger pylon.

6.3.2. Duct Diameter

The duct diameter is directly related to the performance of the PE. As the model is validated for a certain aspect ratios, it has been decided to keep the aspect ratio of the duct constant at 2.0 during the sensitivity analysis. When the duct diameter is modified, a few other parameters that are linked, will also change. The chord of the duct, span of the support, blade radius and control vanes automatically change size when the duct diameter is adjusted.

In terms of mass, the duct and the support have the largest change when the diameter of the duct is changed. This is done under the assumption that the engine in the PE stays the same and that the nacelle does not change size. This assumption is not fully valid when the duct is very small, but as the engine mass is taken from reference, it is difficult to scale with the duct diameter, and hence it has been decided to keep it constant. Figure 6.25 illustrates the increase in weight of the duct and support with increasing duct diameter. The support weight increases because of its increase in size, but also due to the increase in bending moment that is caused by the increased duct weight.

When this increase in weight is analyzed on the complete PE weight, the duct and support weight become notably larger towards the larger duct diameters. This is of course to be expected as the large contributors, the engine and nacelle, have been set constant for this analysis.

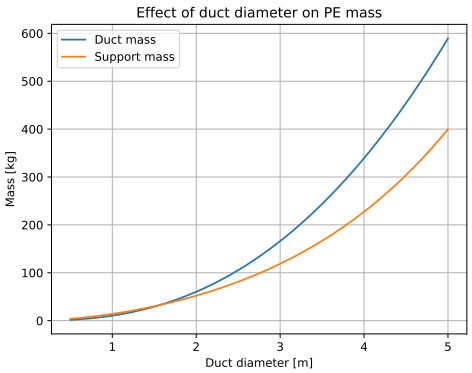

Figure 6.25: Relation between duct diameter and mass of the duct and support.

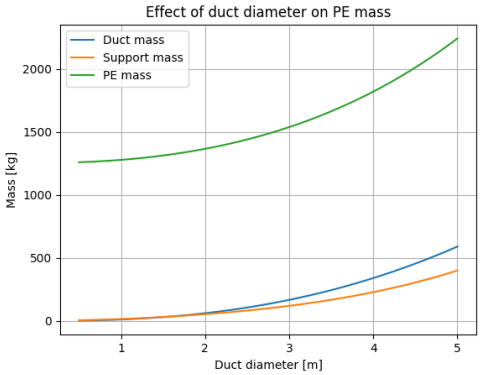

Figure 6.26: Duct mass with respect to PE mass over a range of duct diameter.

The expansion ratio, which merely determines the additional thrust that is delivered due to the application of a duct around the propeller, depends on the airfoil profile used in the duct. When using a symmetric profile, the expansion ratio is determined by the thickness change between the propeller plane and the exit. Figure 6.27 illustrates the relationship of the expansion ratio with respect to the thrust ratio between a ducted and open rotor propeller. It can be concluded that having a larger expansion ratio delivers a higher portion of additional thrust. Potential design changes from this could be the use of cambered airfoil profiles. This would increase the expansion ratio. Secondly, a slight positive installation angle of the airfoil profiles of the duct would also lead to the same result. Note that the full should still fully expand to ambient pressure to ensure that the relationship in Figure 6.27 holds.

The effect on thrust with respect to the duct diameter is illustrated in Figure 6.28. It can be observed that the thrust quadratically relates to the duct diameter. This is also observed in the definition of the BEM model. Different expansion ratios are illustrated in this figure. In this case the open rotor thrust with the smallest duct diameter generates 250 N of thrust.

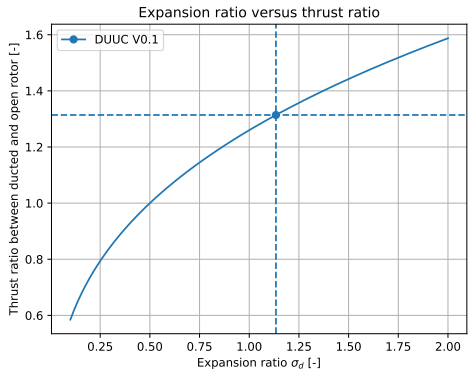

Figure 6.27: Relation between expansion ratio and thrust of the PE compared to open rotor.

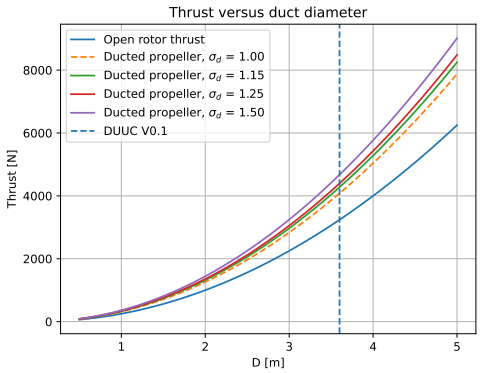

Figure 6.28: Relation between duct diameter and PE thrust.

6.4. DUUC V0.9

The DUUC V0.9 is an aircraft configuration that has been found to be the best in the analysis of the feasibility of the DUUC. A trade-off is made between aerodynamic and flight mechanics performance leading to this design. The aircraft is illustrated in Figure 6.29. The aircraft information is provided in Table 6.17.

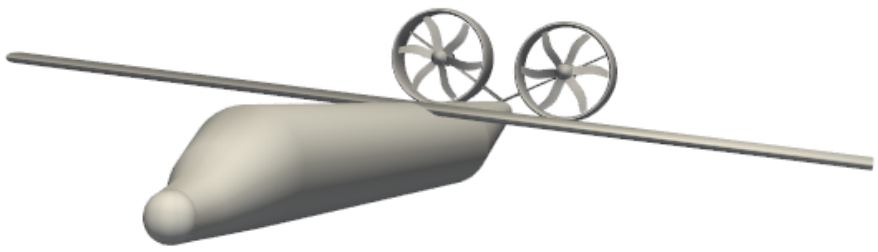

Figure 6.29: DUUC V0.9 aircraft configuration.

Table 6.17: DUUC V0.9 properties found by the prediction model.

Parameter	Value	Unit
OEM	13735	$[kg]$
m_{PE}	3359	$[kg]$
l_{fus}	27	$[m]$
S_w	61.4	$[m^2]$
x_{PE}	24.8	$[m]$
C_L	0.7091	[-]
C_D	0.0415	[-]
L/D	17.08	[-]

The V0.9 design for the DFS is depicted in Figure 6.30. The control vane configuration of the DUUC V0.1 should be changed to the duct edge configuration as shown in Figure 6.31. The improvement in control regime, even without detailed analysis, predicts enough improvement with respect to the X-configuration control vanes. Hence, it has been decided to implement this configuration on the DUUC V0.9. It must be noted that the illustration in Figure 6.31 is still conceptual as the detailed design of the control vanes on the duct edge is beyond the scope of this assignment.

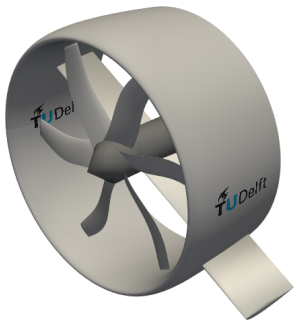

Figure 6.30: DFS for the DUUC V0.9.

Figure 6.31: Conceptual illustration of the proposed control vane configuration used in the DUUC V0.9.

7

Conclusions and Recommendations

This chapter closes the research on the feasibility of an aircraft employing a PE and the DUUC aircraft concept. Conclusions and answers to research questions are given in section 7.1 and recommendations for future work are provided in section 7.2.

7.1. Conclusions

The research in this thesis was set out to investigate the feasibility of the Delft University Unconventional Configuration aircraft, which integrates the propulsion system into the empennage. The concept of synergizing the two systems shows potential combined with other benefits such as a clean wing and potential noise reduction in the cabin and surroundings. Earlier studies have shown that the performance of the DUUC was not favorable compared to that of other aircraft due to the increase in weight and the excursions to the center of gravity. However, these studies were not conclusive, and therefore this study has been done to reevaluate the studies that have been done, refine where possible, and conclude on the feasibility of the concept DUUC.

The DUUC is analyzed by means of empirical relations evaluating the aerodynamics and flight dynamics behavior of the aircraft in the Integrated Aircraft Feasibility Model. This model is validated with experimental data and compared with the reference aircraft, the ATR72-600. The positioning of the PE on the fuselage has been evaluated in two main configurations, where a conventional position has been compared to a canard version of the PE.

When the previous methodology for the analysis of the DUUC is compared with the IAFM in this thesis, changes in the aerodynamic and flight mechanics model are found. A correction factor has been applied that takes into account the flow change around the duct into consideration when the control vanes are deflected. This correction factor for the effective inflow angle of the duct is very small and will show negligible results. Secondly, the aerodynamic model of the nacelle has been updated. It was assumed that the nacelle did not produce any lift, this has been proven wrong, and a model has been implemented that determines the aerodynamic coefficients based on a slender inclined body of revolution. The coefficients that result from this model are small but contribute to the overall forces and hence should be taken into account.

The inflow angle of the support and control vanes was determined by means of the propeller slip in earlier studies. This model has been improved to have velocity vectors that take into account the axial velocity caused by the propeller. The radial distribution of the axial velocity on the propeller blade was averaged as the duct reduces the tip losses on the blade. Due to the propeller swirl, the control vanes in the x-configuration show a reduced load due to the negative inflow angle on one of the control vanes. This reduces the generated forces by 25%. This applied correction improves the control vane load model that has previously been used.

Up to now, only the x-configuration of the control vanes had been studied, but an alternative configuration, where the control vanes are on the edge of the duct, had been recommended. The control

vane effectiveness has been determined by means of an AVL analogy and the duct edge controls demonstrate three times the effectiveness compared to the x-configuration control vanes. Finally, an empirical method for determining the thrust of the duct has been implemented that calculates the thrust production on the expansion ratio of the duct.

In the flight mechanics model, the mass prediction of the duct, pylon and support have been updated. Where previously the duct's mass was dependent on an empirical method of nacelle mass estimation, this has been changed to the mass prediction of a horizontal stabilizer to allow the structural requirements to be evaluated in the same way. The pylon and support mass are not evaluated by means of a percentage of the carried weight but are not sized by means of the bending moment generated by the aerodynamic and weight load. This leads to a mass prediction that is more accurate than the percentual method and approaches the detailed sizing that has been done by an FEM analysis in the past.

The pendulum stability, which is caused by drag components with respect to the vertical center of gravity had not been specifically treated in earlier works but has been implemented in the IAFM. With the addition of the Propulsive Empennage, the aircraft shows a reduced stabilizing effect of the fuselage due to the smaller moment arm. The contribution has been shown to be large enough to incorporate into the model as it relaxes some of the stability constraints.

How can the conceptual sizing method of the tail volume coefficient be applied for the Propulsive Empennage of the DUUC?

When using the same definition for the tail volume coefficient but changing the surface area of the horizontal and vertical tail into the projected surface area. The principle of tail volume coefficient can be used in the sizing process. For the horizontal tail surface, the pylon should also be taken into consideration. The tail volume coefficients found for both DUUC configurations are not close to the reference values of the ATR. The vertical tail coefficients found are 0.07 and 0.05 for respective configurations, while the ATR is 0.119. Configurations 1 and 2 have a horizontal tail coefficient of 0.90 and 0.70 where for the ATR 1.05 is found. In combination with the fact that there is no other statistical data available for tail volume coefficients of aircraft employing a Propulsive Empennage will make it hard to use this principle in the conceptual design phase of the DUUC.

What is the propulsive efficiency of an aircraft employing a Propulsive Empennage?

When the propulsive efficiency is defined as the net forward force of the propulsion group and the empennage combined, the ATR has a propulsive efficiency of 0.79. DUUC configurations 1 and 2 have a lower propulsive efficiency, where configuration 1 performs 14% less and configuration 2 slightly better with a reduction of 10%. This has to do with the fact that configuration 2 has slightly less drag. The thrust benefit of the ducted propeller is annulled by the additional drag of the empennage.

How does the performance of the DUUC configuration compare to a conventional turboprop configuration aircraft?

The performance of the DUUC is analyzed with respect to the OEM, the lift-to-drag ratio, and the propulsive efficiency. It can be concluded that the DUUC configurations that have been evaluated do not outperform the ATR. In terms of OEM, configuration 1 shows an increase while configuration 2 is slightly lighter. The decrease in weight for configuration 2 is due to the shorter fuselage length. Where the addition of the duct pylon and support make the PE a heavier system. There is a small weight gain in the wing structure as the DUUC does not have wing mounted engines.

The lift-to-drag ratio in cruise conditions of configuration 2 is closer to ATR and thus performs better than configuration 1. This is caused by the fact that in the canard situation, the PE delivers a positive lift contribution and the trim drag of the empennage is lower. The aerodynamic performance of the ATR performs approximately 6% better. A maximum reduction of 10% in propulsive efficiency is found for the DUUC in a conventional empennage configuration.

What improvements can be made to the Propulsive Empennage to enhance propulsive efficiency?

Changing the position of the empennage on the fuselage affects the installation angle and hence the trim drag of the PE. This can positively influence the propulsive efficiency. Additionally, the Propulsive Empennage has almost double the zero lift drag compared to a conventional empennage. When this could be reduced, the propulsive efficiency would be positively affected. The major contributor to the zero lift drag are the ducts and hence small changes could already have significant influence.

What are alternative positions of the Propulsive Empennage, and how does this affect the performance?

In the analysis of the two configurations of the DUUC, a canard and a conventional tail location were evaluated. Placing the PE in front of the wing is favorable for the center of gravity excursion, but significantly reduces the longitudinal stability of the aircraft. The weathercock stability that is strongly present for the PE changes sign when the PE is placed in front of the wing, which requires active control systems to compensate. As observed in the sensitivity study, moving the PE forwards on the fuselage decreases the center of gravity excursion which contributes to the stability of the aircraft.

What are the implications with respect to the static stability of the aircraft when the Propulsive Empennage is used compared to a conventional turboprop?

As already concluded in previous studies, the center of gravity excursion increases when a propulsive aircraft is used. This is due to the increased tail load. A trim tank could be used to decrease this excursion and contribute to longitudinal stability. The pendulum stability contribution of the wing is reduced when using a PE on the aircraft, this is caused by the decreased moment arm to the vertical center of gravity. When the PE is placed in front of the wing, the aircraft becomes unstable with respect to sideslip.

How can the Propulsive Empennage be optimized to enhance aerodynamic efficiency, performance and stability compared to design iteration V0.1?

A trim tank could be applied directly after the cockpit underneath the cabin floor to reduce the center of gravity excursion of the aircraft. It should be noted that this has only been conceptually evaluated and the feasibility and safety constraints of such a tank have not been determined.

The duct diameter has been optimized together with the pylon length to have the optimum dimensions to allow for sufficient thrust production whilst also meeting the control and stability requirements for the horizontal and vertical stabilizer.

Finally, using the duct edge control vanes compared to the x-configuration applied in DUUC V0.1, improves the control regime which is beneficial considering the large center of gravity excursion when the PE is applied.

What is the feasibility of the DUUC aircraft concept with respect to aerodynamic efficiency, performance and stability characteristics compared to a conventional turboprop aircraft?

Considering all the changes that have been made to the IAFM and the changes that have been applied to the DUUC design. Also, evaluating the results of an alternative position of the Propulsive Empennage. It must be concluded that the DUUC will not outperform a conventional aircraft. The largest issue of the center of gravity excursion causes too much trim drag for the aircraft to improve the efficiency. The addition of a trim tank does not provide sufficient reduction and, with moving the wing position aft, the moment arm reduces too much, and hence the requirements for the tail surfaces are not met without increasing the weight even more.

The synergy of the propulsion and empennage systems has potential because of the additional thrust generated and the highly effective control vanes when placed on the edge of the duct. When placing the ducted fans on the DUUC concept, it must be noted that the thrust benefit is annulled by the

additional trim drag. The increased fuel fraction and lower propulsive efficiency lead to the conclusion that the DUUC aircraft cannot outperform a conventional aircraft.

7.2. Recommendations

Although the DUUC aircraft configuration does not outperform a conventional configuration. There are still some recommendations for future work that can be made.

Control Vane Model

The control vane model for the duct edge configuration has been analytically determined by means of AVL. For the use of ducted propellers that have control vanes, a more detailed study would be required to determine the interaction effects and flow behavior at the exit of the duct.

Placing the control vanes on the duct's edge also implies that the exit of the duct cannot be circular anymore. A square duct has been investigated by Mourao [89] but this does not include a duct that goes from circular to a square shape. Also, the interaction effect at the corner with the leading edges of the control vanes should be investigated.

Lightweight Duct

A study can be done in creating a lightweight duct that is even lighter than the duct that has been proposed by Stavreva [15] in an earlier study. This in combination with the points proposed in section 7.2 could make a combination in which the tail load is reduced in such a way that the center of gravity excursion and trim drag could be optimized, reducing the performance decreases.

Electric propulsion

Using a hybrid electric propulsion system has the disadvantage of adding additional weight to the aircraft. With the already heavier empennage this would increase the OEM even more. The benefit of this system would be that components could have an alternative placement in the fuselage but only at the cost of passenger space in the fuselage. Combined with new range and passenger requirements, the alternative component placement in the propulsion unit shows potential in decreasing the center of gravity excursion.

References

[1] N. van Arnhem. *DUUC Aircraft with the innovative 'Propulsive Empennage' concept*. Sept. 2016.

[2] David W Zingg et al. *A Multifidelity Multidisciplinary Approach To Unconventional Aircraft Development and Assessment with Application to the Strut-Braced-Wing and Hybrid-Wing-Body Configurations*. Tech. rep. ICAS, Sept. 2022.

[3] Stib. "Inktversie Patent LR". In: (Nov. 2016).

[4] I.M. Goldsmith. *A Study to Define the Research and Technology Requirements for Advanced Turbo/propfan transport aircraft*. Tech. rep. 1981.

[5] F. Nicolosi et al. "Performance Evaluation and Doc Estimation of an Innovative Turboprop Configuration". In: *Proceedings of the 2018 Aviation Technology, Integration, and Operations Conference* (2018).

[6] Eurocontrol. *Aircraft Performance Database - VC10*. URL: https://contentzone.eurocontrol.int/aircraftperformance/details.aspx?ICAO=VC10&.

[7] Eurocontrol. *Aircraft Performance Database - MD87*. URL: https://contentzone.eurocontrol.int/aircraftperformance/details.aspx?ICAO=MD87&GroupFilter=4.

[8] Embraer. *CBA 123 Vector*. URL: https://historicalcenter.embraer.com/global/en/cba-123-vector.

[9] Clean Aviation. *Clean Sky 2 Technology Progress - contribution to the environmental performance of the next generation of aircraft*.

[10] VerticalScope. *Embraer-FMA CBA-123 Vector*. URL: https://www.airliners.net/photo/Embraer/Embraer-FMA-CBA-123-Vector-IA-70/1140110.

[11] R. Vos and M.F.M. Hoogreef. *System-level Assessment of Tail-Mounted Propellers for Regional Aircraft*. Tech. rep. ICAS, 2018.

[12] D. Black and C. Rohback. "Shrouded propellers - A comprehensive performance study". In: American Institute of Aeronautics and Astronautics (AIAA), Oct. 1968. DOI: 10.2514/6.1968-994.

[13] V.N. Harinarain. *Aerodynamic Performance Study on a Ducted Propeller System for Propulsion and Control & Stability Applica-tions*. Tech. rep. Delft University of Technology, May 2017. URL: https://repository.tudelft.nl/record/uuid:63a08d3d-722d-4a66-a7ef-37effdace320.

[14] J.H. Dittmar. *NASA Technical Memorandum 100262*. Tech. rep. 1988.

[15] M.N. Stavreva. *Structural Sizing Method for Propulsive Empennage System Weight Estimation of Ducted Propeller Systems that Provide Longitudinal and Lateral Stability*. Tech. rep. Aug. 2020. URL: https://repository.tudelft.nl/record/uuid:01dfe848-7c5d-4d7a-b68f-c2f60bcdb4a3.

[16] N.H.M. Van Den Dungen. *Synthesis of an Aircraft Featuring a Ducted-Fan Propulsive Empennage*. Tech. rep. Delft University of Technology, Apr. 2017. URL: https://repository.tudelft.nl/record/uuid:82986b0c-2b29-462f-8c6f-746236259ea3.

[17] C. Varriale et al. "A Thrust-Elevator Interaction Criterion for Aircraft Optimal Longitudinal Control". In: American Institute of Aeronautics and Astronautics (AIAA), June 2019. DOI: 10.2514/6.2019-3001.

[18] ATR. *ATR72-600 The most fuel efficient regional aircraft*. URL: https://www.atr-aircraft.com/aircraft-services/aircraft-family/atr-72-600/.

[19] J.L. Pereira. *Hover and Wind-Tunnel Testing of Shrouded Rotors for Improved Micro Air Vehicle Design*. Tech. rep. 2008.

[20] K.J.M. Hameeteman. *Unconventional Propulsive Empennage-Future or Fiction? Stability & control analysis and the effect of scaling of the DUUC*. Tech. rep. Delf University of Technology, Oct. 2017. URL: https://repository.tudelft.nl/record/uuid:8a0d0131-6961-4a19-baa5-32fac80d6b5c.

[21] R. van Dijk and M. Baan. *ParaPy - Knowledge Based Engineering Platform*. Delft. URL: https://parapy.nl/.

[22] E. Adib. *Positioning of the Ducted Fan Propulsive Stabiliser*. Tech. rep. Delft University of Technology, Sept. 2021. URL: https://repository.tudelft.nl/record/uuid:948b5315-4742-4ca7-b4e0-1d56c405fafb.

[23] S. Ribner. "The Ring Airfoil in Non Axial flow". In: *Institute of the Aeronautical Sciences* Vol. 14 no. 9 (Sept. 1947), pp. 529–530.

[24] H.S. Fletcher. *Experimental investigation of lift, drag and pitching moment of five annular airfoils*. Tech. rep. NACA, Oct. 1957.

[25] T. Burton et al. *Wind Energy Handbook*. Wiley, May 2011. ISBN: 9780470699751. DOI: 10.1002/9781119992714.

[26] R. Oleson and Howard Patrick. "Small aircraft propeller noise with ducted propeller". In: *4th AIAA/CEAS Aeroacoustics Conference*. Reston, Virigina: American Institute of Aeronautics and Astronautics, June 1998. DOI: 10.2514/6.1998-2284.

[27] E. Obert. *Aerodynamic Design of Transport Aircraft*. Delft University Press, 2009, pp. 2023–2032. URL: http://ebookcentral.proquest.com/lib/delft/detail.action?docID=448784..

[28] M.A. Chao and T.A.N. Zhoaguang. "A Conceptual Analysis of an Aircraft With Rear-Mounted Open Rotor Engines". In: *ICAS2016* (2016).

[29] A. Filippone and Z. Mohamed-Kassim. *Multi-Disciplinary Simulation of Propeller-Turboshaft Aircraft Flight*. Tech. rep. 1184. University of Manchester, 2012, pp. 985–1014.

[30] P. Martin and C. Tung. *Performance and Flowfield Measurements on a 10-inch Ducted Rotor VTOL UAV*. Tech. rep.

[31] H. Cai, Z. Zhang, and S. Deng. "Numerical Prediction of Unsteady Aerodynamics of a Ducted Fan Unmanned Aerial Vehicle in Hovering". In: *Aerospace* 9.6 (June 2022). ISSN: 22264310. DOI: 10.3390/aerospace9060318.

[32] Anita I Abrego. *Performance Study of a Ducted Fan System*. Tech. rep. California: NASA Ames Research Center, 2002.

[33] Y. Song and P. Shan. *Research on Propeller Characteristics of Tip Induced Loss*. Tech. rep. 2017.

[34] D. Yongle, S. Baowei, and W. Peng. "Numerical investigation of tip clearance effects on the performance of ducted propeller". In: *International Journal of Naval Architecture and Ocean Engineering* 7.5 (Sept. 2015), pp. 795–804. ISSN: 20926790. DOI: 10.1515/ijnaoe-2015-0056.

[35] X. An et al. "Tip clearance influence on hydrodynamic performance and pressure fluctuation of a composite ducted propeller using a two-way FSI method". In: *Ocean Engineering* 282 (Aug. 2023). ISSN: 00298018. DOI: 10.1016/j.oceaneng.2023.114698.

[36] R.J. Goudswaard, D. Ragni, and W.J. Baars. "Effects of the rotor tip gap on the aerodynamic and aeroacoustic performance of a ducted rotor in hover". In: *Aerospace Science and Technology* 155 (Dec. 2024). ISSN: 12709638. DOI: 10.1016/j.ast.2024.109734.

[37] A. Smærup Olsen. "Energy coefficients for a propeller series". In: *Ocean Engineering* 31.3-4 (2004), pp. 401–416. ISSN: 00298018. DOI: 10.1016/j.oceaneng.2003.06.002.

[38] J. Gazzaniga and G. Rose. "Wind tunnel performance results of swirl recovery vanes as tested with an advanced high speed propeller". In: *28th Joint Propulsion Conference and Exhibit*. Reston, Virigina: American Institute of Aeronautics and Astronautics, July 1992. DOI: 10.2514/6.1992-3770.

[39] C.J. Miller. *Euler Analysis of a Swirl Recovery Vane Design for Use With an Advanced Single-Rotation Propfan*. Tech. rep. NASA, 1988.

[40] Y. Wang et al. “Design and numerical investigation of swirl recovery vanes for the Fokker 29 propeller”. In: *Chinese Journal of Aeronautics* 27.5 (2014), pp. 1128–1136. ISSN: 10009361. DOI: 10.1016/j.cja.2014.03.009.

[41] T. Sinnige et al. “The effects of swirl recovery vanes on single - Rotation propeller aerodynamics and aeroacoustics”. In: *21st AIAA/CEAS Aeroacoustics Conference*. American Institute of Aeronautics and Astronautics Inc, AIAA, 2016. ISBN: 9781624103674. DOI: 10.2514/6.2015-2358.

[42] Z. Li et al. “Aerodynamic performance and interaction effects of swirl recovery vanes for ducted propeller”. In: *First Aerospace Frontiers Conference (AFC 2024)*. Ed. by Han Zhang. Vol. 13218. SPIE, 2024, 132181N. DOI: 10.1117/12.3032629. URL: https://doi.org/10.1117/12.3032629.

[43] L. Prandtl. *Induced Drag of Multiplanes*. Feb. 1924.

[44] A. Maqsood and T. Hiong Go. “Aerodynamic estimation of annular wings based on leading-edge suction analogy”. In: *AIAA Journal* 51.2 (Feb. 2013), pp. 529–534. ISSN: 00011452. DOI: 10.2514/1.J051914.

[45] E.C. Polhamus. *A Concept of the Vortex Lift of Sharp-Edge Delta Wings Based on a Leading-Edge Suction Analogy*. Tech. rep. NASA, Dec. 1966.

[46] John E. Lamar. *Extension of Leading-Edge-Suction Analogy to Wings with Separated Flow Around the Side Edges at Subsonic Speeds*. Tech. rep. Washington: NASA, Oct. 1974.

[47] A. A. Kanoria and M. Damodaran. “Computational prediction of annular wing aerodynamic characteristics”. In: *Journal of Aircraft*. Vol. 54. 2. American Institute of Aeronautics and Astronautics Inc., 2017, pp. 815–824. DOI: 10.2514/1.C033876.

[48] Matthew Anderson et al. *Propeller Location Optimisation for Annular Wing Design*. Tech. rep. The University of Sydney, 2013, pp. 17–20.

[49] M.J. Werle. “Aerodynamic loads and moments on axisymmetric ring-wing ducts”. In: *AIAA Journal* 52.10 (Oct. 2014), pp. 2359–2363. ISSN: 00011452. DOI: 10.2514/1.J053116.

[50] E. Torenbeek. *Synthesis of subsonic airplane design*. Kluwer, 1996. ISBN: 9024727243.

[51] D.P. Raymer. “Aircraft Design A Conceptual Approach”. In: *AIAA* (1992).

[52] L.W. Traub. “Experimental investigation of annular wing aerodynamics”. In: *Journal of Aircraft* 46.3 (2009), pp. 988–996. ISSN: 15333868. DOI: 10.2514/1.39822.

[53] L.W. Traub. “Preliminary investigation of the effects of stagger on an annular wing”. In: *Journal of Aircraft* 54.6 (2017), pp. 2386–2392. ISSN: 15333868. DOI: 10.2514/1.C034310.

[54] T. Wan and H.E. Saravia. “Aerodynamic Calculation of an Elliptic Ring Wing”. In: American Institute of Aeronautics and Astronautics (AIAA), Jan. 1991. DOI: https://doi.org/10.2514/6.1991-68.

[55] R. Vos and S. Farokhi. *Introduction to Transonic Aerodynamics*. Vol. 110. Dordrecht: Springer Netherlands, 2015. ISBN: 978-94-017-9746-7. DOI: 10.1007/978-94-017-9747-4.

[56] S.F. Hoerner. *Fluid-Dynamic Drag*. Tech. rep. 1992.

[57] G. Q. Zhang et al. “Investigation of the tail dihedral effects on the aerodynamic characteristics for the low speed aircraft”. In: *Advances in Mechanical Engineering* 2013 (2013). ISSN: 16878132. DOI: 10.1155/2013/308582.

[58] D. Ciliberti et al. *Aircraft directional stability and vertical tail design: A review of semi-empirical methods*. Naples, Nov. 2017. DOI: 10.1016/j.paerosci.2017.11.001.

[59] D. Scholz. “Empennage sizing with the tail volume complemented with a method for dorsal fin layout”. In: *INCAS Bulletin* 13.3 (2021), pp. 149–164. ISSN: 22474528. DOI: 10.13111/2066-8201.2021.13.3.13.

[60] A. Kumar Kundu. *Aircraft design*. Cambridge University Press, 2010. ISBN: 9780511844652. DOI: https://doi.org/10.1017/CBO9780511844652. URL: www.cambridge.org/Kundu.

[61] J. Mcdavid, B. Kühner, and D. Scholz. “Project Empennage Sizing: The Tail Lever Arm as a Percentage of Fuselage Length Determined from Statistics”. In: *HAW Hamburg* (Nov. 2017). DOI: 10.7910/DVN/TLFDIU. URL: https://doi.org/10.7910/DVN/TLFDIU.

[62] F.M. Nita and D. Scholz. *Aircraft Design Studies Based on the ATR 72*. Tech. rep. 2008, pp. 14–15.

[63] J.A. Mulder et al. *Flight Dynamics Lecture Notes*. Tech. rep. 2013.

[64] R.C. Nelson. *Flight stability and automatic control*. WCB/McGraw Hill, 1998, p. 441. ISBN: 0070462739.

[65] M. Drela. *Athena Vortex Lattice*. URL: https://web.mit.edu/drela/Public/web/dfdc/.

[66] L.L.M. Veldhuis. "Propeller Wing Aerodynamic Interference". PhD thesis. Delft University of Technology, 2005.

[67] Snorri Gudmundsson. "The Anatomy of the Wing". In: *General Aviation Aircraft Design*. Elsevier, 2022, pp. 321–413. DOI: 10.1016/b978-0-12-818465-3.00009-4.

[68] Qingxi Li et al. "Towards Optimum Swirl Recovery Vanes for Propeller Propulsion Systems". In: American Institute of Aeronautics and Astronautics (AIAA), June 2017. DOI: 10.2514/6.2017-3571.

[69] E.N. Jacobs and K.E. Ward. *Interference of Wing and Fuselage from Tests of 209 Combinations in the NACA Variable Density Tunnel*. Tech. rep. NASA.

[70] M.H. Sadraey. *Aircraft design: a systems engineering approach*. Hoboken: Wiley, 2012.

[71] R.D. Finck. *USAF Stability and Control DATCOM*. Tech. rep. MCDonnel Aircraft co., 1977.

[72] J. Weissinger. "On the aerodynamics of ring wings, 1. The pressure dirstribution on a thin, almost axially symmetric wing in subsonic flow." In: *Tech. Rep. (David Taylor Model Basin)* (1957).

[73] S.F. Hoerner and H.V. Borst. *Fluid Dynamic Lift*. Tech. rep. 1985.

[74] H.J. Allen, E.W. Perkins, and M. Field. *A Study of Effect of Viscosity On Flow Over Slender Inclined Bodies of Revolution*. Tech. rep. NACA, Aug. 1952.

[75] M. Tabata and S. Fujima. *Finite-element analysis of high Reynolds number flows past a circular cylinder*. Tech. rep. 1991, p. 411.

[76] M. Drela. *XFOIL: An Analysis and Design System for Low Reynolds Number Airfoils*. Tech. rep.

[77] M. Drela, H. Youngren, and S. Sanders. *Ducted Fan Design Code*. URL: https://web.mit.edu/drela/Public/web/dfdc/.

[78] T. Sinnige. *Propeller Aerodynamics*. May 2024.

[79] K.W. Mort and B. Gamse. *A Wind-Tunnel Investigation of a 7-Foot-Diameter Ducted Propeller*. Aug. 1967.

[80] A.H.L.G. Bone et al. *Tabellenboek Bouwkunde*. 3e druk. Noordhoff Uitgevers, 2012. ISBN: 978-90-01-01595-4.

[81] US Department of Transportation. *AC 25.491-1 - Taxi, Takeoff and Landing Roll Design Loads*. Tech. rep. FAA, Oct. 2000.

[82] EASA. *Type-Certificate Data Sheet for Engine PW100 series*. Tech. rep. EASA, Dec. 2023.

[83] J. Roskam and C.T.E. Lan. "Airplane Aerodynamic and Performance". In: *DARcorporation* (1997).

[84] C.D. Perkins and R.E. Hage. *Airplane Performance Stability and Control*. New York: John Wiley and Sons, inc., 1960.

[85] T.C.A. Stokkermans et al. "Aerodynamic interaction effects between propellers in typical evtol vehicle configurations". In: *Journal of Aircraft* 58.4 (2021), pp. 815–833. ISSN: 15333868. DOI: 10.2514/1.C035814.

[86] M.F. Niţă and D. Scholz. *Conceptual Design Studies Based on the ATR 72*. Tech. rep. HAW Hamburg, 2008, pp. 14–15.

[87] P. Della Vecchia and D. Ciliberty. *Matlab live script for aircraft stability and control*. Tech. rep. Napels: Scuola Politechnica e Delle Scienze Di Base Dipartimento Di Ingegneria Industriale, 2023.

[88] Janes. *All the world's aircraft - ATR72*. URL: https://janes.migavia.com/inter/atr/atr-72.html.

[89] H.F. Mourão Bento. *Aerodynamic interaction effects of circular and square ducted propellers*. Tech. rep. Delft University of Technology, May 2019. URL: http://repository.tudelft.nl/..

A

DUUC configurations

This appendix contains the geometric information with respect to both DUUC configurations that have been used in the feasibility analysis of the DUUC.

A.1. DUUC - configuration 1

The geometric properties of the DFS used in the results for configuration 1 are listed in Table A.1.

Table A.1: Geometry used for the DFS components in DUUC configuration 1.

Component	Value	Unit
Duct diameter	3.40	$[m]$
Duct chord	1.70	$[m]$
Duct airfoil	NACA0012	[-]
Pylon span	1.00	$[m]$
Pylon chord	1.00	$[m]$
Pylon airfoil	NACA0012	[-]
x_{pylon}	0.85	$[m]$
Support span	3.40	$[m]$
Support chord	0.75	$[m]$
Support airfoil	NACA0012	[-]
$x_{support}$	0.85	$[m]$
Nacelle diameter	1.00	$[m]$
Control Vanes airfoil	NACA0016	[-]
Control Vane span	1.80	$[m]$
Control Vane chord	0.30	$[m]$
$x_{control}$	1.37	$[m]$
n_{blades}	6	$[-]$
Cant angle	35	$[deg]$
x_{PE}	27.00	$[m]$
z_{PE}	3.08	$[m]$

A.2. DUUC - configuration 2

The geometric properties of the DFS used in the results for configuration 2 are listed in Table A.2.

Table A.2: Geometry used for the DFS components in DUUC configuration 2.

Component	Value	Unit
Duct diameter	3.60	$[m]$
Duct chord	1.80	$[m]$
Duct airfoil	NACA0012	[-]
Pylon span	0.75	$[m]$
Pylon chord	1.00	$[m]$
Pylon airfoil	NACA0012	[-]
x_{pylon}	0.90	$[m]$
Support span	3.40	$[m]$
Support chord	0.75	$[m]$
Support airfoil	NACA0012	[-]
$x_{support}$	0.90	$[m]$
Nacelle diameter	1.00	$[m]$
Control Vanes airfoil	NACA0016	[-]
Control Vane span	1.80	$[m]$
Control Vane chord	0.30	$[m]$
$x_{control}$	1.44	$[m]$
n_{blades}	6	$[-]$
Cant angle	30	$[deg]$
x_{PE}	4.80	$[m]$
z_{PE}	3.08	$[m]$

B

ATR72-600 - reference aircraft

In this appendix, relevant properties of the ATR72-600 aircraft are calculated or the calculation is explained. This allows for an easy and fair comparison between the reference aircraft and the DUUC.

B.1. Weight Estimation

The weight estimation of the reference aircraft follows the same equations as presented in section 5.1. The horizontal and vertical tail surface are determined using Equation 5.1. The engine and nacelle mass are calculated using Equation 5.6 and Equation 5.5, respectively. The results of the weight estimation are given in Table B.1. The reference values are obtained from the University of Applied Sciences from Hamburg [86].

For determining the weight of the fuselage and wing, Equation B.1 and Equation B.2 are used, according to Torenbeek [50]. Where the wetted area of the fuselage is predicted by means of Equation B.3. The equation for the wing mass is valid for aircraft with a maximum take off mass above 5700 kg and for the fuselage a dive speed greater than 130 m/s ensures this equation applies.

A 5% reduction in wing mass can be applied when the landing gear is not mounted to the wing. Additionally, according to Torenbeek [50] the wing mass can be decreased by 5% when the engines are not mounted onto the wing.

$$m_{fus} = 0.23 \cdot \sqrt{V_{dive} \cdot \frac{l_{fus}}{w_{fus} + h_{fus}}} \cdot S_{wet,fus}^{1.2} \tag{B.1}$$

$$m_w = m_{MZF} \cdot 6.67 \cdot 10^{-3} \cdot b_s^{0.75} \cdot \left(1 + \frac{b_{ref}}{b_s}\right) \cdot n_{ult}^{0.55} \cdot \left(\frac{b_s/t_r}{m_{MZF}/S_w}\right)^{0.30} \tag{B.2}$$

Table B.1: Weight estimation reference aircraft.

Component	Model value [kg]	Reference value [kg] [62]
Fuselage	2685	2323
Wing	2875	3309
Vertical Tail	178	178
Horizontal Tail	146	124
Engine (for both engines)	1532	1532
Nacelle	228	241

B.2. Zero Lift Drag

The wetted area of the fuselage of the ATR is determined using Equation B.3. Torenbeek [50] provides this relation where the fuselage assumes a cylindrical middle part. The slenderness ratio of the fuselage

is represented by λ_{fus}. According to Torenbeek [50] an additional 3% has to be added to the zero lift drag of the fuselage due to the landing gear fairings of the main landing gear.

$$S_{wet,fus} = \pi \cdot d_{fus} \cdot l_{fus} \cdot \left(1 - \frac{1}{\lambda_{fus}^2}\right) \tag{B.3}$$

The wetted area of for the components in the ATR are listed in Table B.2. The zero lift drag coefficient values for the relevant components of the ATR are given in Table B.3.

Table B.2: S_{wet} values for the ATR obtained from Nita [62].

Component	S_{wet} $[m^2]$
Fuselage	222
Wing	129
Vert. tail	29
Hor. tail	22
Nacelle	18

Table B.3: C_{D0} values for the ATR obtained from Nita [62].

Component	C_{D0} [-]
Fuselage	$8.053 \cdot 10^{-3}$
Wing	0.014
Vert. tail	$1.315 \cdot 10^{-3}$
Hor. tail	$8.347 \cdot 10^{-4}$
Nacelle	$1.160 \cdot 10^{-3}$

B.3. Stability Derivatives

The stability coefficient of the fuselage ($C_{N_{\beta,fus}}$), relevant for the directional stability of the aircraft, can be determined using Equation B.4 defined by Finck [71].

$$C_{N_{\beta,fus}} = -\frac{360}{2 \cdot \pi} \cdot k_N \cdot K_{R,J} \cdot \frac{l_{fus}^2 \cdot d_{fus}}{S_w \cdot b} \tag{B.4}$$

Where the factors k_N and $k_{R,J}$ are represented in Equation B.5 and Equation B.6 respectively.

$$k_N = 0.01 \cdot \left[0.27 \cdot \frac{x_M}{l_{fus}} - 0.168 \cdot ln\left(\frac{l_{fus}}{d_{fus}}\right) + 0.416\right] - 0.0005 \tag{B.5}$$

$$k_{R,J} = 0.46 \cdot log\left(\frac{Re}{10^6}\right) + 1 \tag{B.6}$$

C

Experimental Data Processing

In this appendix the processing of the experimental data is explained as well as the scaling factors used for different experimental sources.

C.1. Spinner Mass Estimation

The spinner mass relative to the blades of a propeller can be estimated by taking the average spinner mass of the example propellers given in Table C.1. This results in an average weight increase of 10%.

Table C.1: Relative spinner hub mass of a propeller.

Propeller	Mass blades [kg]	Mass hub [kg]	Relative mass [%]
Dowty R381/6-123-F/5	227	23	10.1%
Hartzell ASC-II	18.1	1.8	9.9%

C.2. AVL Setup and Scaling

The AVL setup that has been used to determine the aerodynamic properties of the DFS is illustrated in Figure C.1. It must be noted that the right scaling factor has to be used in order to compare the experimental data with the results obtained from AVL.

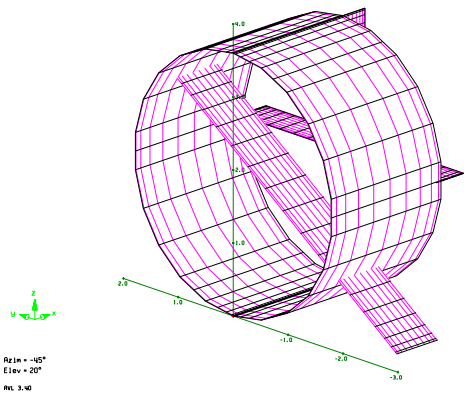

Figure C.1: AVL setup used to calculate the aerodynamic properties for the DFS.

The applied scaling factor is given in Equation C.1. This has to do with a mismatch between the definition of the aspect ratio of a regular wing and the definition of the AR in this thesis. The value of 10 is obtained by multiplying all values in Table C.2

$$k_{AVL} = \frac{10}{AR_{duct}} \tag{C.1}$$

Table C.2: Scaling factors used to modify AVL results.

Factor	Value
AR definition mismatch	π
Weissinger's horseshoe vortex simplification	2
AVL's resolution of bidirectional tip vortices	1.6

C.3. Reference Data Scaling Factors

For each source with experimental data of ducts, shrouded propellers and nacelles, a separate scaling factor has been applied to allow for a fair comparison. The reference area has been kept equal and whilst validating the results of the components, the flight and operating conditions have been taken similarly.

For the ducted fans, an attempt has been made use the same geometry. Not all data about the experimental setup was publicly available and hence the results are not fully one-to-one comparable.

D

Aerodynamic Performance PE

This appendix contains the aerodynamic coefficients of the individual DFS components over a range of angle of attack.

Duct

The lift, drag and pitching moment coefficient of the duct can be found in Figure D.1, Figure D.2 and Figure D.3, respectively.

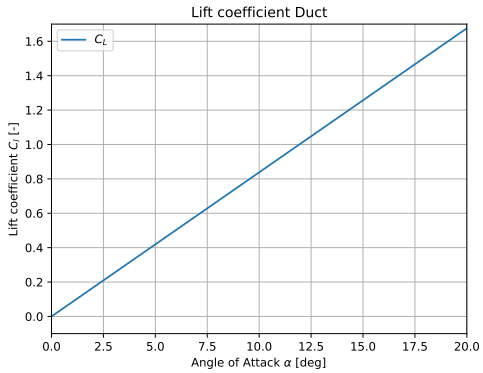

Figure D.1: C_L vs. α for the duct in the DFS.

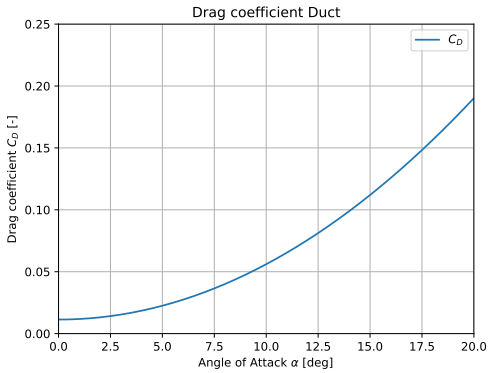

Figure D.2: C_D vs. α for the duct in the DFS.

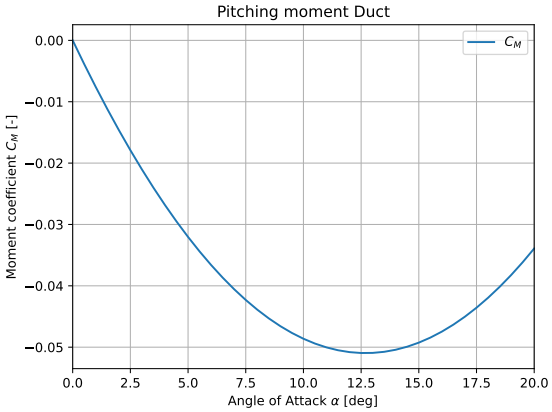

Figure D.3: C_M vs. α for the duct in the DFS.

Pylon

The lift, drag and pitching moment coefficient of the pylon can be found in Figure D.4, Figure D.5 and Figure D.6, respectively.

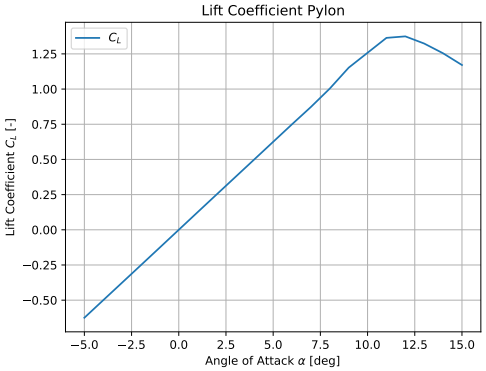

Figure D.4: C_L vs. α for the pylon in the DFS.

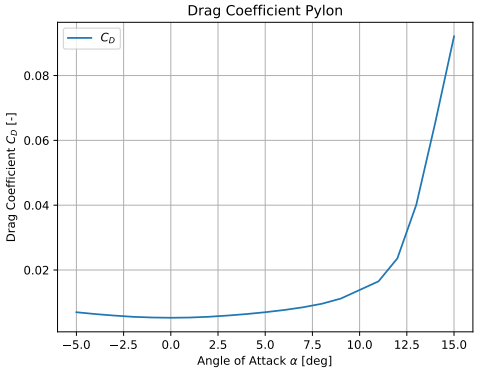

Figure D.5: C_D vs. α for the pylon in the DFS.

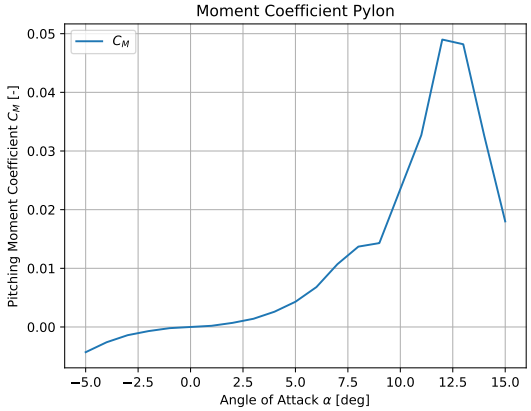

Figure D.6: C_M vs. α for the pylon in the DFS.

Nacelle

The lift, drag and pitching moment coefficient of the nacelle can be found in Figure D.7, Figure D.8 and Figure D.9, respectively.

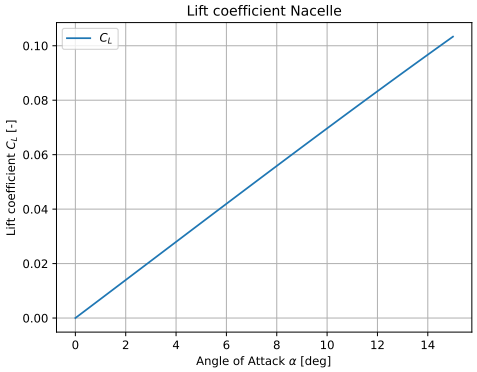

Figure D.7: C_L vs. α for the nacelle in the DFS.

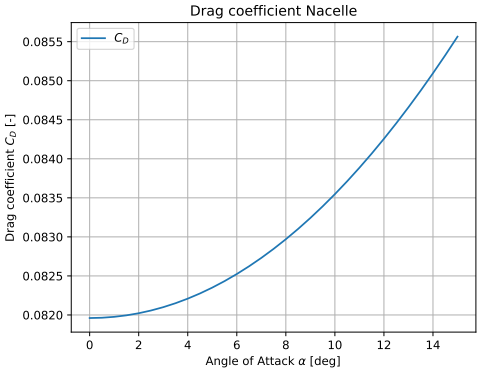

Figure D.8: C_D vs. α for the nacelle in the DFS.

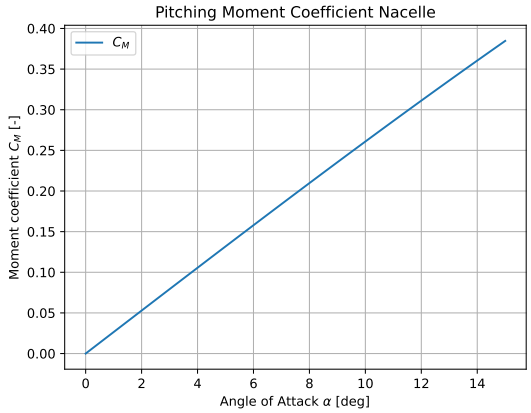

Figure D.9: C_M vs. α for the nacelle in the DFS.

Support

The lift, drag and pitching moment coefficient of the support can be found in Figure D.10, Figure D.11 and Figure D.12, respectively.

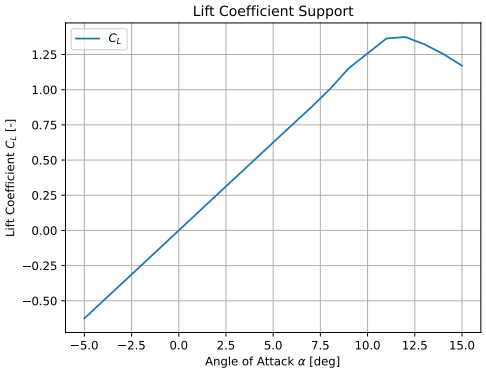

Figure D.10: C_L vs. α for the support in the DFS.

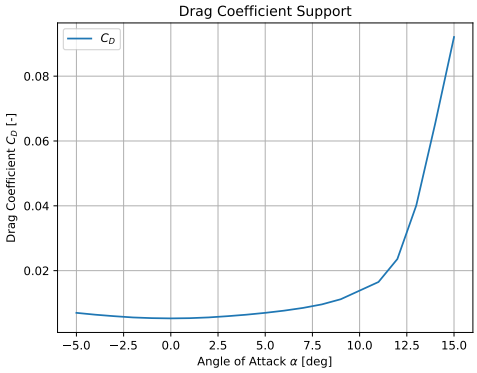

Figure D.11: C_D vs. α for the support in the DFS.

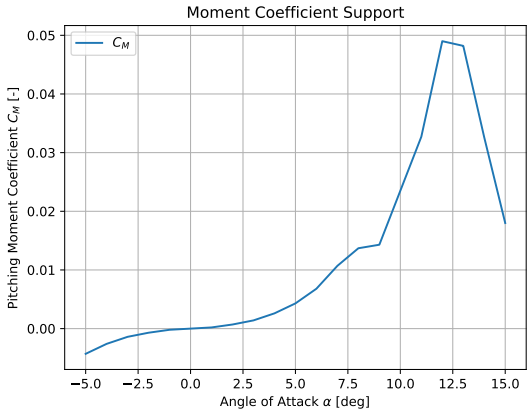

Figure D.12: C_M vs. α for the support in the DFS.

Control Vanes

Support

The lift, drag and pitching moment coefficient of the control vanes can be found in Figure D.13, Figure D.14 and Figure D.15, respectively.

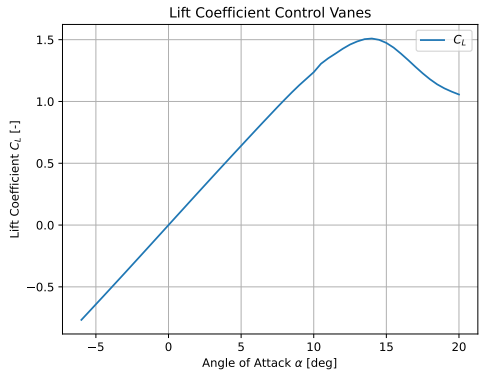

Figure D.13: C_L vs. α for the control vanes in the DFS.

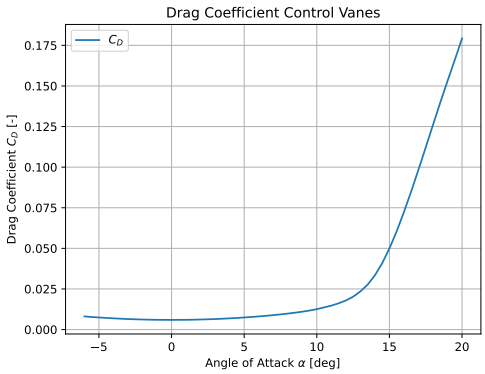

Figure D.14: C_D vs. α for the control vanes in the DFS.

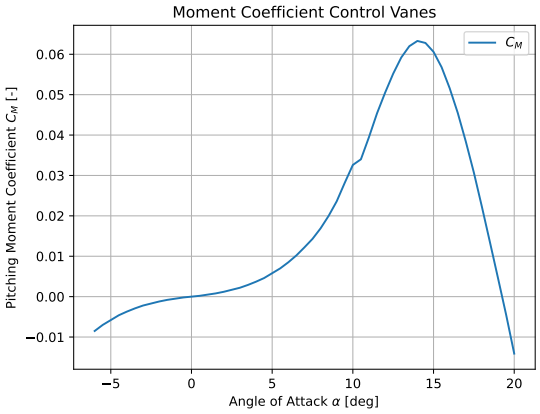

Figure D.15: C_M vs. α for the control vanes in the DFS.